Spring 1988

Full-Potential Integral Solutions for Steady and Unsteady Transonic Airfoils With and Without Embedded Euler Domains

Hong Hu
Old Dominion University

FULL-POTENTIAL INTEGRAL SOLUTIONS FOR STEADY AND UNSTEADY TRANSONIC AIRFOILS WITH AND WITHOUT EMBEDDED EULER DOMAINS

by

Hong Hu
B.S., February 1982, Zhejiang Institute of Technology, China
M.E., May 1984, Old Dominion University

A Dissertation Submitted to the Faculty of
Old Dominion University in Partial Fulfillment of the
Requirements for the Degree of

DOCTOR OF PHILOSOPHY
MECHANICAL ENGINEERING

OLD DOMINION UNIVERSITY
March 1988

Approved by:

Osama A. Kandil (Director)

Samuel R. Bland (NASA-LaRC)

Erwon Lavante

Robert L. Ash

John H. Heinbockel

ABSTRACT

FULL-POTENTIAL INTEGRAL SOLUTIONS FOR STEADY AND UNSTEADY TRANSONIC AIRFOILS WITH AND WITHOUT EMBEDDED EULER DOMAINS

Hong Hu
Old Dominion University, 1988
Director: Dr. Osama A. Kandil

The integral equation solution of the full-potential equation is presented for steady and unsteady transonic airfoil flow problems. The method is also coupled with an embedded Euler domain solution to treat flows with strong shocks for steady flows.

For steady transonic flows, three integral equation schemes are well developed. The first two schemes are based on the integral equation solution of the full-potential equation in terms of the velocity field. The Integral Equation with Shock-Capturing (IE-SC) and the Integral Equation with Shock-Capturing Shock-Fitting (IE-SCSF) schemes have been developed. The IE-SCSF scheme is an extension of the IE-SC scheme, which consists of a shock-capturing (SC) part and a shock-fitting (SF) part in which shock panels are introduced at the shock location. The shock panels are fitted and crossed by using the Rankine-Hugoniot relations in the IE-SCSF scheme. The third scheme is based on coupling the IE-SC integral equation solution of the full-potential equation with the psuedo time integration of the Euler equations in a small embedded domain around the shock within the IE computational domain. The integral solution provides the initial and boundary conditions for the Euler domain. This scheme is named as the Integral Equation-Embedded Euler (IE-EE)

scheme. These three schemes are applied to different airfoils over a wide range of Mach numbers, and the results are in good agreement with the experimental data and other computational results.

For unsteady transonic flows, the full-potential equation formulation in the moving frame of reference has been used. The steady IE-SC scheme has been extended to treat airfoils undergoing time-dependent motions, and the unsteady IE-SC scheme has thus been developed. The resulting unsteady scheme is applied to a NACA 0012 airfoil undergoing a pitching oscillation around the quarter chord length. The numerical results are compared with the results of an implicit approximately-factored Euler scheme.

ACKNOWLEDGMENTS

I would like to express the highest apprecriation to my dissertation advisor, Professor Osama A. Kandil, for his able guidance and valuable suggestions during the entire course of this study.

Also I wish to thank the members of my dissertation committee: Drs. Samuel R. Bland and E. von Lavante, Professors Robert L. Ash and John H. Heinbockel, for their review and comments on this dissertation. The author would like to thank Dr. John Edwards, Head of the Unsteady Aerodynamics Branch of the NASA-Langley Research Center, for his valuable discussions.

This research work has been supported by the Unsteady Aerodynamics Branch of the NASA-Langley Research Center under Grant No. NAG-1-648, monitored by Dr. Samuel Bland. The author would like also to thank the College of Engineering for the partial financial support through the College of Engineering Fellowship.

I would like to mention that Mr. Andrew Chuang provided the useful finite-difference unsteady Euler solution for comparison with the current unsteady results.

Finally, I am very grateful to my wife, Betty, for her understanding, patience and sacrifices throughout my entire dissertation work. Also, I want to thank my parents for all they have done.

TABLE OF CONTENTS

	Page
LIST OF SYMBOLS	vi
LIST OF FIGURES	ix
Chapter	
1. INTRODUCTION	1
2. LITERATURE SUVERY	7
2.1 Physics of Steady and Unsteady Transonics	7
2.2 Transonics before 1970	10
2.3 Current Status of Steady Transonics	12
2.3.1 FD Methods for Steady Inviscid Transonics	12
2.3.2 IE Methods for Steady Inviscid Transonics	18
2.3.3 Experimental Work in Steady Transonics	21
2.4 Current Status of Unsteady Transonics	23
2.4.1 FD Methods for Unsteady Inviscid Transonics	23
2.4.2 IE Methods for Unsteady Inviscid Transonics	28
2.4.3 Experimental Work in Unsteady Transonics	30
2.5 Summary	33
3. FORMULATION OF THE PROBLEM	34
3.1 Physical Aspects of Flow Modeling	34
3.2 Full-Potential Equations	38
3.2.1 Physical Problems	38

3.2.2 General Unsteady Full-Potential Equation 39
3.2.3 2-D Steady Full-Potential Equation 46
3.2.4 2-D Unsteady Full-Potential Equation 47
3.3 IE Solutions of FP Equations 49
3.3.1 Panel Methods or Incompressible IE Methods 49
3.3.2 IE Solution for Steady Transonic Flows 51
3.3.3 IE Solution for Unsteady Transonic Flows 53
3.4 Unsteady Euler Equations 54
3.5 Validity of IEM for Transonics 55
4. COMPUTATIONAL SCHEMES OF STEADY TRANSONIC FLOWS 56
4.1 IE Scheme for Shock-Free Flows 56
4.1.1 Discretization of the Equations, No-Penetration Condition 56
4.1.2 Computational Scheme for Shock-Free Flows 59
4.2 IE-SC and IE-SCSF Schemes for Transonic Flows 63
4.2.1 IE-SC Scheme 63
4.2.2 IE-SCSF Scheme 65
4.3 IE-EE Scheme for Transonic Flows with Strong Shocks 68
5. COMPUTATIONAL SCHEME OF UNSTEADY TRANSONIC FLOWS 73
5.1 Unsteady IE-SC Scheme 73
5.2 Wake Point Vortex Generation 80
6. NUMERICAL RESULTS 83
6.1 Steady Transonic Flow Solutions 84
6.1.1 Shock-Free Flow Solutions 84
6.1.2 IE-SC and IE-SCSF Solutions for Transonic Flows 87
6.1.3 IE-EE Solutions for Transonic Flows 89
6.2 Unsteady Transonic Flow Solutions 92

7. CONCLUSIONS AND RECOMMENDATIONS 95

REFERENCES 99

APPENDICES

A. SURFACE INTEGRALS 111

B. FIELD INTEGRALS 113

FIGURES 116

LIST OF SYMBOLS

A	Area
$[A_{i,j}]$	Influence coefficient matrix
a	Speed of sound
c	Airfoil chord length
C_p	Pressure coefficient
d_{sr}	Distance between receiver and sender
e_t	Total energy
$\vec{e}_o$	Unit vector of $\vec{V}_o$, $\vec{e}_o \equiv u_o\vec{i} + v_o\vec{j}$
$\vec{e}_\infty$	Unit vector of free-stream velocity, $\vec{e}_\infty \equiv -\vec{e}_o$
g	Body surface, airfoil surface
G, G_1	Full compressibility
G_2	Unsteady compressibility
h_t	Total enthalpy
k	Thermal conductivity
k_c	Reduced frequency based on the chord length, $k_c = \omega c/\lvert\vec{V}_o\rvert$
k_{ch}	Reduced frequency based on the half-chord length, $k_{ch} = k_c/2$
l	Characteristic length
M	Local Mach number
M_∞	Free-stream Mach number
M_{crit}	Critical free-stream Mach number
$\vec{n}$	Surface unit normal vector

p	Pressure
q	Source strength
$\vec{r}$	Position vector
S	Entropy
s	Line element
t	Time
$\vec{V}$	Absolute velocity vector, $\vec{V} \equiv u\vec{i} + v\vec{j}$ and $V \equiv \lvert\vec{V}\rvert$
$\vec{V}_e$	Transformation velocity vector of the moving frame of reference
$\vec{V}_o$	Translation velocity vector of the moving frame of reference
$\vec{V}_r$	Relative velocity vector
w	Wake surface
α	Angle of attack
$\dot{\alpha}$	Rate of the change of α
α_o	Mean angle of attack
α_a	Amplitude of angle of attack
β	Shock-panel angle
γ	Surface vortex distribution
κ	Gas specific heat ratio
θ	Relative direction of the flows across the shock
$\vec{\zeta}$	Vorticity, $\vec{\zeta} \equiv \nabla \times \vec{V}$
μ	Viscous coefficient
ρ	Density
ω	Frequency
Γ	Circulation, or total surface vortex ($\Gamma \equiv \int_{panel} \gamma dl$)
Φ	Velocity potential, $\nabla\Phi \equiv \vec{V}$
Ω	Angular velocity of the moving frame of reference

Subscripts

1	Condition ahead of the shock
2	Condition behind of the shock
∞	Infinity condition
av	Average value
n	Normal component
p	Oscillation pivot point
t	Tangential component
u	Upper surface value
l	Lower surface value
sp	Edge of separation
TE	Airfoil trailing edge
S	Shock surface
i, k	Second subscript, k, refers to wake point vortex numbers, etc.

Superscripts

(n)	Time step level
$'$	(Time derivative) with respect to the moving frame of reference

LIST OF FIGURES

Figure		Page
2.1	Classification of the flow	116
2.2	Sketch of a typical transonic flow	117
3.1	Physical problem and coordinate system for steady flows	118
3.2	Physical problem and coordinate system for unsteady flows	119
3.3	Space-fixed and body-fixed frames of reference	120
4.1	Airfoil surface paneling	121
4.2	Computational domain and field-elements	122
4.3	Relation between global and local coordinates	123
4.4	Computational steps for shock-free flows	124
4.5	Near-field vs. far-field computations	125
4.6	Computational steps of the IE-SCSF scheme	126
4.7	Index used in difference scheme	127
4.8	Illustration of shock panels and field-element splitting	128
4.9	Computational region of the IE with embedded Euler domain	129
4.10	Computational steps of the IE-EE scheme	130
5.1	Computational steps of the unsteady IE-SC scheme	131
5.2	Wake point vortex generation	132
6.1	Vortex vs. source panels, NACA 0012, $M_\infty = 0, \alpha = 0^o$	133
6.2	Vortex vs. source-vortex panels, NACA 0012, $M_\infty = 0, \alpha = 9^o$	134
6.3	Vortex vs. source panels, NACA 0012, $M_\infty = 0.72, \alpha = 0^o$	135
6.4	Computational domain effect, NACA 0012, $M_\infty = 0.72, \alpha = 0^o$	136

6.5 Computational domain effect, NACA 0012, $M_\infty = 0.63, \alpha = 2^o$ 137

6.6 Comparisons with FD solutions, NACA 0012, $M_\infty = 0.63, \alpha = 2^o$ 138

6.7 IE-SC vs. IE-SCSF schemes, NACA 0012, $M_\infty = 0.8, \alpha = 0^o$ 139

6.8 Comparison of the IE-SCSF solution, NACA 0012, $M_\infty = 0.8, \alpha = 0^o$ 140

6.9 Comparison of the IE-SCSF solution, NACA 0012, $M_\infty = 0.75$, $\alpha = 2^o$ 141

6.10 Comparison of the IE-SCSF solution, NACA 64A010A, $M_\infty = 0.796, \alpha = 0^o$ 142

6.11 Comparison of the IE-EE solution, NACA 0012, $M_\infty = 0.8, \alpha = 0^o$ 143

6.12 Comparison of the IE-EE solution, NACA 0012, $M_\infty = 0.75, \alpha = 2^o$ 144

6.13 Comparison of the IE-EE solution, NACA 64A010A, $M_\infty = 0.796$, $\alpha = 0^o$ 145

6.14 Comparison of the IE-EE solution, NACA 0012, $M_\infty = 0.812$, $\alpha = 0^o$ 146

6.15 Comparison of the IE-EE solution, NACA 0012, $M_\infty = 0.82, \alpha = 0^o$ 147

6.16 IE and Euler domains, NACA 0012, $M_\infty = 0.84, \alpha = 0^o$ 148

6.17 Comparison of the IE-EE solution, NACA 0012, $M_\infty = 0.84, \alpha = 0^o$ 149

6.18 Initial C_p distributions, NACA 0012, $M_\infty = 0.755, \alpha = \alpha_o = 0.016^o$ 150

6.19 Lifting coefficients for a pitch oscillation, NACA 0012, $M_\infty = 0.755$, $\alpha(t) = 0.016^o + 1.255^o \sin(0.1632t)$ 151

6.20 Time history of C_p for a pitching oscillation, NACA 0012, $M_\infty = 0.755, \alpha(t) = 0.016^o + 1.255^o \sin(0.1632t)$ 152

Chapter 1

INTRODUCTION

One of the main difficulties facing the aircraft designer is to predict the aerodynamic loads at transonic speeds. The mixed nature and the nonlinearity of the flow are at the root of the difficulty. In the transonic regime, even the simplest representation of the aerodynamics must be described by a mixed type, nonlinear, partial-differential equation or set of equations. This fact is in contrast to the subsonic or supersonic flow regimes where an adequate representation of the aerodynamics can be obtained by using linear theory and mixed type governing equations do not occur. On the other hand, the transonic flow regime is a very important flow regime, because it is in this regime that most military aircraft maneuvers and most civil aircraft cruises. Due to the difficulties and importance of the prediction of aerodynamic loads at transonic speeds, the transonic flow regime is probably the most critical flow regime for today's aircraft. Therefore, it is of extreme importance to have an understanding of the flow and to provide the aircraft designer with accurate and reliable prediction methods that are as advanced and as relevant to practice as possible.

As the name implies, transonic flows are the flows where the velocities are in the neighborhood of the local speed of sound. The flows are characterized by the presence of both subsonic and supersonic regions within the flow field simultaneously. Therefore, transonic flows are described by a mixed elliptic-hyperbolic partial differential equation with the boundary between them unknown apriori. For

both subsonic and supersonic flows, there exist physical analogs which facilitate the interpretation of these phenomena. In addition, the close relationship between the governing equations of subsonic flows and the Laplace equation as well as that between the governing equations of supersonic flows and the wave equation are very helpful. But, the same is not true of transonic flows. There is almost no phenomenon analogous to the mixed flow and there is almost no available theory of the mixed elliptic-hyperbolic differential equations.

Also, the nonlinear physics is associated with transonic flows. In transonic flows, the disturbance propagation velocity is comparable in magnitude with the local fluid velocity. The familiar inequalities $a \gg u$ or $a \ll u$ of classical subsonic or supersonic flow theory are no longer valid for transonic flows. This makes transonic flow equations impossible to linearize. Also since the shock location and the shock strength is a crucial part of a transonic computation, any method for predicting the aerodynamic loads must be based on a nonlinear equation or set of nonlinear equations.

For unsteady flows under certain conditions, aircraft structures like wings and tail surfaces may experience severe vibrations of an unstable nature. This aeroelastic phenomenon is governed by the interaction of elastic and inertial forces with the unsteady aerodynamic forces, and it is called "flutter". This phenomenon may lead to the disintegration of the structure. The accuracy of the flutter prediction depends mainly on the knowledge of unsteady aerodynamic forces.

For unsteady transonic flows at low to moderate reduced frequencies, the governing equation of the flow cannot be linearized in contrast with the unsteady subsonic or supersonic flows. This means that the unsteady transonic flow field cannot be treated independently of the steady flow field. This makes the unsteady transonic flow problems considerably more complicated.

The development of a method for predicting aerodynamic loads at transonic speeds has challenged many scientists and engineers. During the last decade, the decade for the advance of the computational aerodynamics, significant research work has been done in the computational transonics. Most of the work done is in the finite-difference (FD) and finite-volume (FV) methods and some work is in the integral equation (IE) methods. In Chapter 2, a review of the current research work on transonics will be presented.

For flows with shocks of weak to moderate strength, the potential equation, which assumes irrotational isentropic flows, can be used satisfactorily to solve for these flows, since the entropy increase and vorticity production across the shock are small. The integral equation solution of the potential equation represents an alternative to the finite-difference and finite -volume methods (FDM and FVM) for treating transonic flows.

The integral equation method (IEM) has several advantages over the finite-difference and finite-volume methods. It involves evaluation of integrals, which is more accurate and simpler than the FDM and FVM where the accuracy depends on the grid size since they involve evaluation of derivatives. In the IEM, grid refinement and high-order source, vorticity and compressibility modeling can be used in order to increase the accuracy. Moreover, the IEM automatically satisfies the far-field boundary conditions as $O(1/r)$ or $O(1/r^2)$ and hence only a small limited region around the source of disturbance is needed. In the FDM and FVM, grid points are needed over a large region around the source of disturbance and special treatment is required to satisfy the far-field boundary conditions where a certain part of the boundary is treated as an inflow boundary while the other part is treated as an outflow boundary. The IEM is computationally inexpensive, particularly for unsteady flows, and does not suffer from the artificial viscosity effects as compared

to FDM and FVM for shock capturing in transonic flows. Because of these obvious advantages of the method, it is highly desirable to fully develop the IEM and extend it to treat transonic flows over a wide range of Mach numbers.

But, for the upper transonic range, where strong shocks exist and where entropy changes and vorticity production cannot be ignored, and for flows with distributed vorticity existing in the field, the potential equation simply breaks down unless these effects are carefully taken into account. Thus, the integral equation method which is based on the potential flow assumption is not valid for flows with strong shocks. It should be mentioned that the use of Helmholtz decomposition along with scalar and vector potentials can be used in this regard.

Euler equations admit distributed vorticity fields and should produce accurate solutions for rotational flows with strong shock waves. But, the numerical solutions of the Euler equations are expensive. Usually the airfoil Euler computation requires a fine grid and a large computational domain, of which the outer boundary extends twenty to thirty chord lengths away from the airfoil surface. On the other hand, it is known that the flow rotationality is confined to a limited small domain behind the strong shock, and hence the flow can be assumed irrotational outside this domain. Therefore, a combined algorithm using the IEM for the full-potential equation and the FVM for the Euler equations is most desirable for transonic flows with strong shocks.

The objective of this dissertation is to develop efficient, reliable and accurate computational schemes to treat transonic flows using the IEM for the full-potential equation with and without embedded Euler domains.

Three IE schemes are developed and are briefly described as follows:

(i) An IE scheme for the full-potential equation to solve for transonic flows with shocks of moderate strength. Shocks are captured in this scheme. This is called the Integral Equation with Shock Capturing (IE-SC) scheme.

(ii) An IE scheme, similar to the one given in item (i) with the exception of fitting the shocks once they are captured. This scheme is called the Integral Equation with Shock Capturing- Shock Fitting (IE-SCSF) scheme.

(iii) An IE scheme, similar to the one given in item (i) with the exception of using Euler equations in an embedded domain around the captured shock. This is called the Integral Equation with Embedded Euler (IE-EE) scheme.

These schemes have been applied to steady transonic airfoil computations. The first scheme has been extended to treat unsteady transonic flows and has been applied to unsteady airfoils in pitching motion.

Chapter 2 presents an extensive literature survey of transonic research with emphasis on inviscid computational transonics. In Chapter 3, the formulation of the problem is given in terms of a moving frame of reference. The formulation is then specialized for steady flows around airfoils and unsteady flows of airfoils undergoing pitching motion. This is then followed by the corresponding integral equation solutions in terms of the velocity field for steady and unsteady flows. Finally, the Euler formulation in the embedded domain is given. The solution procedures for solving the steady airfoil transonic flows are presented in Chapter 4. The IEM for shock-free flows is first described, the IE-SC, IE-SCSF, and IE-EE schemes are then presented. Chapter 5 presents the solution procedure of the IE-SC scheme applied to unsteady flows for an airfoil undergoing pitching motion. The numerical results of steady and unsteady flows are presented in Chapter 6, along with comparisons with other numerical results and experimental data. The computations are applied

to the NACA 0012 and NACA 64A010A airfoils. The accuracy and the capability of the schemes are also discussed. Finally, the concluding remarks on the numerical schemes and the recommendations for further research on the transonic IE methods are addressed in Chapter 7.

Chapter 2

LITERATURE SURVEY

In the first section of this chapter, the physics of steady and unsteady transonic flows past airfoils is described briefly. This is then followed by a literature survey of the developments in computational and experimental transonics. Emphasis will be placed on the recent developments of the computational inviscid transonics, including both the finite-difference and integral equation methods. The early work on transonic flows before 1970 is discussed first in the second section. Then the recent developments on steady and unsteady transonic flows are presented in the following two sections, respectively.

2.1 Physics of Steady and Unsteady Transonics

A brief discussion of the physics of steady and unsteady transonic flows past airfoils provides an introduction to the review of the transonic research work. A classification of the flow past airfoils is shown in Fig. 2.1. The critical free-stream Mach number, M_{crit}, is defined as the lowest value of the free-stream Mach number, M_∞, for which the local supersonic speed ($M > 1$) appears in the flow field. The values of M_{crit} vary from one flow to another. For example, the value of M_{crit} could be as low as 0.4 for bluff bodies and as high as near 1.0 for very slender configurations. When the value of M_∞ is less than the value of M_{crit}, the whole flow field has local Mach numbers less than 1.0 and the flow is called subsonic or subcritical. When the value of M_∞ is greater than the value of M_{crit} but less than

1, the flow is called lower transonic flow or simply, transonic flow. The physics of this type of flow will be discussed in this section. If M_∞ is slightly greater than 1 and if the flow field has local Mach numbers less than 1 at some places, then the flow is called an upper transonic flow. For supersonic flows, the whole flow field has local Mach numbers greater than 1, while if M_∞ becomes greater than 5, in general, the flow is called hypersonic flow.

Figure 2.2 shows a typical transonic flow past an airfoil. The flow is subsonic in the free-stream, from which it accelerates over the airfoil to supersonic speeds and forms a supersonic region over the airfoil as shown. This supersonic region is then terminated by, in general, a shock wave through which the flow speed is reduced from supersonic to subsonic. The strength and location of the shock wave are the crucial part of transonic aerodynamic load predictions.

The strength of a normal shock in terms of the pressure jump is on the order of $(M_1^2 - 1)$, where M_1 is the local Mach number ahead of the shock wave. If the value of M_1 is not too high, then the shock is called a weak shock and the flow is called a critical flow. If the value of M_1 is large, then the shock wave is strong and the shock is called a strong shock. The flow is then called a supercritical flow. The appearance of the shock wave is related to the increase in the fluid entropy. The increase of entropy across the shock wave is of the order of $[(M_1^2 - 1)^3]$,which is the third power of the pressure change across the shock. Therefore, if the strength of the shock is small enough such that $(M_1^2 - 1)^3 \ll (M_1^2 - 1)$, the increase in the fluid entropy is negligible and the flow is then called a homentropic flow. But for strong shock flows, the increase in fluid entropy is not negligible because of the large value of $(M_1^2 - 1)$. Furthermore, from Crocco's theorem for steady, inviscid, isoenergetic flows, the assumption of the homentropic flow yields directly the assumption of potential flow. On the other hand, the increase in entropy must correspond to

the vorticity production. The details about the entropy increase and the vorticity production across the shock will be discussed in Chapter 3.

Another important phenomenon associated with the shock wave is the increase of the wave drag force. At the lower end of the transonic flow regime, the drag rises rapidly as a result of the shock wave development, and this is followed by a significant reduction of the lift force at a slightly higher free-stream Mach number. This phenomenon of significant reduction in lift is called shock stall. One of the most important practical problem in the design of aerodynamic configurations is to optimize the cruise performance at high free-stream subsonic Mach numbers before shock stall occures.

If an airfoil performs unsteady motion, such as a sinusoidal oscillation around a given mean position, the properties of the flow field show periodic variations. In general, the shock wave can be generated or lost during the motion of the airfoil. The strength and the location of the shock vary periodically with the motion of the airfoil. According to Helmholtz's theorem, a free-vortex sheet is shed from the trailing edge of the airfoil in order to conserve the total vorticity, as shown in Fig. 2.2. This free-vortex sheet is convected downstream by the local particle velocity. These phenomena of unsteady flows make the problem even more complicated.

It should be mentioned that transonic flow is largely dominated by viscous effects, although the majority of the research work on transonic flows is based on the inviscid flow assumptions. The interaction between shock waves and the wall viscous boundary-layers is a dominant factor in transonic flows. This interaction culminates in a shock-induced flow separation, which results in a loss of lift and an increase of drag. All of these phenomena cannot be understood fully without considering viscous effects. But when viscous effects are negligible compared with

the inviscid effect, the inviscid flow assumption can be used for practical transonic flow analysis.

2.2 Transonics before 1970

The study of transonic flows has a long history. Molenbroeck [1] in 1890 and Chaplygin [2] in 1904 published mathematical analyses in which they reduced the steady, two-dimensional, nonlinear, potential-flow equation for a compressible gas to a linear equation by use of a hodograph transformation. The resulting equation was applied to nozzle flows. But between those dates and 1940, very limited theoretical work was done.

Since 1940, significant efforts have been made in both theoretical and experimental areas. The difficulty associated with the theoretical work in the area of transonics is the treatment of the nonlinear mixed-type differential equations. At the time when high-speed computers were not available, the theoretical work was based mainly on physical approximations and various classical techniques. The classical theoretical work on transonic flows was made mainly in the transonic small-disturbance (TSD) theory and the transonic similarity rules.

Cole [3] has reviewed the history of transonic small-disturbance theory and the hodograph solution up to the 1960's. Of the early work, the most outstanding contributions to transonic small-disturbance theory were made by Oswatitsch and Wiegardt [4], Busemann and Guderley [5] and Guderley [6,7]. From the transonic small-disturbance theory, the transonic similarity rules were first obtained by von Karman [8,9] in 1947. Soon after this theory was applied to the symmetric transonic flow around three different single wedges [10-12], Liepmann and Bryson [13] and Bryson [14] completed wind-tunnel tests for flow around these three wedges. The experimental results showed good agreement.

During that time, there was also some work done in which the solution was sought by iterating either the full-potential equation or the approximate equations of transonic small- disturbance theory. The most notable work was due to Asaka [15] who used a third-order power series for subsonic flows past an airfoil-like shape. Another more powerfull technique for solving the transonic small-disturbance equation was the integral equation method with the most notable contribution from Oswatitsch [16,17] in 1950. The results showed good agreement with the experimental data for subsonic flows. However, no results were provided for mixed or transonic flows.

The development of the transonic theory of wings of finite span started with the introduction of the transonic similarity rules by Spreiter [18] in 1953. Then the transonic equivalence rule and transonic area rule were derived by Oswatitsch [19,20] and by Whitcomb [21], respectively. The transonic equivalence rule relates the flow around a slender body of arbitrary cross section to the flow around an "equivalent" nonlifting body of revolution with the same longitudinal distribution of cross-sectional area, while the area rule deals with the zero-lift drag. These rules were then used for slender bodies of arbitrary cross section, including wing-body combinations, by Heaslet and Spreiter [22].

By the end of the 1950's, a local linearization method was first derived by Spreiter and Alksne [23], which was applied to two-dimensional flows past thin airfoils. They replaced the original nonlinear partial differential equation by a different linear partial differential equation at each point. Soon after, this local linearization method was applied to axisymmetric flows past slender bodies of revolution [24] and to flows past non-lifting wings of finite span [25] with the free-stream Mach number near unity. The local linearization method made significant contributions to the theoretical transonics during that period.

From the discussion given above, it is obvious that the period from 1940 to 1960 was one of rapid development in transonic aerodynamics, in which the transonic small-disturbance theory played an important role. Unsteady transonic flows were not considered until the 1970's. The period between 1960 and 1970 was not one of rapid progress in transonics, but certain developments were underway which cluminated in the explosive advances of the 1970's.

2.3 Current Status of Steady Transonics

Since 1970, transonic research work has been focused heavily on the development of reliable computational methods for predicting aerodynamic loads at transonic speed with shocks. The computational methods for inviscid transonic flows can be divided basically into two types: finite-difference (FD) methods including finite-volume methods, and integral equation (IE) methods (or field panel methods). Also, finite-element methods for transonic flows have been developed recently. These methods will not be reviewed in this dissertation.

2.3.1 FD Methods for Steady Inviscid Transonics

The developments of finite-difference methods for steady inviscid transonic flows have been accomplished using three different levels of mathematical approximations for the problem formulation: (i) the transonic small-disturbance (TSD) formulation, (ii) full-potential (FP) equation formulations, and (iii) Euler equation formulations.

Finite-difference methods of transonics are new methods which started in 1970. Murman and Cole [26] were the first to obtain a stable transonic solution including the shock by solving the transonic small-disturbance equation. The computation was made on a 6%-thick circular-arc airfoil and a weak shock was captured in the

solution. The basic idea of their difference scheme was to use central-differencing at the subsonic points and to use upwind-differencing at the supersonic points. In this way the disturbance propagation of the equation is simulated computationally according to the partial-differential equation type. This scheme has been named the Murman-Cole type-difference scheme. This type-difference scheme has proven to be very successful; and opened the way for modern computational transonics. Soon after, this technique was extended to three-dimensional flows for swept-wing calculations by Ballhaus and Bailey [27] and for wing-cylinder calculations by Bailey and Ballhaus [28]. The method [27] was applied to the flow about a thin swept lifting wing. The computed results at angles of attack, $\alpha = 0^o$ and 2^o, for the planform model of aspect ratio, $AR = 4$, constant chord, sweptback angle of 23.75^o, with a Lockheed C141 airfoil section, compared well with the experimental data for the critical flows with weak shocks.

On the other hand at this same time, finite-difference solutions to the full-potential equation were being developed by using suitable mapping procedures. Notable contributions were due to Steger and Lomax [29] and Garabedian and Korn [30] for airfoil computations. Steger and Lomax [29] used a successive over-relaxation (SOR) procedure to solve the full-potential equation. The procedure was applied to blunt-nosed airfoils at a wide range of subsonic free-stream Mach numbers. The computed results for the NACA 0012 airfoil at M_∞=0.864 and $\alpha = 0^o$, at M_∞=0.75 and $\alpha = 2^o$ and at M_∞=0.80 and $\alpha = 1^o$ were reported. Also, the computed results for the NACA 0015 airfoil at M_∞=0.726 and $\alpha = 2^o$ and at M_∞=0.729 and $\alpha = 4^o$ were presented. The comparisons of these results with the experimental data for the flows with weak shocks showed a good agreement. Garabedian and Korn [30] solved the full-potential equation with the Korn airfoil for a shock of moderate strength. Then, the first three-dimensional wing calculations

using the FP formulation were published by Jameson [31], who solved the flow about an unyawed wing at M_∞=0.82 and $\alpha = 1^o$, and a yawed wing with a yaw angle of 36^o at M_∞=1.0 and $\alpha = 1.8^o$. The computations on these two cases yielded reasonable results.

All of these schemes are based on non-conservative formulation of the governing equations and are thus called non-conservative relaxation (NCR) schemes. The solutions for the NCR-schemes did not give the correct shock jump condition when compared with accurate numerical solutions which were developed later. It is known that the difference schemes for computing solutions with discontinuities need to obey the global conservation laws. As a consequence, a solution procedure using the conservative form of the full-potential equation was introduced first by Jameson [32] for two-dimensional airfoil computations. This was later extended to three-dimensional wing computations by Jameson and Caughey [33,34], who used the explicit finite-volume scheme with added dissipation terms to solve the three-dimensional full-potential equation. The computations were made on both a single ONERA wing M6 and a wing-cylinder combination for the same wing. The results compared well with experimental data for the location and strength of the shock with the exception of slight underprediction of the peak pressure.

These early works on FD methods established a very good foundation for the rapid improvements in the computational transonics which took place later on. Most of the recent work in the steady transonic potential methods has been directed toward increasing the efficiency of the computations. The Jameson conservation scheme [32] was modified by Holst [35] who introduced the upwind-biased scheme and by Hafez et al. [36] who introduced the artificial compressibility scheme. Holst [35] applied their upwind-biased scheme to subcritical flows (NACA 0012, $M_\infty = 0.63$ and $\alpha = 2^o$) and to critical flows (NACA 0012, M_∞=0.75 and $\alpha = 2^o$).

The comparisons of their results with other numerical solutions are satisfactory for subcritical flows. But for critical flows, the shock location predicted by this scheme appears to be too far downstream. The artificial compressibility scheme [36] was applied to certain thin airfoils at M_∞=0.9 to 1.1. The development of more computationally efficient methods has been accomplished by introducting the fully implicit approximate factorization (AF) methods and multigrid methods. The first solution of TSD theory for transonic flows past airfoils by using the AF-scheme was obtained by Ballhaus et al. [37] in 1978. This AF-scheme was applied to a 10%-thick airfoil at M_∞=0.84 with $\alpha = 0^o$ and the Korn airfoil at M_∞=0.7 with $\alpha = 1^o$. This scheme requires substantially less computer time than the standard successive-line over relaxation (SLOR) scheme to get the same accuracy. This increase in the computational efficiency is achieved without increase in the computer storage. After one year, the AF-scheme was extended to the two-dimensional full-potential flows by Holst [35] and to three-dimensional full-potential flows by Holst [38] again in 1980. The computational results on the two-dimensional NACA 0012 airfoil at M_∞=0.75 and $\alpha = 2^o$ and on the NACA 0015 wing at $M_\infty = 0.86$, $\alpha = 0^o$, $AR = 1.9$ and sweptback angle of 30° were reported [38]. Substantial improvement in the convergence speed was achieved. While the multigrid techniques were already developed by Brandt [39,40], South and Brandt [41] were the first to present a multigrid method by using the SLOR for transonic flow calculations. The convergence of the South and Brandt scheme [41] was five times faster than the uniform grid calculations, which reduced the computational cost significantly. Further work on reducing the computational cost is still underway.

By the 1980's, Euler equation solutions for transonic flows were introduced. Before reviewing the work on Euler equations, it is important to mention that asymmetric solutions of the conservative potential equation have been obtained

recently for symmetric flows at moderate Mach numbers [42-44]; a very disturbing computational result. Steinhoff and Jameson [43] examined this nonuniqueness by using FD schemes to solve the full-potential equation at different Mach numbers. They found that for the symmetric 11.8%-thick Joukowski airfoil at $\alpha = 0^o$, the nonuniqueness occurs only in a narrow band of Mach number, between 0.82 and 0.85. The nonunique solution at M_∞=0.832 was presented. Also, a nonunique solution was obtained for the flow around the NACA 0012 airfoil at M_∞=0.84 and $\alpha = 0^o$ in their research. Salas and Gumbert [45] have shown that the problem appears to be universal because of the isentropic-flow assumption, which is violated as the shock strength becomes finite. More recently, Fuglsang and Williams [46] have shown that the nonuniqueness can be eliminated by relatively minor modifications to potential-flow codes which account for entropy changes across a shock of finite strength. The method was applied to both steady and unsteady airfoil computations. The steady solutions for the NACA 0012 airfoil at M_∞=0.84 and $\alpha = 0^o$ and at M_∞=0.82 and $\alpha = 2^o$ showed satisfactory agreement with the Euler solutions. Later on, the concept of the entropy correction has been used in the full-potential equation by Whitlow et al. [47] for the steady and unsteady airfoil computations. The steady results for an NACA 0012 airfoil at M_∞=0.84 and $\alpha = 0^o$ showed that the nonuniqueness was removed but the shock location was still too far downstream when compared with the accurate Euler solutions. The Euler solution of transonic flows over a wide range of free-stream Mach numbers does not show any multiple solutions, since the Euler formulation does not assume isentropic flows.

During the last five years, several methods which use the strong conservative form of the unsteady Euler equation have been developed to solve for steady transonic flows. One of the excellent schemes for steady, two-dimensional transonic flows was developed by Jameson et al. [48], who used an explicit central-differencing

finite-volume method with added second and fourth-order dissipation terms. This scheme proved to be an effective tool for solving Euler equations for compressible flows, particularly for transonic flows with strong shocks. The computations were carried out on the flow around a cylinder at M_∞=0.45 with $\alpha = 0°$, and on the flow around an NACA 0012 airfoil at M_∞=0.80 and 0.85 with $\alpha = 0°$. His comparisons of the Euler results for flows with strong shocks (NACA 0012, M_∞=0.85 and $\alpha = 0°$) with his early FP solutions showed that the shock wave was further aft in the fully conservative FP calculations. This difference may have been caused by the isentropic flow assumption used in the FP formulation. Recently, an implicit finite-volume scheme for the Euler equations was developed by Caughey [49] who used a multigrid implementation of the alternating direction implicit(ADI) algorithm. Computed results for the NACA 0012 airfoil at M_∞=0.85 with $\alpha = 0°$ and at M_∞=0.80 with $\alpha = 1.25°$ were presented. An improvement in the computational efficiency as compared with the Jameson explicit scheme [48] was achieved. The accuracy, stability and convergence rate of various artificial dissipation models that are used with central-differencing algorithms for the Euler equations have been analyzed recently by Pulliam [50].

Although most of the work done is based on inviscid flow theory, transonic flows are highly influenced by viscous effects. Early work on this problem was done by Deiwert [51,52] in the mid-1970's, who used a finite-volume method to solve the time-dependent, Reynolds-Averaged Navier-Stokes equations for two-dimensional flows. Recently the two-dimensional Navier-Stokes equations were solved using the LU-ADI method by Matsushima et al. [53]. The scheme was applied to flows with strong shocks around NACA 0012 and RAE 2822 airfoils. The work on Navier-Stokes equations is outside the scope of this dissertation.

2.3.2 IE Methods for Steady Inviscid Transonics

Although a great deal of progress has been made in solving nonlinear fluid flow problems by FD methods, these methods have not yet proved to be easily adaptable to complex three-dimensional surfaces. The major difficulty is caused by the need for generating suitable grids. More recently, this difficulty and the relatively large computational time associated with FD methods prompted some researchers to reconsider the application of integral equation methods to transonic flows.

Panel methods for linearized subsonic and supersonic aerodynamic computations have been in use since the 1960's and have become indispensable tools in aerodynamic analysis and design. A review of the panel methods in this flow regime was given by Kandil and Yates [54].

Relatively little (compared with FD methods) attention has been paid, so far, to the IE methods for transonic flows. Certain appropriate IEM formulations of the transonic small-disturbance problem were studied in the pre-computer era, notably by Oswatitsch [17] and Spreiter [55] in the 1950's. Computerized and extended versions of the approximate IEM were developed later. The most notable contributions are due to Crown [56], Norsturd [57] and Nixon [58]. The solutions obtained in these pioneering works compared well with the experimental data and other computational solutions for shock-free flows at high subsonic Mach numbers. But for flows with shocks, the comparison was poor for both the shock strength and the shock location. It should be noted that the approximate IEMs, mentioned above, are all based on a special, partial-integration form of the integral equation for the TSD formulation, which enables easy implimentation of approximating assumptions on the decay of the perturbation velocity away from the body. The approximating assumptions on the decay of the pertubation velocity and the shock-fitting character of these methods are not considered to be competitive with FDMs.

In 1979, Piers and Sloof [59] first developed an IEM based on transonic small-disturbance theory. Their method does not contain any approximating assumptions and, through the introduction of artificial viscosity and directional bias, they produced a shock-capturing capability similar to that of current FDM's. The results of calculations were presented for a non-lifting 10%-thick parabolic-arc airfoil at M_∞=0.80, 0.825 and 0.85, respectively. The comparisons of these results with the other FD solutions were in good agreement for shock-free flows and for transonic flows with weak shocks.

The development of the integral equation methods based on the full-potential equation formulation started two years ago. Kandil and Yates [54] first developed an IEM for steady transonic flows past delta wings and a conical shock was captured on the suction side of the wing. The results showed that the method is promising and efficient. Also, Oskam [60] developed an IEM of the full-potential equation applied to multicomponent airfoils. These two methods are obtained by adding a field distribution of source singularities to the conventional distribution of singularities over the boundaries of the field. The comparisons of the results by Oskam [60] for the NACA 0012 airfoil at M_∞=0.80 and $\alpha = 0^o$ with the other accurate FD solutions of the full-potential equation are satisfactory. Also, the computed solution for flow around multicomponent airfoils at M_∞=0.25 and $\alpha = 14^o$ was presented and a shock was captured in the solution. At about the same time, Erickson and Strande [61] used Green's third identity to extend the panel method to non-linear potential flows, using the concept of the artificial density. An optimization technique was used to make sure that the total compressibility is conserved. This computational code was named TranAir. The code was applied to the flow around an NACA 0012 arifoil at M_∞ =0.8 with $\alpha = 0^o$ and 0.37^o, respectively. These results were found to be as accurate as other reliable FD solutions. Recently, this TranAir code was

applied to the F-16A aircraft configuration by Erickson et al. [62]. The computations were made for both subcritical and critical flows. Solutions for the flows at M_∞=0.6 and M_∞=0.9 with $\alpha = 4^o$ were presented. At M_∞=0.6 (subcritical flow), the results were generally in close agreement with the experimental data. At M_∞=0.9 (critical flow), weak shocks were captured on the wing, and the predicted pressure distributions were in fairly close agreement with the experimental data. The computations of this F-16A aircraft configuration showed that complex geometries can be represented easily since the surface-conforming field grids are not needed for IEM. Later on, another IEM for two-dimensional, steady transonic flows based on the full-potential formulation was performed by Sinclair [63], which was similar to that of Kandil and Yates [54] for three-dimensional flows. The numerical examples of both single airfoils and multicomponent airfoils were presented. The solutions for the flows around the NACA 0012 airfoil at M_∞=0.8 and $\alpha = 0^o$ were in close agreement with FD solutions to the full-potential equation, while the result for the flow with a strong shock (RAE 2822 airfoil, M_∞=0.729 and $\alpha = 2.46^o$) was not in good agreement with the FD solutions in terms of the location and the strength of the shock.

On the other hand, the development of the integral equation method based on TSD theory was continued by Ogana [64], who used the streamwise-linear-distributed field-elements to solve for two-dimensional airfoil flows. Numerical examples were made for the non-lifting flows around the 6%-thick parabolic-arc airfoil at M_∞=0.87 and the NACA 0012 airfoil at M_∞=0.80. The results were generally in good agreement with the FD solutions. This method is one of the few IE methods based on TSD theory developed during the last several years.

It is clear that, the integral equation approachs to the steady transonic flows are still in their initial stage of development. The results obtained recently using IE

methods are in good agreement with those from other numerical approach as well as with experimental data for transonic flows with weak shocks. Unfortunately, no good results for flows with strong shocks were reported by IEM. The reason behind that may be the isentropic flow assumption used in the IEM of the potential equation.

2.3.3 Experimental Work in Steady Transonics

For transonic flows, little experimental data are available compared with incompressible, subsonic, supersonic and hypersonic flows. This is due to the fact that transonic wind-tunnel tests are subject to much greater uncertainties than any other flow. The pioneering work on experimental transonics is due mainly to Liepmann [65] and Ackeret, Feldman and Rott [66]. Liepmann [65] obtained a clear schlieren photograph showing the interaction between the shock edge and the turbulent boundary-layer near the trailing edge of a profile in transonic flows. Ackeret et al. [66] got a series of photographs showing the effect of Mach number on shock wave-boundary layer interaction. Their work had helped greatly in understanding transonic flow phenomena.

The emphases of the recent experimental work on transonic flows has been extended from the significance of a local shock wave-boundary layer interaction over curved surfaces or simple airfoils to shock induced separation. Based on the extensive observations of Pearcey et al. [67] they postulated that two types of separation, called Type A and Type B separations, are permissible and both can exist in a realistic flow. Type A separation is a separation bubble formed at the foot of a near-normal shock wave adjacent to the surface, while Type B separation is flow separation from the airfoil trailing edge. Further experimental studies of these

two types of separation were continued by Yoshihara and Zonnars [68], Collins and Krupp [69], Collins [70] and Studwell [71].

Surface pressure measurements on the airfoils and wings for steady transonic flows started in the late 1950's. Knechtel [72] measured the surface pressure on a 6%-thick circular-arc airfoil at transonic speeds with weak shocks in 1959. At about this same time, the pressure measurements on the H-34 helicopter main rotor airfoil section were done [73]. The measured surface pressures at $M_\infty = 0.75$ with $\alpha = 2^o$ and at $M_\infty = 0.80$ with $\alpha = 1^o$ were reported.

Most of the steady transonic pressure measurements were made during the 1970's. The surface pressure measurements for steady transonic flows about a thin swept lifting wing with a Lockheed C-141 airfoil section at the critical condition was made by Cahill et al. [74] in 1971. The three-dimensional wing surface pressure measurements were continued by Monnerie et al. [75], who measured the surface pressure for the flow about ONERA wing M6 at M_∞=0.84 and $\alpha = 3.06^o$ with a strong shock predicted.

Several two-dimensional airfoil pressure measurements were made during the last few years. McDevitt et al. [76] measured the surface pressure for the non-lifting flows about a 18%-thick circular-arc airfoil at a wide range of Mach numbers with weak and strong shocks. Cook et al. [77,78] reported the measured results for flow about a 12%-thick circular-arc airfoil at M_∞=0.865 and $\alpha = 0^o$ [77], and for an RAE 2822 airfoil at $M_\infty = 0.729$ with $\alpha = 2.54^o$ and at $M_\infty = 0.750$ with $\alpha = 2.51^o$ [78]. Anon [79] measured the surface pressure for the MBB-A3 supercritical airfoil at design conditions. Recently, Harris [80] made pressure measurements on the NACA 0012 airfoil at large angles of attack with strong shocks. Some other steady surface pressure measurements for several standard AGARD two-dimensional airfoil configurations, such as, NACA 64A006, NACA 64A010, NLR 7301 and NACA

0012 airfoils and some non-standard AGARD airfoils, have been made in recent few years and will be reviewed in the next section along with a review of the unsteady experimental work. All of these measured surface pressure distributions provide rigorous verifications for numerical schemes.

2.4 Current Status of Unsteady Transonics

Unsteady computational transonics have been developed in parallel with the developments of the steady transonics, but with a lag of approximately five years [81] due to the additional requirement of time-accruacy. The rapid developments of unsteady transonics started in the mid-1970's from two sources: the first is the computational method of unsteady TSD theory developed by Ballhaus and Lomax [82] and the second is the pioneering experiment by Tijdeman [83] that determined pressure of unsteady transonic flows. The developments in this field since the mid-1970's will be reviewed in the following sub-sections.

2.4.1 FD Methods for Unsteady Inviscid Transonics

The development of inviscid unsteady finite-difference methods has also been based on three levels of mathematical approximations: (i) TSD formulations, (ii) FP formulations, and (iii) Euler equation formulations. Most of the available methods are based on the TSD formulation.

The unsteady two-dimensional solution based on the TSD formulation was first obtained by Ballhaus and Lomax [82] who applied semi-implicit methods to the general TSD equation and its low-frequency approximation. Next Ballhaus and Steger [84] developed a fully implicit scheme which used an ADI-scheme for the low-frequency TSD equation. Then this ADI-scheme was implemented into a computer code LTRAN2 by Ballhaus and Goorjian [85]. The code was applied

to the computations of the low-frequency unsteady flap oscillations of an NACA 64A006 airfoil under transonic speeds. Tijdeman's experimental observations of Type A, B and C shock wave motions (see Sec. 2.4.3) resulting from airfoil flap oscillations were qualitatively reproduced by this code. The computational time required by this implicit ADI algorithm is substantially less than that of the semi-implicit scheme.

Further developments of the scheme used in LTRAN2 were made by Houwink and van der Vooren [86] and by Couston and Angelin [87]. To extend the frequency range, they solved the low-frequency TSD equation with added high-frequency terms to the wake condition and the pressure calculation. The computations were made for flows about an NACA 64A006 airfoil oscillating in pitch with a reduced frequency based on the chord length, k_c=0 to 0.8. Moreover, Rizzetta and Chin [88] extended the frequency range further by including a high-frequency term in the governing equation, and the scheme was implemented into a computer code ATRAN2. The reduced frequency range, k_c=0.05 to 5.0, was examined using both ATRAN2 and LTRAN2 codes, and good agreement between the results obtained by ATRAN2 and LTRAN2 was found only for the lower frequencies. This indicates the importance of the unsteady terms in high-frequency motions. Whitlow [89] further modified the GTRAN2 code by replacing the Murman-Cole (M-C) type-difference by the Engquist- Osher (E-O) monotone-difference scheme and by using non-reflecting boundary conditions. The method was implemented into the computer code XTRAN2L TSD. The test on the M-C type-differencing scheme and the E-O monotone-differencing scheme was made. The results showed that the E-O monotone-differencing scheme was much more stable than the M-C type-differencing scheme during the unsteady computations. A test on the reflecting and non-reflecting unsteady boundary conditions was also made. The results with

non-reflecting boundary conditions showed good agreement with the reference solutions. A computational scheme for three-dimensional unsteady transonic flows based on the complete TSD equation was developed by Borland and Rizzetta [90] and this computational code is named as XTRAN3. Further study of the XTRAN3 code was made by Gibbons et al. [91]. The non-lifting steady flows over a rectangular wing with an NACA 0012 airfoil section and an aspect ratio of 12 were computed for M_∞=0.82, 0.84 and 0.86. A nonunique solution was observed for the flows at M_∞=0.84 when the aspect ratio became larger than 24. The steady and unsteady solutions were also presented for the RAE tailplane model at M_∞ =0.90 and $\alpha = -0.3°$, and comparison with the experimental data was generally in good agreement. Nearly continuous study of the application of the TSD theory has been made by Edwards et al. [92], Bland and Seidel [93], Goorjian and Guruswamy [94], Malone et al. [95], and Edwards [96] in the mid-1980's. The numerious numerical examples were calculated for several AGARD two-dimensional aeroelastic configurations: NACA 64A006, NACA 64A010A, NACA 0012, MBB-A3 and NLR 7301 airfoils, and for a three-dimensional F-5 wing and AGARD rectangular wings [92-96]. The several types of unsteady motions, such as, pitching oscillation of the airfoil, flap oscillations and transient ramping motions, were simulated. For most of the cases, the comparisons of the results with other numerical solutions and experimental data were made, and they rated from very good to fair. A recent notable contribution to TSD theory is the introduction of the concept of entropy correction across the shock, which was first applied to two-dimensional flows by Fuglsang and Williams [46], as discussed before.

The algorithm developments of the implicit-scheme to full-potential equation formulations were started by Isogai [97], who developed a semi-implicit algorithm for the conservative full-potential equation. Soon after, Chipman and Jameson [98] have

developed a conservative implicit algorithm that used a time-varying coordinate system to satisfy the exact boundary conditions. The time-accurate calculations have been made for the pulsating problem of a thickening-thining circular-arc airfoil at $M_\infty = 0.85$ and $\alpha = 0^o$ with the thickness ratio changing from 0% to 10%, and for a 10%-thick circular-arc airfoil with flap oscillation under $M_\infty = 0.8$ and a mean angle of attack, $\alpha_o = 0^o$. The results were in good agreement with the more accurate Euler solutions. Shock location and strength were predicted better by this conservative full-potential solution than by either the TSD theory or the non-conservative full-potential equation. Further developments on this scheme have been reported by Goorjian [99] and Chipman and Jameson [100]. Goorjian [99] used time-linearization of the density function to reduce the solution process from one of solving a system of two equations to one of solving a single equation. This ADI implicit scheme was applied to the same airfoil-thickening-thining problem as that of Chipman and Jameson [98]. Comparisons of these results with Chipman and Jameson's [98] results showed a close agreement. Chipman and Jameson [100] used both density and velocity potential as dependent variables rather than the velocity potential only which was the case in their previous method [98], resulting in a simple system of two equations. This scheme had excellent stability and yielded accurate solutions when applied to a pulsating airfoil. Recently, the idea of an entropy correction has been used in the full-potential solution by Whitlow et al. [47] and applied to the unsteady two-dimensional computations. The numerical example has been presented for flow about the NACA 0012 airfoil under pitch motions about its quarter-chord at $M_\infty = 0.755$ and an amplitude of 2.51^o about the mean angle of attack of 0.016^o. Reduced frequency based on the half-chord length, k_{ch}, is 0.0814. Their results were in good agreement with experimental data for flows with strong shocks.

The unsteady transonic solution of the Euler equation formulation also started in the mid-1970's. Magnus and Yoshihara [101] solved the Euler equations for two-dimensional flows using an explicit algorithm. They solved the Euler equations with and without a viscous ramp for an NACA 64A006 airfoil at $M_\infty = 0.875$ with a quarter-chord flap oscillation. The use of viscous ramps was found to reduce the difference between the inviscid Euler results and the experimental data. This explicit Euler scheme was also applied to an NACA 64A010 airfoil in pitching and plunging motions at $M_\infty = 0.80$ by Magnus [102], and to a blunt-nosed, 16.5%-thick, NLR 7301 airfoil under pitching $\pm\ 0.5^o$ by Magnus [103] again. Later on, Chyu et al. [104] solved both Euler equations and Navier-Stokes equations using an implicit scheme for an NACA 64A010 airfoil undergoing pitch oscillations of $\pm\ 1^o$ amplitude about its quarter-chord with a reduced frequency, $k_{ch} = 0.2$, at $M_\infty = 0.80$. Comparisons of their results with the experimental data showed good agreement for both solutions. The computational time used by this implicit scheme was reduced significantly when compared to explicit schemes. Recently, the unsteady conservative Euler equations in the moving frame of reference have been solved by Kandil and Chuang for a pitching oscillation around a mean angle of attack of an NACA 0012 airfoil in transonic flow [105,106] and for a locally conical supersonic flow with rolling oscillations of a sharp-edged delta wing at zero mean angle of attack [105,107]. The airfoil solutions were obtained by using a time-accurate solution of an implicit, approximately-factored finite-volume Euler solver, and the delta wing solutions were obtained by using time-accurate solutions of an explicit finite-volume Euler solver. The results for the NACA 0012 airfoil in pitching motion at transonic speeds showed good agreement with the experimental data. Time-accurate solutions of the unsteady Euler equations have also been presented for pitching airfoils by Anderson, Thomas and Rumsey [108]. They solved the Euler equations by

using the flux-vector splitting and the flux-difference splitting methods extended for dynamic meshes. The Euler equations have been solved for three-dimensional unsteady transonic flows and the results for this type of solution are given in reference [109-113]. Some numerical examples can be found in these references, such as the results for an F-5 wing configuration, pitching at $\pm$ 0.113° with a frequency of 40 hz at $M_\infty = 0.8$ and mean angle of attack of 0° by Sankar et al. [113].

Methods used for unsteady viscous flows are not reviewed here. This type of flow modeling includes interactive viscous modeling, shock induced boundary-layer separation modeling and wake separation modeling, etc. Edwards and Thomas [114] presented a very extensive review of this field. An example of the solution of unsteady viscous flow problems is given by Rumsey and Anderson [115]; they solved the thin-layer Navier-Stokes equations for unsteady laminar and turbulent transonic flows past a pitching NACA 0012 airfoil at transonic speeds.

2.4.2 IE Methods for Unsteady Inviscid Transonics

Integral equation methods for unsteady transonic flows received little attention until recently. Nixon [116] first developed an integral equation method for a harmonically oscillating airfoil using transonic small-disturbance theory which was a pioneering work for unsteady IE methods. The method was applied to computations for non-lifting flows about a 10%-thick biconvex airfoil at $M_\infty = 0.808$ pulsating in thickness between 9% and 11% of the chord length with a reduced frequency k_c of 0.1 , and to the flow about an NACA 0012 airfoil at M_∞=0.8 and a mean angle of attack of 0° oscillating in pitch at $\pm$ 0.5° about the mid-chord with reduced frequency, k_c, of 0.2. The motion of the weak shock was predicted by this scheme. The principle disadvantage of the method is the restriction that shock waves cannot be lost or generated during the motion, due to the use of a strained coordinate system

in treating the shock motion. This restriction eliminates the study of important nonlinear shock motion effects. After three years, Hounjet [117] developed another two-dimensional TSD integral equation method. This method combined supersonic and subsonic linear lifting surface theories, which are based on the velocity potential panel approach with an account for the moving shock effect. The unsteady load calculations were performed for an NACA 64A006 airfoil at $M_\infty = 0.875$ and $\alpha = 0^o$ under the pitching oscillation and the oscillating flap motions. The comparisons of the calculated unsteady loads with those obtained by LTRAN2 code developed by NLR showed a good agreement. The computational time used in this IEM is 5% of that necessary for the LTRAN2 code, which makes this approach attractive. Unfortunately, these two methods are restricted to small motion of airfoils.

Later, Tseng and Morino [118] developed a nonlinear Green's function method (IEM) for three-dimensional unsteady transonic flows based on TSD formulations. The unsteady loads on a rectangular wing of aspect ratio, $AR = 5$, with a NACA 64A006 section at $M_\infty = 0.875$ under a small amplitude and low frequency pitching motion were presented. The results showed satisfactory agreement with the FD solutions. Recently, a hybrid method for calculating time-linearized unsteady transonic potential flows was developed by Hounjet [119]. The method combined the advantages of the FDM and the IEM in that the computational time was reduced. The FDM was adopted to deal with the fast local variations of the flow variables in the immediate neighborhood of the body, while the IEM described the smoother variations at some distance away from the body. The corresponding computer code was named as FTRAN3, and it was applied to several wing planforms, and weak shocks were capured by this code.

2.4.3 Experimental Work in Unsteady Transonics

Due to the wall interference problem, unsteady transonic experiments are more difficult to carry out than those for steady transonic flows. Erickson and Robinson [120] made the first local unsteady transonic pressure measurements on an oscillating wind-tunnel model, but they only reported overall aerodynamic coefficients. Twelve years later in 1960, Lessing et al. [121] and Leadbetter et al. [122] published the first detailed unsteady transonic pressure distribution measurement over oscillating wings.

By the mid-1970's, after a series of investigations made by the NLR of the Netherlands [123-129], Tijdeman [127] divided flows over airfoils with oscillating flaps into three different types of periodic shock wave motions, named Type A, Type B and Type C motions as mentioned previously. This classification was one of the most significant contributions to interpreting unsteady transonic experiments. For Type A motion, the shock moves almost sinusoidally and persists during the complete cycle of the sinusoidally pitching oscillation of the flap. For Type B motion, the motion of the shock is similar to that of Type A motion, except that the change of the shock strength during the motion is larger than the mean steady shock strength and thus the shock may disappear during the cycle. Type C motion is totally different from Type A and Type B motions, which is an upstream propagated shock wave motion. The shock wave is formed periodically on the airfoil upper surface. This shock wave moves upstream while the strength of the shock is increased at begining and then the strength of the shock is decreased. Finally, the shock wave leaves the airfoil from the leading edge to propagate upstream into the incoming flow as a shock-free wave. This phemomenon is repeated periodically and alternates between the airfoil upper and lower surfaces. This phenomenon of Type C motion happens when M_∞ is slightly greater than M_{crit}. The types of the shock

wave motions that occur depend on the free-stream Mach number, the amplitude and the frequency of the flap oscillations.

Another notable contribution in experimental study of unsteady transonics at that time is due to Grenon and Thers [130], who observed that an almost linear relationship exists between the frequency of oscillation and the phase shift between the motion of the airfoil and the motion of the shock wave for low to moderate frequencies.

The period from the late 1970's to the early 1980's is the period of the rapid developments of experimental unsteady transonics. Some transonic unsteady load and surface pressure measurements for the standard AGARD two-dimensional airfoils and three-dimensional wings were made during this period.

Tijdeman and Schippers [125] measured the surface pressure on an NACA 64A006 airfoil for steady and unsteady flows. For the steady flows, the surface pressure distributions at $\alpha = 0^o$ and $M_\infty = 0.80$ to 0.96 were presented, which corresponded to shock-free flows and transonic flows with weak shocks, respectively. For the unsteady flows, the measurements were made for the oscillation of a flap with its hinge axis located at the three-quarter-chord about a zero mean angle of attack. The surface pressure distributions were presented for many AGARD standard cases, mainly for $M_\infty = 0.825$ to 0.96, the flap oscillation amplitude, $\alpha_a = 1^o$ and 2^o, and a reduced frequency, which is based on the half -chord length, of $k_{ch} = 0.064$ to 0.254.

For a NACA 64A010 airfoil, the steady and the unsteady teansonic flow measurements were made by Davis and Malcolm [131]. For the steady flows, the measured surface pressure distributions were reported for M_∞=0.49 to 0.802 at $\alpha = 0^o$. The motion of the unsteady flow was for an airfoil pitch oscillation about its quarter-chord length at a zero mean angle of attack. The measured surface pressure

distributions were presented for various AGARD standard cases, mainly for M_∞ = 0.5 and 0.8, $\alpha = 1^o$ and 2^o, and reduced frequencies, k_{ch}=0.01 to 0.3.

Extensive pressure measurements on the unsteady transonic flows were made by Landon [132] for an NACA 0012 airfoil, who published the measured time history of the surface pressure distributions for the airfoil pitch oscillation and ramp motion about its quarter-chord and for quasi-steady motions. For the pitch oscillation, the results presented include the cases of M_∞ =0.755 with mean angle of attack, $\alpha_o = 0.016^o$, and the amplitude, $\alpha_a = 2.51$, and of $M_\infty = 0.60$ with $\alpha_o = 2.89^o$ to 4.86^o and $\alpha_a = 2.41^o$ to 4.59^o, at the reduced frequency, $k_{ch} = 0.08$. For the ramp and quasi-steady motions, the results for $M_\infty = 0.30$ to 0.75, and $\alpha = -3.27^o$ to 15.55^o, were presented.

Pressure measurements have been done for a 16%-thick supercritical NLR 7301 airfoil by Tijdeman [133] for steady and unsteady flows. For steady flows, the surface pressure distributions were measured for the flows at a subcritical condition at $M_\infty = 0.5$ and $\alpha = 0^o$, a supercritical condition with a shock at $M_\infty = 0.7$ and $\alpha = 2^o$, and the design condition at $M_\infty = 0.721$ and $\alpha = -0.19^o$. For unsteady flows, the pressure distributions for the airfoil pitch oscillations about its 40% chord and flap oscillations located at three-quarter-chord with various frequencies and amplitudes at these three conditions were presented.

Recently, the steady and unsteady flows about a 14%- thick model supercritical airfoil, Sc(2)-0714, were tested by Hess et al. [134]. At M_∞ =0.72 and four angles of attack of 0^o, 1.5^o, 2.0^o and 2.5^o, the steady surface pressure distributions were presented. The unsteady surface pressure measurements were made for the airfoil oscillation in pitch about a mean angle of attack of 1^o and 2^o, at amplitides of 0.25^o to 1.0^o, with a frequency range from 5 hz to 60 hz.

Along with the two-dimensional experimental data measurements, the three-dimensional unsteady pressure measurements for flows past wing configurations were made. Tijdeman et al. [135] measured the surface pressure on an F-5 wing under pitch oscillations at $M_\infty = 0.9$, $\alpha_o = 0^o$, $\alpha_a = 0.109^o$ and $k_{ch} = 0.137$. Similar work was done by Horsten et al. [136] for a LANN wing, and by Mabey et al. [137] for an RAE wing. The results for the LANN wing, pitching oscillation about a mean angle of attack of 0.62^o at $M_\infty = 0.82$, $\alpha_a = 0.25^o$ and $k_{ch} = 0.076$, were available from Horsten et al. [136]; while for the RAE wing, the results for the pitching oscillation at 70 hz about a mean angle of attack of -0.30° with an amplitude of 0.57^o at M_∞=0.90 were avaiiable from Mabey et al. [137].

This work on the pressure measurements provided very reliable data for comparisons with the computational results. They helped the rapid development of computational unsteady transonics.

2.5 Summary

The study of the recent developments on the computational transonics shows that the integral equation methods have a very good potential to challenge finite-difference methods in the field of inviscid transonics due to the obvious advantages mentioned. Furthermore, if the integral equation methods are combined with finite-difference methods, the possibility to handle flows with strong shocks exists. In this hybrid IE-FD method, the IE solution can be used in the far-field to satisfy boundary conditions of a small FD domain. This method would result in a significant reduction in the size of the FD computational domain. It is not clear, however, if the integral equation methods will ever replace the present mainstream techinque FD methods in some fields of inviscid transonics. It is always beneficial to consider different viewpoints of the same problem.

Chapter 3

FORMULATION OF THE PROBLEM

In the first section of this chapter, we consider the physical aspects of the full-potential and the Euler equation formulations. In the second section, we first describe briefly the physical problem to be solved. This is then followed by the derivation of the general unsteady three-dimensional full-potential equation along with the associated boundary conditions in the body-fixed moving frame of reference. The governing equations and the boundary conditions are then specialized for two-dimensional steady and unsteady flows. In the next section, integral equation solutions are presented. For the embedded Euler domain method, the Euler equations and the boundary conditions are given. Finally we end this chapter with a brief discussion on the validity of the IE method for transonic flows.

3.1 Physical Aspects of Flow Modeling

The Navier-Stokes equations are generally accepted as the most basic governing equations for fluid dynamic phenomena of interest to aerodynamicists. The equations are capable of representing the most general transonic flows, including mixed subsonic-supersonic flows, shock waves, separations and boundary-layers including turbulent flows. But, because of the present computer speed and capacity, it is not possible to solve all of those flows using the Navier-Stokes equations for practical aerodynamic configurations.

Different levels of approximations to the Navier-Stokes equations are available. For large Reynolds numbers, viscous effects are small compared to inviscid effects, and in the limiting case where $\mu \rightarrow 0$ and $k \rightarrow 0$, the Navier- Stokes equations reduce to the Euler equations. Since the limiting process changes the order of the governing equations from second-order (Navier-Stokes equations) to first-order (Euler equations), one cannot satisfy all the boundary conditions. Moreover, singular-limiting surfaces appear in the flow field. They model regions with large gradients in flow properties in real flows by reducing them to surfaces of mathematical discontinuities in the Euler limit. In addition, by introducing isentropic flow and irrotational flow assumptions the full-potential equation is obtained. Further simplification is the transonic small-disturbance (TSD) equation, which is the simplest equation that can describe transonic flows with shocks. However, the TSD theory has some significant limitations. Only flows past bodies of small thickness at small angles of attack and undergoing small amplitude, unsteady motions can be modeled adequately since their transonic flow is characterized with weak shocks. Because of these limitations, the TSD theory will not be used in this work. A brief discussion of the full-potential equation and the Euler equation formulations for transonic flows will be given in the following paragraphs.

The Euler equations generally represent all inviscid rotational flows in all speed ranges. In an inviscid flow, the energy equation can be written as [138],

$$\frac{DS}{Dt} = 0 \tag{3.1}$$

providing that there are no singular surfaces in the flow field. Therefore, the only mechanism for generating entropy changes in an inviscid flow is through the presence of singular surfaces - shock waves. It may be shown [138] that the entropy rise, ΔS,

through a shock wave is of order $(M_{1n}^2 - 1)^3$, or

$$\frac{\Delta S}{R} = \frac{2\kappa}{3(\kappa+1)}(M_{1n}^2 - 1)^3 + O(\epsilon^4) \tag{3.2}$$

where M_{1n} is the normal component of the local Mach number ahead of the shock, κ the gas specific heat ratio, R the gas constant, and the small parameter ϵ is given by $\epsilon = M_{1n}^2 - 1$; while other flow variable changes are of order $(M_{1n}^2 - 1)$. For example, the change of the pressure across the shock, Δp, is given by

$$\frac{\Delta p}{p_1} = \frac{2\kappa}{\kappa+1}(M_{1n}^2 - 1) + O(\epsilon^2) \tag{3.3}$$

where p_1 is the pressure ahead of the shock. If the shock wave is sufficiently weak such that

$$(M_{1n}^2 - 1)^3 \ll (M_{1n}^2 - 1) \tag{3.4}$$

then the entropy production is a negligible higher-order effect compared with those of other flow variables. Therefore, the homentropic flow assumption can be used for the flow where the value of $(M_{1n}^2 - 1)$ is small.

Crocco's theorem gives the relation between the vorticity production and the changes of the other field variables. For inviscid flows, it is given by

$$\vec{\zeta} \times \vec{V} = T\nabla S - \nabla h_t - \frac{\partial \vec{V}}{\partial t} \tag{3.5}$$

where $\vec{\zeta}$ is the vorticity given by $\vec{\zeta} \equiv \nabla \times \vec{V}$; h_t is the total enthalpy and the term ∇h_t is zero for homoenergetic flows. For a steady, inviscid, homoenergetic flow, Crocco's theorem reduces to

$$\vec{\zeta} \times \vec{V} = T\nabla S \tag{3.6}$$

This equation tells us that the vorticity production is the same order as that of the entropy gradient if T and $\vec{V}$ are both of order 1, and that the assumption of homentropic flows yields directly the assumption of irrotational flow. Under the

assumptions of homentropic and irrotational flow, the full-potential equation is thus obtained, and it is probably the most appropriate modeling equation for transonic flows with shocks of moderate strength. The full-potential equation formulation is used in present reaserch work. The well developed integral equation methods of linear potential flows will be extended to treat nonlinear transonic flows.

Experience has shown that rather accurate solutions can be obtained for many transonic flows using the full-potential equation. The equation can be shown to express conservations of mass, momentum and energy, neglecting the effects due to viscosity, vorticity and entropy production. For transonic flows without strong shocks and massive separation, the full-potential equation is an adequate approximation to the Navier-Stokes equations.

But for flows with strong shocks, where the entropy increase and vorticity production are not negligible because of large $(M_{1n}^2 - 1)$, the full-potential equation formulation breaks down if none of these effects are taken into account. Here the Euler equations are more appropriate for modeling the flow. The Euler equations admit more accurate solutions for transonic flows with strong shocks because the equations do not assume isentropic flows and moreover they contain the vorticity term. However, with the Euler equations, there are, in general, five nonlinear differential equations instead of one equation as in the full-potential formulation, which greatly increases the computational cost. And as mentioned above, it is known that the rotational effects and entropy changes are confined to a small region behind the strong shocks. Thus, the Euler equations can be solved in this small region while the integral solution of the full-potential equation is used outside of that region. This is the idea of the IE with embedded Euler domain scheme. The purposes of this scheme are to extend IE method of the full-potential equation to treat transonic flows with strong shocks and to reduce the computational time.

3.2 Full-Potential Equations

In this section, the physical problems to be solved are first introduced. This is then followed by the derivation of the governing equations and the related boundary conditions.

3.2.1 Physical Problems

Figures 3.1 and 3.2 show the physical problems studied and the coordinate systems used in the present research. Figure 3.1 shows the steady flow cases; while Fig. 3.2 shows the unsteady flow cases.

In Fig. 3.1, an airfoil is placed in a subsonic free-stream. When the flow reachs airfoil surfaces it will accelerate to supersonic speeds and then it will decelerate to subsonic speeds by means of a shock wave as shown in Fig. 2.2. The solution of the pressure distribution over airfoil surfaces with the location and the strength of the shock is very important for aerodynamicists. Transonic steady flow computations over a wide range of Mach number have been made in the present research work.

In Fig.3.2, a body-fixed frame of reference is attached to the airfoil which is translating at a subsonic speed of $\vec{V}_o$, and rotating at an angular velocity of $\dot{\alpha}\vec{k}$. For unsteady transonic flows, the moving coordinate formulation has been used, where the source of the unsteadiness in the flow has been introduced through the motion of the airfoil-fixed frame of reference. In the present research, the sinusoidal pitch oscillation around a pivot point has been studied as a numerical example. The oscillation function in terms of angles of attack, $\alpha(t)$, is given by

$$\begin{aligned} \alpha(t) &= \alpha_o + \alpha_a \sin(\omega\tau) \\ &= \alpha_o + \alpha_a \sin(k_c t) \end{aligned} \tag{3.7}$$

where, α_o is the mean angle of attack, α_a the pitch amplitude, ω the frequency and k_c the reduced frequency based on the chord length ($k_c = \omega c/|\vec{V}_o|$,$V_o$ is the

characteristic speed and c the chord length), τ is the dimensional time and t the non-dimensional time ($t = \tau|\vec{V_o}|/c$).

3.2.2 General Unsteady Full-Potential Equation

In this subsection we derive the full-potential equation in the moving frame of reference for general three-dimensional unsteady flows. Then, the equation is reduced to that of two-dimensional steady and unsteady flows in the subsequent two subsections, respectively.

For a general unsteady motion of a body, the governing equations are simple to solve if the body-fixed frame of reference formulation is used. In addition to the space-fixed frame of reference OXYZ, we introduce the body-fixed frame of reference oxyz, which is also known as the moving frame of reference as shown in Fig. 3.3. The moving frame of reference oxyz is translating at a velocity of $\vec{V_o}(t)$ and rotating around a pivot point, $\vec{r_p}$, at an angular velocity of $\vec{\Omega}(t)$. Next, we derive the equation of absolute motion of a fluid particle in the moving frame of reference.

The continuity and momentum equations for unsteady, inviscid compressible flows with negligible body forces in a space fixed frame of reference OXYZ are given by

$$\frac{D\rho}{Dt} + \rho\nabla\cdot\vec{V} = 0 \tag{3.8}$$

$$\rho\frac{D\vec{V}}{Dt} + \nabla p = 0 \tag{3.9}$$

where ρ and p are the density and the pressure, respectively, while $\vec{V}$ is the absolute velocity.

By introducing the body fixed moving frame of reference described above, we have following relations:

$$\vec{V} = \vec{V_r} + \vec{V_e} \tag{3.10}$$

$$\vec{V}_e = \vec{V}_o + \vec{\Omega} \times \vec{r} \tag{3.11}$$

where $\vec{r}$ denotes the radius vector in the moving frame of reference of the fluid particle measured from the pivot point, $\vec{r}_p$, $\vec{V}_r$ is the relative velocity of the fluid particle with respect to the moving frame oxyz; and $\vec{V}_e$ is the transformation velocity vector of the moving frame

The substantial derivative of a scalar quantity like ρ is related to its substantial derivative in the moving frame and to the local derivative in the moving frame by the equation

$$\frac{D\rho}{Dt} = \frac{D'\rho}{Dt} = \frac{\partial'\rho}{\partial t} + \vec{V}_r \cdot \nabla\rho \tag{3.12}$$

On using Eq. (3.10), Eq. (3.12) becomes

$$\frac{D\rho}{Dt} = \frac{D'\rho}{Dt} = \frac{\partial'\rho}{\partial t} + (\vec{V} - \vec{V}_e) \cdot \nabla\rho \tag{3.13}$$

where the prime ($'$) refers to the time derivative with respect to the moving frame. Combining Eqs. (3.8) and (3.13), the continuity equation becomes

$$\frac{\partial'\rho}{\partial t} + \nabla \cdot (\rho\vec{V}) - \vec{V}_e \cdot \nabla\rho = 0 \tag{3.14}$$

Also, we can write the substantial derivative of a vector quantity like $\vec{V}$ as follows:

$$\begin{aligned} \frac{D\vec{V}}{Dt} &= \frac{D'\vec{V}}{Dt} + \vec{\Omega} \times \vec{V} \\ &= \frac{\partial'\vec{V}}{\partial t} + \vec{V}_r \cdot \nabla\vec{V} + \vec{\Omega} \times \vec{V} \end{aligned} \tag{3.15}$$

On using Eq. (3.10), Eq. (3.15) becomes

$$\frac{D\vec{V}}{Dt} = \frac{\partial'V}{\partial t} + \vec{V} \cdot \nabla\vec{V} - \vec{V}_e \cdot \nabla\vec{V} + \vec{\Omega} \times \vec{V} \tag{3.16}$$

But $\vec{V}_e \cdot \nabla\vec{V}$ can be expanded as follows:

$$-\vec{V}_e \cdot \nabla\vec{V} = -\nabla(\vec{V} \cdot \vec{V}_e) + \vec{V} \cdot \nabla\vec{V}_e + \vec{V} \times (\nabla \times \vec{V}_e) + \vec{V}_e \times (\nabla \times \vec{V}) \tag{3.17}$$

Since

$$\begin{aligned}\vec{V}\cdot\nabla\vec{V}_e &= \vec{V}\cdot\nabla(\vec{V}_o+\vec{\Omega}\times\vec{r})\\ &= \vec{V}\cdot\nabla(\vec{\Omega}\times\vec{r}) \qquad (3.18a)\\ &= \vec{\Omega}\times\vec{V}\end{aligned}$$

and

$$\begin{aligned}\vec{V}\times(\nabla\times\vec{V}_e) &= \vec{V}\times[\nabla\times(\vec{V}_o+\vec{\Omega}\times\vec{r})]\\ &= 2\vec{V}\times\vec{\Omega} \qquad (3.18b)\\ &= -2\vec{\Omega}\times\vec{V}\end{aligned}$$

Eq. (3.17) can be written as

$$-\vec{V}_e\cdot\nabla\vec{V} = -\nabla(\vec{V}\cdot\vec{V}_e) - \vec{\Omega}\times\vec{V} + \vec{V}_e\times(\nabla\times\vec{V}) \qquad (3.19)$$

Substituting Eq. (3.19) into Eq. (3.16), one obtains

$$\frac{D\vec{V}}{Dt} = \frac{\partial'\vec{V}}{\partial t} + \vec{V}\cdot\nabla\vec{V} - \nabla(\vec{V}\cdot\vec{V}_e) + \vec{V}_e\times(\nabla\times\vec{V}) \qquad (3.20)$$

On using the identity

$$\vec{V}\cdot\nabla\vec{V} = \nabla\left(\frac{V^2}{2}\right) - \vec{V}\times(\nabla\times\vec{V})$$

into Eq. (3.20), we obtain

$$\begin{aligned}\frac{D\vec{V}}{Dt} &= \frac{\partial'\vec{V}}{\partial t} + \nabla\left(\frac{V^2}{2}\right)\\ &\quad - \vec{V}\times(\nabla\times\vec{V}) - \nabla(\vec{V}\cdot\vec{V}_e) + \vec{V}_e\times(\nabla\times\vec{V})\\ &= \frac{\partial'\vec{V}}{\partial t} + \nabla\left(\frac{V^2}{2} - \vec{V}\cdot\vec{V}_e\right)\\ &\quad - (\vec{V}-\vec{V}_e)\times(\nabla\times\vec{V})\end{aligned} \qquad (3.21)$$

Combining Eq. (3.21) with Eq. (3.9), one obtains the momentum equation of absolute motion in the moving frame of reference as follows:

$$\frac{\partial'\vec{V}}{\partial t} + \nabla\left(\frac{V^2}{2} - \vec{V}\cdot\vec{V}_e\right) - (\vec{V}-\vec{V}_e)\times(\nabla\times\vec{V}) + \frac{1}{\rho}\nabla p = 0 \qquad (3.22)$$

If we assume that the absolute motion is irrotational, then we have a zero vorticity, $\vec{\varsigma}$,

$$\vec{\varsigma} \equiv \nabla \times \vec{V} = 0 \tag{3.23}$$

By introducing the velocity potential, Φ, one gets

$$\vec{V} = \nabla' \Phi = \nabla \Phi \tag{3.24}$$

Thus, Eq. (3.22) becomes

$$\nabla \frac{\partial' \Phi}{\partial t} + \nabla \left[\frac{(\nabla \Phi)^2}{2} - \nabla \Phi \cdot \vec{V}_e \right] + \frac{1}{\rho} \nabla p = 0 \tag{3.25}$$

Integrating Eq. (3.25) with respect to space, we obtain

$$\frac{\partial' \Phi}{\partial t} + \frac{(\nabla \Phi)^2}{2} - \nabla \Phi \cdot \vec{V}_e + \int \frac{dp}{\rho} = f(t) \tag{3.26}$$

For a barotropic fluid, one can find that

$$\int \frac{dp}{\rho} = \frac{a^2}{\kappa - 1} \tag{3.27}$$

where a is the speed of sound. If the fluid is at rest at infinity, then Eq. (3.26) and Eq. (3.27) yield

$$f(t) = \frac{a_\infty^2}{\kappa - 1} \tag{3.28}$$

where the subscript ∞ refers to the infinity condition. Substituting Eqs. (3.27) and (3.28) into Eq. (3.26), one gets

$$\frac{\partial' \Phi}{\partial t} + \frac{(\nabla \Phi)^2}{2} - \nabla \Phi \cdot \vec{V}_e + \frac{a^2}{\kappa - 1} = \frac{a_\infty^2}{\kappa - 1} \tag{3.29}$$

Now, we assume that the flow is isentropic, and hence we can use the isentropic relation

$$\frac{\rho}{\rho_\infty} = \left(\frac{a^2}{a_\infty^2} \right)^{\frac{1}{\kappa - 1}} \tag{3.30}$$

into Eq. (3.29). This yields the equation for density as follows:

$$\frac{\rho}{\rho_\infty} = \left\{1 - \frac{\kappa-1}{2a_\infty^2}\left[(\nabla\Phi)^2 + 2\left(\frac{\partial'\Phi}{\partial t}\right) - 2\nabla\Phi\cdot\vec{V}_e\right]\right\}^{\frac{1}{\kappa-1}} \tag{3.31}$$

The continuity equation, Eq. (3.14) can be rewritten in the form

$$\frac{1}{\rho}\frac{\partial'\rho}{\partial t} + \nabla\cdot\vec{V} + \vec{V}\cdot\frac{\nabla\rho}{\rho} - \vec{V}_e\cdot\frac{\nabla\rho}{\rho} = 0$$

or,

$$\nabla\vec{V} = -\frac{\nabla\rho}{\rho}\cdot(\vec{V} - \vec{V}_e) - \frac{1}{\rho}\frac{\partial'\rho}{\partial t} \tag{3.32}$$

Using Eq. (3.24), Eq. (3.32) becomes

$$\nabla^2\Phi = -\frac{\nabla\rho}{\rho}\cdot(\nabla\Phi - \vec{V}_e) - \frac{1}{\rho}\frac{\partial'\rho}{\partial t} \tag{3.33}$$

Equation (3.33) is the unsteady full-potential equation in the moving frame of reference with the density given by Eq. (3.31). After introducing the characteristic parameters of $|\vec{V}_o|$, ρ_∞ and length l, and defining the free-stream Mach number as $M_\infty = |\vec{V}_o|/a_\infty$, Eqs. (3.33) and (3.31) take the dimensionless form as follows:

$$\nabla^2\Phi = -\frac{\nabla\rho}{\rho}\cdot(\nabla\Phi - \vec{e}_o - \vec{\Omega}\times\vec{r}) - \frac{1}{\rho}\frac{\partial'\rho}{\partial t} \tag{3.34}$$

and

$$\begin{aligned}\rho = \Big\{1 + \frac{\kappa-1}{2}M_\infty^2\big[&-(\nabla\Phi - \vec{e}_o - \vec{\Omega}\times\vec{r})^2 \\ &+ (\vec{e}_o + \vec{\Omega}\times\vec{r})^2 - 2\big(\frac{\partial'\Phi}{\partial t}\big)\big]\Big\}^{\frac{1}{\kappa-1}}\end{aligned} \tag{3.35}$$

where $\vec{e}_o = u_o\vec{i} + v_o\vec{j} + \omega_o\vec{k}$ is a unit vector parallel to $\vec{V}_o$. All quantities in the above two equations are dimensionless, although the same notations are used.

Equation (3.34) is the desired full-potential equation in the moving frame of reference with the density given by Eq.(3.35). It should be noted that the formulation in terms of the moving frame of reference does not introduce artificial accelerations

since the velocity terms associated with the moving frame of reference are algebraic terms. Next, we consider the associated boundary conditions:

(i) Surface No-Penetration Condition: This condition states that there is no flow across the body surfaces, or that the normal component of the velocity relative to the body surface is zero at the surface. This condition is given by

$$\frac{Dg}{Dt} = \frac{\partial' g}{\partial t} + \vec{V}_r \cdot \nabla g = 0$$

Divided by $\mid \nabla g \mid$, we obtain

$$\frac{1}{\mid \nabla g \mid} \frac{\partial' g}{\partial t} + \vec{V}_r \cdot \vec{n}_g = 0$$

For a rigid body, the body surface, $g(\vec{r}) = 0$, is not a function of t. Thus, we get

$$\vec{V}_r \cdot \vec{n}_g = 0 \qquad \text{on} \quad g(\vec{r}) = 0 \tag{3.36}$$

where $\vec{n}_g$ is the unit normal vector of the body surface, $g(\vec{r}) = 0$.

(ii) Kutta Condition: Along the edge of separation (e.g., airfoil trailing edge) a form of the Kutta condition must be enforced. For a sharp edge the pressure must be continuous across the edge and hence

$$\Delta C_p \mid_{sp} = 0 \tag{3.37}$$

where the subscript *sp* refers to the edges of separation.

(iii) Infinity Condition: Because the moving frame of reference formulation is used,the velocity at infinity is zero. This condition is given by

$$\nabla \Phi \to 0 \qquad \text{away from} \quad g(\vec{r}) = 0 \tag{3.38}$$

(iv) Wake Condition: For unsteady flows, a wake surface denoted by $w(\vec{r}, t) = 0$, is shed from the edge of separation (e.g., airfoil trailing edge). The wake surface must

satisfy a kinematic boundary condition and a dynamic boundary condition. The kinematic boundary condition has the same form as the no-penetration condition for the body surface and is given by

$$\frac{1}{\mid \nabla w \mid} \frac{\partial' w}{\partial t} + \vec{V}_r \cdot \vec{n}_w = 0 \qquad \text{on} \quad w(\vec{r},t) = 0 \tag{3.39}$$

The dynamic boundary condition requires that the pressure jump across the wake surfaces is zero, or

$$\Delta C_p = C_{pu} - C_{pl} = 0 \qquad \text{on} \quad w(\vec{r},t) = 0 \tag{3.40}$$

where subscripts u and l refer to the upper and lower surface, respectively. The pressure coefficient, C_p, is defined by

$$C_p = \frac{2}{\kappa M_\infty^2}(\rho^\kappa - 1) \tag{3.41}$$

where the non-dimensional density, ρ, is given by Eq. (3.35). Substituting Eq. (3.41) together with Eq. (3.35) into Eq. (3.40) and simplying the results, one obtains

$$\left[\frac{\partial'}{\partial t} + (\nabla \Phi_{av} - \vec{V}_e) \cdot \nabla\right] \Delta\Phi = 0 \qquad \text{on} \quad w(\vec{r},t) = 0 \tag{3.42}$$

where

$$\Delta\Phi = \Phi_u - \Phi_l$$

and

$$\nabla\Phi_{av} = \frac{1}{2}\left[(\nabla\Phi)_u + (\nabla\Phi)_l\right]$$

Eq. (3.42) reproduces the theorems of Kelvin and Helmholtz for the conservation of circulation and outflow of vorticity, respectively. This gives

$$\frac{D\Gamma}{Dt} = \frac{D}{Dt}\int\int \vec{\zeta} \cdot \vec{n}_A dA = 0 \qquad \text{on} \quad w(\vec{r},t) = 0 \tag{3.43}$$

where Γ is the circulation around a wake element and $\vec{\varsigma} \cdot \vec{n}_A$ is the outflow of the vorticity through the area bounded by the curve around which Γ is calculated. For inviscid, homentropic flow, it can be shown [138] that the theorem of the Kelvin is equivalent to

$$\frac{D}{Dt}\left(\frac{\vec{\varsigma}}{\rho}\right) = \left(\frac{\vec{\varsigma}}{\rho}\right) \cdot \nabla \vec{V}_r \tag{3.44}$$

3.2.3 2-D Steady Full-Potential Equation

For two-dimensional steady flows, the time derivative terms and angular velocity, $\vec{\Omega}$, in the above equations are all zero. By using the characteristic parameters of $| \vec{V}_o |$, ρ_∞ and chord length, c, Eqs. (3.34) and (3.35) reduce to

$$\Phi_{xx} + \Phi_{yy} = G \tag{3.45}$$

with

$$G = -\frac{1}{\rho}[(\Phi_x - u_o)\rho_x + (\Phi_y - v_o)\rho_y] \tag{3.46}$$

and

$$\rho = \left\{1 + \frac{\kappa - 1}{2} M_\infty^2 \left[1 - (\Phi_x - u_o)^2 - (\Phi_y - v_o)^2\right]\right\}^{\frac{1}{\kappa - 1}} \tag{3.47}$$

The terms $(\Phi_x - u_o)$ and $(\Phi_y - v_o)$ are the components of relative velocity. For steady flows, the space-fixed frame of reference formulation will yield the same equations if we replace $(\Phi_x - u_o)$ and $(\Phi_y - v_o)$ by Φ_x and Φ_y and let the fluid move at a velocity of $\vec{e}_\infty (\vec{e}_\infty = -\vec{e}_o)$ while the airfoil is kept stationary. This yields

$$\Phi_{xx} + \Phi_{yy} = G \tag{3.48}$$

with

$$G = -\frac{1}{\rho}(\Phi_x \rho_x + \Phi_y \rho_y) \tag{3.49}$$

and

$$\rho = \left[1 + \frac{\kappa - 1}{2} M_\infty^2 \left(1 - \Phi_x^2 - \Phi_y^2\right)\right]^{\frac{1}{\kappa - 1}} \tag{3.50}$$

The boundary conditions for the steady two-dimensional flow can be obtained directly from Eqs. (3.36) to (3.38). Here no wake conditions are needed. These conditions are summarized as follow:

(i) Surface No-Penetration Condition:

$$\nabla\Phi \cdot \vec{n}_g = 0 \qquad \text{on} \quad g(x,y) = 0 \tag{3.51}$$

(ii) Kutta Condition:

$$\Delta C_p \mid_{TE} = 0 \tag{3.52}$$

Equation (3.52) implies that the vortex distribution at the airfoil trailing edge must be zero:

$$\gamma \mid_{TE,u} + \gamma \mid_{TE,l} = 0 \tag{3.53}$$

(iii) Infinity Condition:

$$\nabla\Phi \rightarrow \vec{e}_\infty \qquad \text{away from} \quad g(x,y) = 0 \tag{3.54}$$

where $g(x,y) = 0$ is the airfoil surface and $\vec{n}_g$ is its unit normal vector; TE refers to the trailing edge and the subscripts u and l refer to the upper and lower surface, respectively.

Equations (3.48) through (3.50) are the basic equations to be solved for steady flows in the space-fixed reference. The associated boundary conditions are given by Eqs. (3.51), (3.53) and (3.54).

3.2.4 2-D Unsteady Full-Potential Equation

For the unsteady two-dimensional flow, shown in Fig. 3.2, we have

$$\vec{r}_p = x_p\vec{i} + y_p\vec{j} = x_p\vec{i} + o\vec{j} = x_p\vec{i} \tag{3.55}$$

$$\vec{e}_o = \frac{\vec{V}_o}{\mid \vec{V}_o \mid} = u_o\vec{i} + v_o\vec{j} \tag{3.56}$$

and

$$\vec{\Omega} = o \cdot \vec{i} + o \cdot \vec{j} + \dot{\alpha}\vec{k} = \dot{\alpha}\vec{k} \tag{3.57}$$

where

$$\dot{\alpha} \equiv \frac{d\alpha(t)}{dt} \tag{3.58}$$

As a special case of pitching oscillation, the $\alpha(t)$ is given by Eq. (3.7). Equation (3.34) thus becomes

$$\Phi_{xx} + \Phi_{yy} = G_1 + G_2 \tag{3.59}$$

with

$$G_1 = -\frac{1}{\rho}\{(\Phi_x - u_o + \dot{\alpha}y)\rho_x + [\Phi_y - v_o - \dot{\alpha}(x - x_p)]\rho_y\} \tag{3.60}$$

and

$$G_2 = -\frac{1}{\rho}\frac{\partial' \rho}{\partial t} \tag{3.61}$$

where x_p is the pivot point of the pitching oscillation.

Similarly, Eq. (3.35) reduces to

$$\begin{aligned} \rho = \Big\{1 + \frac{\kappa - 1}{2} M_\infty^2 \Big[& - (\Phi_x - u_o + \dot{\alpha}y)^2 \\ & - (\Phi_y - v_o - \dot{\alpha}(x - x_p))^2 + (u_o - \dot{\alpha}y)^2 \\ & + (v_o + \dot{\alpha}(x - x_p))^2 - 2\left(\frac{\partial' \Phi}{\partial t}\right) \Big] \Big\}^{\frac{1}{\kappa - 1}} \end{aligned} \tag{3.62}$$

Equations (3.59) through (3.62) are the basic equations to be solved for two-dimensional unsteady flows in the moving frame of reference. The boundary conditions are derived directly from those in Subsection 3.2.2. They are presented here.

(i) Surface No-Penetration Condition:

$$\vec{V}_r \cdot \vec{n}_g = 0 \qquad \text{on} \quad g(x, y) = 0 \tag{3.63}$$

note that here $\vec{V}_r$ is the relative velocity.

(ii) Kutta Condition:

$$\Delta C_p \mid_{TE} = 0 \tag{3.64}$$

This also implies that

$$\frac{D}{Dt}\left(\frac{\varsigma}{\rho}\right) \mid_{TE} = 0 \tag{3.65}$$

or

$$\frac{\partial'}{\partial t}\left(\frac{\varsigma}{\rho}\right) \mid_{TE} + \vec{V}_r \cdot \nabla \left(\frac{\varsigma}{\rho}\right) \mid_{TE} = 0 \tag{3.66}$$

Note that Eq. (3.65) is a special case of Eq. (3.44) for two-dimemsional flows.

(iii) Infinity Condition:

$$\nabla \Phi \rightarrow 0 \qquad \text{away from} \quad g(x,y) = 0 \tag{3.67}$$

(iv) Wake Conditions: The kinematic boundary condition is given by

$$\frac{1}{(\nabla w)} \frac{\partial' w}{\partial t} + \vec{V}_r \cdot \vec{n}_w = 0 \qquad \text{on} \quad w(x,y,t) = 0 \tag{3.68}$$

and the dynamic boundary condition is given by

$$\frac{D}{Dt}\left(\frac{\varsigma}{\rho}\right)_w = 0 \tag{3.69}$$

or

$$\frac{\partial'}{\partial t}\left(\frac{\varsigma}{\rho}\right)_w + \vec{V}_r \cdot \nabla \left(\frac{\varsigma}{\rho}\right)_w = 0 \tag{3.70}$$

where the subscript $w(x,y,t) = 0$ is the wake surface shed from the trailing edge.

3.3 IE Solutions of FP Equations

Before the integral equation solution of the full-potential equation is presented, it is necessary to describe briefly the standard panel method for incompressible potential flows and its recent extension to transonic flows.

3.3.1 Panel Methods or Incompressible IE Methods

The standard panel method for incompressible potential flows around a complex configuration can be described briefly as follows:

Since the governing equation for this flow is Laplace's equation, the IE solution for the perturbation velocity field consists of the sum of two surface integral terms: a source term and a doublet or vortex term. Therefore, the body sufaces are divided into a finite number of small elements with each element geometry approximated by an *nth* order panel. A distributed or concentrated singularity is placed on each panel. The strength of singularities on the panels are determined by satisfing the boundary conditions at certain points on the panel surfaces (so-called control points). Once the strength of the singularities is known, the IE for the velocity field is used and the pressure at the body surface or at any field point can be calculated easily. The perturbation velocity at any point is the sum of the contributions from all body-surface singularities. Therefore, the solution of a flow problem around complex configurations reduces to a solution for the strength of a set of surface singularities by satisfying body-surface boundary conditions. This yields a set of linear algebraic equations, which can be solved by any standard method. The surface singularities can be divided into three types: (i) source/sink, (ii) vortex and/or, (iii) doublet. Different combinations of these three types of singularities can be made according to the flow conditions and body configurations. Details on standard panel methods for incompressible flows can be found in many references, such as Kraus [139].

For subsonic flows, a linearized governing equation can be obtained by assuming small disturbances. The solution for subsonic small disturbance flows can be obtained by standard panel methods described above in which compressibility effects are taken into account through the Prandtl-Glauert transformation. Also, the standard panel methods can be applied to linearized supersonic flows.

But for transonic flows, there is no such linearized governing equation. The compressibility effects must be maintained as nonlinear term(s) in the governing

equation. Recently, several IE schemes which are based on standard panel methods have been developed for transonic flows, as mentioned in Chapter 2. The schemes are called field panel methods. In the IE solution for transonic flows, volume integral terms contributed from the nonlinear compressibilities are added to the standard surface integral terms of singularities for velocity calculations. The details of this method will be discussed in Chapters 4 and 5.

3.3.2 IE Solution for Steady Transonic Flows

Equation (3.48) is the full-potential equation in which G is representing the total compressibility. This G-term could be split into a linear and a nonlinear term with the linear term given by $\Phi_{xx}M_\infty^2$. Instead, reading Eq. (3.48) as Poisson's equation and by using Green's third identity, the integral equation solution of Eq. (3.48) in terms of the velocity field for a steady two-dimensional flow in a space-fixed frame of reference is given by

$$\begin{aligned}\nabla\Phi(x,y) = \vec{e}_\infty &+ \frac{1}{2\pi}\oint_g q_g(s)\frac{(x-\xi)\vec{i}+(y-\eta)\vec{j}}{(x-\xi)^2+(y-\eta)^2}ds \\ &+ \frac{1}{2\pi}\oint_g \gamma_g(s)\frac{(y-\eta)\vec{i}-(x-\xi)\vec{j}}{(x-\xi)^2+(y-\eta)^2}ds \\ &+ \frac{1}{2\pi}\int\int G(\xi,\eta)\frac{(x-\xi)\vec{i}+(y-\eta)\vec{j}}{(x-\xi)^2+(y-\eta)^2}d\xi d\eta \\ &+ \frac{1}{2\pi}\int_S q_S(s)\frac{(x-\xi)\vec{i}+(y-\eta)\vec{j}}{(x-\xi)^2+(y-\eta)^2}ds\end{aligned} \tag{3.71}$$

where the subscript g refers to the airfoil surface and the subscript S refers to the shock surface; q and γ are surface source and vortex distributions, respectively; ds is the infinitesimal line element measured in (ξ,η) coordinates. Here the source and vortex singularities are used in the present research work. It should be noted here that the G-term is considered as an inhomogeniety in stead of a nonlinearity.

In Eq. (3.71), the first integral is the contribution of the body thickness; the second integral is the contribution of lift or thickness or both; the third integral is

a field integral term representing the contribution due to the full compressibility; while the last integral is the explicit contribution due to the shock for the shock-fitting solution, which will be discussed detail in Sec. 4.2.2.

Not all of the terms in the first and second integral in Eq. (3.71) are necessarily included in the calculation of the velocity field. For symmetric flows, either the first integral or second integral can be used; while for asymmetric flows, either the second integral or both integrals should be used.

It should be noticed that the integrand of the volume integral of Eq. (3.71) decreases rapidly with increasing distance not only because of the factor of $1/[(x-\xi)^2+(y-\eta)^2]$ but also because G(x,y) diminishes rapidly with increasing distance. Consequently, for computational purposes, the volume integral term needs to be addressed only within the immediate vicinity of the body.

It should also be noticed that the present formulation differs from the formulations given by Sinclair [63] and by Tseng and Morino [118]. The present formulation is based on the velocity field in which the field source term G(x,y) contains first order derivatives of the density only, and the normal velocity is discontinuous across the shock. Both formulations of Sinclair [63] and Tseng and Morino [118] are based on the velocity potential in which the source term G contains first- and second-order derivatives of the velocity potential and the velocity potential is continuous across the shock. The present formulation has two advantages over the velocity-potential formulation: (1) only first order derivatives need to be calculated by finite-difference, and (2) It does not need the calculation of derivatives of the velocity potential in order to detect the shock formation since the velocity field is calculated directly in the present formulation.

3.3.3 IE Solution for Unsteady Transonic Flows

The unsteady full-potential equation in the moving frame of reference oxy is given by Eq. (3.59), which is a Poisson's equation also. By using the Green's third identity, similar to that for steady flows, the integral equation solution of Eq. (3.59), for the absolute velocity field in the moving frame of reference, is given by

$$\begin{aligned}
\nabla\Phi(x,y,t) = & \frac{1}{2\pi}\oint_g q_g(s,t)\frac{(x-\xi)\vec{i}+(y-\eta)\vec{j}}{(x-\xi)^2+(y-\eta)^2}ds \\
& + \frac{1}{2\pi}\oint_g \gamma_g(s,t)\frac{(y-\eta)\vec{i}-(x-\xi)\vec{j}}{(x-\xi)^2+(y-\eta)^2}ds \\
& + \frac{1}{2\pi}\int\int G_1(\xi,\eta,t)\frac{(x-\xi)\vec{i}+(y-\eta)\vec{j}}{(x-\xi)^2+(y-\eta)^2}d\xi d\eta \\
& + \frac{1}{2\pi}\int\int G_2(\xi,\eta,t)\frac{(x-\xi)\vec{i}+(y-\eta)\vec{j}}{(x-\xi)^2+(y-\eta)^2}d\xi d\eta \\
& + \frac{1}{2\pi}\int_w \gamma_w(s,t)\frac{(y-\eta)\vec{i}-(x-\xi)\vec{j}}{(x-\xi)^2+(y-\eta)^2}ds \\
& + \frac{1}{2\pi}\int_S q_S(s,t)\frac{(x-\xi)\vec{i}+(y-\eta)\vec{j}}{(x-\xi)^2+(y-\eta)^2}ds
\end{aligned} \tag{3.72}$$

The first two integrals in Eq. (3.72) are similar to those of Eq. (3.71) for steady flows, with the exception of their implicit dependence on time t. The third integral is the contribution of compressibility similar to that of Eq. (3.71), while the fourth integral is the explicit contribution due to the unsteadiness. The fifth integral represents the contribution of the wake surface shed at the airfoil trailing edge. The last integral term represents the explicit contribution of the shock panel and must not be considered in the field integral terms for the shock-fitting solution. It should be noted that the term $\vec{e}_\infty$, which appeared in Eq. (3.71) for steady flows, does not appear here, because the moving frame of reference is used since the infinity boundary condition is zero.

3.4 Unsteady Euler Equations

As discussed earlier, for transonic flows with strong shocks, the full-potential equation with the isentropic flow assumption is no longer applicable. For these cases, Euler equations are solved in a small embedded domain around the shock. The dimensionless conservation form of the Euler equations in two-dimensional flows is given by

$$\frac{\partial \vec{q}}{\partial t} + \frac{\partial \vec{E}}{\partial x} + \frac{\partial \vec{F}}{\partial y} = 0 \tag{3.73}$$

where the flow vector field $\vec{q}$, and the inviscid fluxes $\vec{E}$ and $\vec{F}$ are given by

$$\begin{aligned} \vec{q} &= [\rho, \rho u, \rho v, \rho e_t]^t \\ \vec{E} &= [\rho u, \rho u^2 + p, \rho uv, \rho u h_t]^t \\ \vec{F} &= [\rho v, \rho uv, \rho v^2 + p, \rho v h_t]^t \end{aligned} \tag{3.74}$$

In Eq. (3.74), the density is ρ, the velocity components are u and v; the pressure is p and the total energy and total enthalpy per unit mass are given by

$$e_t = \frac{p}{\rho(\kappa + 1)} + \frac{1}{2}(u^2 + v^2) \tag{3.75}$$

and

$$h_t = e_t + \frac{p}{\rho}, \tag{3.76}$$

respectively.

For steady flows, the energy equation, the last component of Eq. (3.74), reduces to a statement of constant-total enthalphy, which gives

$$p = \frac{\rho}{\kappa}\left[\frac{1}{M_\infty^2} + \frac{(\kappa + 1)}{2}(1 - u^2 - v^2)\right] \tag{3.77}$$

The no-penetration condition is enforced on the airfoil surface through the normal-momentum equation. The normal-momentum equation is given by

$$\frac{\partial p}{\partial n} = \rho \vec{V} \cdot (\vec{V} \cdot \nabla \hat{n}) \tag{3.78}$$

where $\hat{n}$ is the unit normal to the airfoil surface. The other boundary conditions at the upstream boundary and the top boundary and initial conditions are obtained from the integral equation solutions. The downstream boundary conditions initially are obtained from the integral equation solutions. In the subsequent time steps, they are extrapolated from the interior cells similar to the outflow treatment of a subsonic boundary.

3.5 Validity of IEM for Transonics

Panel methods for linearized aerodynamics (incompresssible, subsonic and supersonic flows) have been very well developed. The methods are well accepted in the linear aerodynamics community. But the IE methods for nonlinear transonic flows are new ones started only a few years ago.

Questions about the validity of the mathematical foundations of transonic IE methods may often be asked. People may question the validity of using the integral equation solution, which is based on linear elliptic operators, to solve nonlinear mixed-type differential equations as those of transonic flows. The best answer to this question is the successful solutions of newly developed transonic integral equation methods [54, 58-64, 116-119]. In these methods, a volume integral term, corresponding to the nonlinear term that is considered as an inhomogeneous term, is added in the integral solution to account for the full contribution of compressibility. The type-differencing or the artificial density concept is used to model computationally the proper wave propapation implied by the mixed nature of the equation. They are at the root of extending the classical IE methods to transonic flow problems. For more discussion on the validily of the method, one can refer to the paper by Tseng and Morino [118].

Chapter 4

COMPUTATIONAL SCHEMES OF STEADY TRANSONIC FLOWS

The computational schemes for solving steady transonic flows are presented in this chapter. In the first section, we present the scheme of integral equation method for shock-free flows. In the second section, the IE with Shock-Capturing (IE-SC) and the IE with Shock-Capturing Shock-Fitting (IE-SCSF) schemes of the integral equation solution for the transonic flows are described. The Integral Equation with Embedded Euler Domain (IE-EE) scheme for the solution of transonic flows with strong shocks is presented in the third section.

4.1 IE Scheme for Shock-Free Flows

4.1.1 Discretization of the Equations, No-Penetration Condition

Equation (3.71) is the integral equation solution for the velocity field of the steady full-potential equation. The first two integral terms are the standard panel method terms, which account for the contributions of the airfoil thickness, camber and angle of attack. These two integrals are evaluated along the airfoil surface. The airfoil surface is divided into a number of flat panels and a source and/or vortex distribution is placed on each panel as shown in Fig. 4.1. The finer panels are used in the leading edge and in the region around the shock for transonic flows. To enforce the no-penetration condition at the airfoil surface, one control point on each panel must be used as shown in Fig. 4.1, where the condition is satisfied.

The third integral term is a field integral term, which represents the contribution of the full compressibility, G(x,y). The computational domain for this field integral term is constructed around the airfoil within a small limited region. The domain is divided into a number of rectangular elements with the exception of the airfoil surface where trapezoidal elements are used. The computational domain for this integral term is shown in Fig. 4.2. For shock-free flows, the last integral term is set to zero. It will be considered only for the shock-fitting scheme.

The discretized equation becomes

$$\begin{aligned}\nabla\Phi(x,y) \equiv \vec{V} &\equiv u\vec{i} + v\vec{j} \\ &= \vec{e}_\infty + \frac{1}{2\pi}\sum_{k=1}^{N}\int_{g_k} q_{g,k}(s)\frac{(x-\xi)\vec{i}+(y-\eta)\vec{j}}{(x-\xi)^2+(y-\eta)^2}ds \\ &+ \frac{1}{2\pi}\sum_{k=1}^{N}\int_{g_k} \gamma_{g,k}(s)\frac{(y-\eta)\vec{i}-(x-\xi)\vec{j}}{(x-\xi)^2+(y-\eta)^2}ds \\ &+ \frac{1}{2\pi}\sum_{i}^{IM}\sum_{j}^{JM}\int\int_{A_{i,j}} G_{i,j}\frac{(x-\xi)\vec{i}+(y-\eta)\vec{j}}{(x-\xi)^2+(y-\eta)^2}d\xi d\eta\end{aligned} \tag{4.1}$$

where N is the total number of airfoil surface panels and $IM \times JM$ is the total number of field elements. The indices, k and (i,j), refer to the surface panel and field-element numbers, respectively, while the subscript g refers to the airfoil surface.

The summations of the above integrals in Eq. (4.1) are taken over all airfoil-surface panels and all field elements. These surface panels and field elements are thus called "senders", while the surface panels and field-elements, where the velocities are computed at their control points, are called "receivers". Therefore, Eq. (4.1) clearly states that the velocity at the receiver (x,y), $\nabla\Phi(x,y)$, is contributed from all sources at senders plus the contribution of the free-stream velocity.

For high accuracy, local linear distributions of source and vortex singularities are used in the present research work. These distributions are expressed in terms of the local nodal values as given by

$$q_{g,k}(\xi) = \left(\frac{\xi_{k+1} - \xi}{\xi_{k+1} - \xi_k}\right) q_{g,k} + \left(\frac{\xi - \xi_k}{\xi_{k+1} - \xi_k}\right) q_{g,k+1} \tag{4.2a}$$

and

$$\gamma_{g,k}(\xi) = \left(\frac{\xi_{k+1} - \xi}{\xi_{k+1} - \xi_k}\right) \gamma_{g,k} + \left(\frac{\xi - \xi_k}{\xi_{k+1} - \xi_k}\right) \gamma_{g,k+1}, \tag{4.2b}$$
$$\xi_k \leq \xi \leq \xi_{k+1}, k = 1, 2, 3, ...N.$$

where ξ is the local coordinate as shown in Fig. 4.3; $q_{g,k}, q_{g,k+1}$ and $\gamma_{g,k}, \gamma_{g,k+1}$ are paris of unknown nodal values for each panel source and vortex distributions, respectively. Thus, the distributions of the source and vortex singularities are continuous but not smooth between adjacent panels. Therefore, there are N+1 unknown nodal values for the source and/or vortex distributions for N panels.

Substituting Eqs. (4.2a) and (4.2b) into Eq. (4.1) and evaluating the integral in local coordinates, a closed form expression of the solutions is obtained as given in Appendix A. The resulting expressions are then transformed from the local coordinates (ξ, η) to the global coordinates (x,y).

Due to the fact that the computation of the third integral term of Eq. (4.1) is expensive, a constant G distribution is assumed over each small field element. This integral is evaluated in the global coordinates over each field element. The resulting closed form expression for typical elements is given in Appendix B.

Applying the no-penetration condition, Eq. (3.51), at each control point, we obtain a set of linear algebraic equations. For example, if we want to solve for γ_g, then we get a set of N linear algebraic equations for N control points of the form

$$[A_{i,j}]\{\gamma_{g,i}\} = \{B_i\} \tag{4.3}$$

where $\{\gamma_{g,i}\}$ is the matrix of unknown nodal values of vorticity, and $\{B_i\}$ is the known right-hand side vector which is the contributions from compressibility and

free-stream velocity. The coefficient matrix $[A_{i,j}]$ is known as the "Influence Coefficient Matrix".

4.1.2 Computational Scheme for Shock-Free Flows

The main difference between the standard panel scheme and the transonic integral equation scheme is due to the field integral term of Eq. (4.1). This term is a nonlinear term and therefore unlike the standard panel schemes, the solution cannot be obtained directly and an iterative procedure is necessary.

In this research work, we examine both the source panel and vortex panel modeling. For simplicity, we first describe the computational scheme for shock-free flows with the full-compressibility term, G, included. The procedure is the base of the IE-SC scheme.

The computational scheme is sketched in Fig. 4.4 and it is described as follows:

Step 1 - Standard Panel Scheme for the Linear Problem:

Setting $G(x,y) = 0$, a standard panel method scheme is employed to get q_g or γ_g or both. By applying the no-penetration condition, Eq. (3.51), at each control point of the airfoil surface panels, one gets a set of N equations with N+1 unknown nodal values as given by Eq. (4.3). There is at least one additional equation needed to solve for the N+1 unknowns. If a source panel modeling is used, one can use the condition of zero total source, because the airfoil is a closed body. This condition gives

$$\sum_{k=1}^{N} \int_{\xi_k}^{\xi_{k+1}} q_{g,k}(\xi) d\xi = 0 \tag{4.4}$$

If a vortex panel modeling is used, one can apply the Kutta condition, Eq. (3.53), at the trailing edge. This yields one additional equation which is given by

$$\gamma\,|_{TE,u} + \gamma\,|_{TE,l} = 0 \tag{4.5}$$

Equation (4.3) together with Eq. (4.4) or Eq. (4.5) form a set of N+1 linear algebraic equations for N+1 unknown nodal values. This set is solved by any standard method to obtain N+1 nodal values of the source or vortex distributions.

Stet 2 - Computation of the Initial Values of G:

The initial values of the compressibility, $G(x,y)$, are calculated by using the linear (Prandtl-Glauert) compressibility

$$G(x,y) = M_\infty^2 u_x(x,y) \tag{4.6}$$

Here, the x-component of the field velocity, $u(x,y)$, is obtain from the x-component of Eq. (4.1) without the compressibility term, and q_g or γ_g is obtained in Step 1. The derivatives of $u(x,y)$ with respect to x, u_x, is obtained analytically.

Step 3 - Enforcing the Boundary Conditions:

With the compressibility, G(x,y), obtained in Step 2 and the source or vortex distribution obtained in Step 1, Eq. (4.1) is used to satisfy the airfoil-surface no-penetration condition, Eq. (3.51), to get a set of N-equations for N+1 unknown nodal values of the q_g or γ_g distributions, as given by Eq. (4.3). By solving Eq. (4.3) together with Eq. (4.4) or Eq. (4.5), the N+1 new nodal values of q_g or γ_g are obtained.

Step 4 - Calculation of the Surface Pressure Coefficient:

Once we obtain G and q_g or γ_g distributions, we use Eq. (4.1) to calculate the velocity at each control point. Next, we calculate the surface pressure coefficient. The pressure coefficient is defined by

$$C_p \equiv \frac{2}{\kappa M_\infty^2}\left(\frac{p}{p_\infty} - 1\right) \tag{4.7}$$

where p and p_∞ are all dimensional quantities. By introducing the isentropic flow relation,

$$\frac{p}{p_\infty} = \left(\frac{\rho}{\rho_\infty}\right)^\kappa \tag{4.8}$$

and writing $(\frac{\rho}{\rho_\infty})$ as the dimensionless density, ρ, Eq. (4.7) becomes

$$C_p = \frac{2}{\kappa M_\infty^2}(\rho^\kappa - 1) \tag{4.9}$$

Substituting Eq. (3.50) into Eq. (4.9), we get

$$C_p = \frac{2}{\kappa M_\infty^2}\left\{\left[1 + \frac{\kappa - 1}{2}M_\infty^2(1 - {\Phi_x}^2 - {\Phi_y}^2)\right]^{\frac{\kappa}{\kappa-1}} - 1\right\} \tag{4.10}$$

Equation (4.10) is used to calculate the pressure coefficients at each of the airfoil-surface control points.

Step 5 - Calculation of the Full-Compressibility:

In this step, we first compute the velocity field, $\nabla\Phi(x,y)$, by using Eq. (4.1). The source/vortex distribution, q_g/γ_g, over each airfoil-surface panel and the compressibility, G(x,y), over each field-element are already obtained in previous steps. Substituting the newly obtained q_g/γ_g and G(x,y) into Eq. (4.1) and evaluating the integrals, one obtains the velocity fields, $\nabla\Phi(x,y)$, at each field point (centroid of a field-element). Then Eq. (3.50) is used to compute the density, $\rho(x,y)$, and Eq. (3.49) is used to compute the compressibility, G(x,y), at each field point, where central-differencing is used to compute the derivatives of the densities for subsonic (shock-free) flows.

Step 6 - Enforcing the Boundary Conditions:

With the newly obtained compressibility, we use Eq. (4.1) to satisfy the no-penetration condition, Eq. (3.51), over each airfoil-surface control point. Thus a set of N-linear algebraic equations given by Eq. (4.3) is obtained. By solving Eq. (4.3) with Eq. (4.4) or Eq. (4.5), we get the new N+1 nodal values of source/vortex.

Step 7 - Calculation of the Surface Pressure Coefficient:

Eq. (4.1) is used to calculate the velocities at each control point and then Eq. (4.10) is used to calculate C_p there.

Step 8 - Convergence Criterion:

Steps 5-7 are repeated until the C_p converges at each control point.

Since the computation of the field integral term in Eq. (4.1) is expensive, because of the constant G-distribution assumption over each field element, we restrict the computation of the integral form using a constant G-distribution to the near field computations. For the far field computations, this integral term is replaced by an equivalent lumped source term at its centroid. As given by the third integral of Eq. (4.1), we represent the velocity at point (x, y) due to the constant G-distribution at the element of centroid of (ξ, η) by using the integral

$$\vec{V}(x, y; \xi, \eta) = \frac{1}{2\pi} G_{i,j} \int\int_{A_{i,j}} \frac{(x-\xi)\vec{i} + (y-\eta)\vec{j}}{(x-\xi)^2 + (y-\eta)^2} d\xi d\eta \tag{4.11}$$

Since the distance between the receiver (x,y) and the sender (ξ, η), d_{sr}, is given by

$$d_{sr} = [(x-\xi)^2 + (y-\eta)^2]^{\frac{1}{2}} \tag{4.12}$$

we compare the value of d_{sr} with a specified near field distance, d_{near}, and if $d_{sr} > d_{near}$ Eq. (4.11) is replaced by the equivalent lumped formula, which is given

by

$$\vec{V}(x,y;\xi,\eta) = \frac{1}{2\pi} G_{i,j} \frac{(x-\xi)\vec{i} + (y-\eta)\vec{j}}{d^2_{sr}} A_{i,j} \tag{4.13}$$

where (x,y) is the centroid of the receiver and (ξ,η) is the centroid of the sender. With sufficient accuracy, it has been determined computationally that the near field distance can be as small as

$$d_{near} = 0.05 \quad \text{chord length} \tag{4.14}$$

The concept of the far-field lumped calculation is shown in Fig. 4.5.

4.2 IE-SC and IE-SCSF Schemes for Transonic Flows

The IE with Shock-Capturing (IE-SC) and IE with Shock-Capturing-Shock-Fitting (IE-SCSF) schemes are developed to treat transonic flows with shocks. The IE-SC scheme is a natural extension of the IE scheme for shock-free flows presented in the previous section. The IE-SCSF scheme consists of two parts: a Shock-Capturing (SC) part and a Shock-Fitting (SF) part. The steps of the IE-SCSF scheme is shown in Fig. 4.6. These two schemes are described in the following two sub-sections.

4.2.1 IE-SC Scheme

The IE-SC scheme is similar to that for shock-free flows described in Subsection 4.1.2, with the exception that the Murman-Cole type difference is used to compute the derivatives of the densities during Step 5 of the scheme. Now let's explain the type differencing used in the current IE-SC scheme.

Once the velocity and the density fields are computed at each field point during Step 5, the local Mach number is computed to determine the type of field point; supersonic or subsonic points. The local Mach number, $M(x,y)$, is calculated by

$$M(x,y) = M_\infty \mid \nabla\Phi(x,y) \mid / \rho(x,y)^{\frac{\kappa-1}{2}} \tag{4.15}$$

For subsonic points where $M < 1$, central-differencing is used to calculate the derivatives of the densities with respect to x and y. They are given by

$$\left(\frac{\partial \rho}{\partial x}\right)_{i,j} = \frac{\rho_{i+1,j} - \rho_{i-1,j}}{x_{i+1,j} - x_{i-1,j}}, \qquad \text{for} \quad M < 1 \tag{4.16a}$$

and

$$\left(\frac{\partial \rho}{\partial y}\right)_{i,j} = \frac{\rho_{i,j+1} - \rho_{i,j-1}}{y_{i,j+1} - y_{i,j-1}}, \qquad \text{for} \quad M < 1 \tag{4.16b}$$

For supersonic points where $M > 1$, backward-differencing is used. They are given by

$$\left(\frac{\partial \rho}{\partial x}\right)_{i,j} = \frac{\rho_{i,j} - \rho_{i-1,j}}{x_{i,j} - x_{i-1,j}}, \qquad \text{for} \quad M > 1 \tag{4.17a}$$

and

$$\left(\frac{\partial \rho}{\partial y}\right)_{i,j} = \frac{\rho_{i,j} - \rho_{i,j-1}}{y_{i,j} - y_{i,j-1}}, \qquad \text{for} \quad M > 1 \tag{4.17b}$$

where the subscripts, i and j, represent the centroid of the element where the derivative is computed as shown in Fig. 4.7. This type-differencing is the so-called Murman-Cole type-difference scheme.

The type-differencing given by Eqs. (4.16a) through (4.17b) is consistant with the mixed nature of the transonic flow, because the local disturbance in a subsonic flow propagates in all directions while in a supersonic flow the local disturbance is confined to the downstream Mach wedge of the disturbance. Also it should be noted that the type-differencing is used both in x and y directions, because the full-potential equation formulation (rather than TSD formulation) is used.

One exception is that forward-differencing is used to compute the derivatives of the densities at the first elements after the shock discontinuity. The forward-differencing formula is given by

$$\left(\frac{\partial \rho}{\partial x}\right)_{i,j} = \frac{\rho_{i+1,j} - \rho_{i,j}}{x_{i+1,j} - x_{i,j}} \tag{4.18a}$$

and

$$\left(\frac{\partial \rho}{\partial y}\right)_{i,j} = \frac{\rho_{i,j+1} - \rho_{i,j}}{y_{i,j+1} - y_{i,j}} \tag{4.18b}$$

4.2.2 IE-SCSF Scheme

The IE-SCSF scheme is an extension of the IE-SC scheme by introducing shock panels at the captured shock. In this scheme, the iterative cycle of the shock-capturing (SC) part described above is carried out until the location of the shock is fixed. Then, the shock-fitting (SF) part is initiated by introducing shock panels at the captured shock.

The iterative cycle of the SF part is described below:

Step 1 - Introducing Shock Panels:

With the values of the local Mach number at each field point obtained in the previous step, we can find the approximate location of the shock wave, where the local Mach number changes from a value greater than 1 to a value smaller than 1. Furthermore, we use the relation between the slope of the oblique shock and the relative direction of the velocities ahead and behind the shock to generate the shock panels one by one. This relation is given by

$$\beta = \sin^{-1}\left[\frac{(\kappa+1)\sin\beta\sin\theta}{2\cos(\beta-\theta)} + \frac{1}{M_1^2}\right]^{\frac{1}{2}} \tag{4.19}$$

where β is the shock-panel angle and θ is the direction of the flow behind the shock relative to that ahead of the shock as shown in Fig. 4.8.

We start with the first layer of the field-elements above or below the airfoil and place a vertical shock panel at a location where M changes from a value greater than 1 to a value smaller than 1. Then we compute the velocity vectors at the elements ahead and behind the shock for the next layer to obtain the relative direction of

these two velocity vectors, θ. Using θ and M_1 in Eq. (4.19) the shock angle, β, is computed for this layer. The second shock panel is thus generated according to the value of β just obtained and the fact that shock panels form continuous surfaces. This procedure is repeated until M_1 is smaller than 1, where it is stopped.

The field element with the shock panel inside is then split into three parts as shown in Fig. 4.8, where the original rectangular element is split into two trapezoidal sub-field elements plus one panel representing a shock panel.

The constant distribution of strength for each shock panel is given by

$$q_s = -(V_{1n} - V_{2n}) = -\frac{2V_{1n}}{\kappa+1}\left(1 - \frac{1}{M_{1n}^2}\right), \qquad M_{1n} > 1 \tag{4.20}$$

where subscripts 1 and 2 refer to conditions ahead and behind the shock, respectively, while the subscript n refers to the normal component with respect to the shock.

After introducing shock panels, the integral equation solution, Eq. (4.1), becomes

$$\begin{aligned}
\nabla\Phi(x,y) = \vec{e}_\infty &+ \frac{1}{2\pi}\sum_{k=1}^{N}\oint_{g_k} q_{g,k}(s)\frac{(x-\xi)\vec{i}+(y-\eta)\vec{j}}{(x-\xi)^2+(y-\eta)^2}ds \\
&+ \frac{1}{2\pi}\sum_{k=1}^{N}\oint_{g_k} \gamma_{g,k}(s)\frac{(y-\eta)\vec{i}-(x-\xi)\vec{j}}{(x-\xi)^2+(y-\eta)^2}ds \\
&+ \frac{1}{2\pi}\sum_{i}^{IM}\sum_{j}^{JM} G_{i,j}\int\int_{A_{i,j}}\frac{(x-\xi)\vec{i}+(y-\eta)\vec{j}}{(x-\xi)^2+(y-\eta)^2}d\xi d\eta \\
&+ \frac{1}{2\pi}\sum_{k}^{NS} q_{S,k}\int_{S_k}\frac{(x-\xi)\vec{i}+(y-\eta)\vec{j}}{(x-\xi)^2+(y-\eta)^2}ds
\end{aligned} \tag{4.21}$$

where the index NS refers to the total number of shock panels and the last integral term is the explicit contribution of the shock panels, which is extracted from the third field integral term. It should be mentioned that mathematically the third field integral term includes all compressibility effects including shock discontinuity. Since

a relatively coarse grid has been used in our computational domain, the contribution of the shock discontinuity is extracted from the third field integral term, for those field-elements which include shock surface, and is used explicitly. By doing this, the shock discontinuity is sharpened. Also we should note that the strength of the shock panels is calculated by Eq. (4.20), which states that the strength is equal to the jump of the normal velocity across the shock panel. Therefore, if a shock panel is placed at a location where the normal velocity jump vanishes, then the shock-panel strength will be automatically zero and thus this integral term will vanish.

Step 2 - Calculation of the Flow Properties:

After the shock panels are introduced, Eq. (4.21) is used to compute the velocity field, where the contributions from the two split trapezoidal elements are computed by using the third integral term in Eq. (4.21). The contribution of the shock panel is computed by using the fourth integral term in Eq. (4.21). Equation (3.50) is then used to compute the density.

Step 3 - R-H Relations Across the Shock:

In this step, the Rankine-Hugoniot relations are used to cross the shock. The velocities and the densities at the first elements behind the shock panels are updated by

$$\begin{aligned} V_{2n} &= \frac{(\kappa-1)M_{1n}^2+2}{(\kappa+1)M_{1n}^2}V_{1n} \\ V_{2t} &= V_{1t} \\ \rho_2 &= \frac{(\kappa+1)M_{1n}^2}{(\kappa-1)M_{1n}^2+2}\rho_1 \end{aligned} \tag{4.22}$$

Step 4 - Computation of the Full-Compressibility:

Now we calculate the derivatives of the densities by using the type-differencing described above, and then Eq. (3.49) is used to compute the full-compressibility function, $G(x, y)$.

Step 5 - Enforcing the Boundary Conditions:

Equation (4.21) is used to satisfy the non-penetration condition at each control point of the airfoil surface panel. We then solve the resulting equations given by Eq. (4.3) together with Eq. (4.4) or (4.5) to obtain the N+1 new nodal values of the source/vortex distributions.

Step 6 - Computation of the Surface Pressure Coefficients:

Equation (4.10) is applied to compute the airfoil surface pressure coefficient at each control point.

Step 7 - Convergence Criterion:

If the surface pressure coefficient at each control point does not converge, Steps 1-6 are repeated.

4.3 IE-EE Scheme for Transonic Flows with Strong Shocks

In order to obtain accurate and unique solutions to the transonic flow problem with strong shocks, the Euler equations are solved in a small embedded domain around the shock in the integral equation computational region. Because it is desired that the method be applicable to complex geometric configurations, the finite-volume method is used to develop the space discretization, allowing the use of an arbitrary grid.

The basic finite-volume equation is obtained by integrating the Euler equations, Eq. (3.73), over x and y and applying the divergence theorem to the flux terms

$$\int\int \frac{\partial q}{\partial t} dA + \oint (E dy + F dx) = 0 \tag{4.23}$$

Equation (4.23) is applied to each quadrilateral cell of the embedded domain. The resulting difference equation is given by

$$\left(\frac{\partial q}{\partial t}\right)_{i,j} \Delta A_{i,j} + \sum_{r=1}^{4} (E\Delta y_r + F\Delta x_r) = 0 \tag{4.24}$$

where $\Delta A_{i,j}$ is cell area; r refers to the cell-side number and the integer subcript refers to the centroidal value.

Second- and fourth-order dissipation terms, $D(q)$, as proposed by Jameson, et al. [48], are added to the right-hand side of Eq. (4.24) with artificial viscosity coefficients $\nu^{(2)}$ and $\nu^{(4)}$. Thus, Eq. (4.24) becomes

$$\left(\frac{\partial q}{\partial t}\right)_{i,j} \Delta A_{i,j} + \sum_{r=1}^{4} (E\Delta y_r + F\Delta x_r) = D(q) \tag{4.25}$$

where

$$D(q) = D_x(q) + D_y(q) \tag{4.26}$$

and

$$D_x(q) = d_{i+1/2,j} - d_{i-1/2,j} \tag{4.27a}$$

$$D_y(q) = d_{i,j+1/2} - d_{i,j-1/2} \tag{4.27b}$$

and a typical $d_{i+1/2,j}$ is given by

$$\begin{aligned} d_{i+1/2,j} = \frac{\Delta A_{i+1/2,j}}{\Delta t} [&\nu^{(2)}_{i+1/2,j}(q_{i+1,j} - q_{i,j}) \\ &- \nu^{(4)}_{i+1/2,j}(q_{i+2,j} - 3q_{i+1,j} + 3q_{i,j} - q_{i-1,j})] \end{aligned} \tag{4.28}$$

where

$$\begin{aligned} \nu^{(2)}_{i+1/2,j} &= \epsilon_2 max(\lambda_{i+1,j}, \lambda_{i,j}) \\ \nu^{(4)}_{i+1/2,j} &= max[0, (\epsilon_4 - \nu^{(2)}_{i+1/2,j})] \end{aligned} \tag{4.29}$$

and

$$\lambda_{i,j} = \frac{|p_{i+1,j} - 2p_{i,j} + p_{i-1,j}|}{|p_{i+1,j}| + 2|p_{i,j}| + |p_{i-1,j}|} \tag{4.30}$$

Equations (4.29) and (4.30) show that the artificial viscosity coefficients $\nu^{(2)}$ and $\nu^{(4)}$ adapt to the local pressure gradient. The $\nu^{(2)}$-coefficient varies from a maximum value in regions of high pressure gradients (shock regions) to a minimum value in regions of low pressure gradients. On the other hand, the $\nu^{(4)}$- coefficient is turned off in regions of high pressure gradients. The values of ϵ_2 and ϵ_4 used here are 0.25 and 0.004, respectively.

Equation (4.25) with added artificial viscosity terms, given by Eqs. (4.26) through (4.30), is solved by central-differencing, finite-volume methods, which use four-stage Runge-Kutta time stepping.

In this IE-EE scheme, the IE-SC scheme is used to locate the shock. Once the shock is captured, a fine grid is constructed within the small embedded domain around the shock. Figure 4.9 shows a typical embedded Euler domain inside an IE domain.

The iterative procedure of the IE-EE scheme is shown in Fig. 4.10 and it is described as follows:

Step 1 - Shock-Capturing of IE Computations:

In this step, the IE-SC scheme is used. The scheme is carried out until the location of the shock is fixed. The purpose of this step is to predict the shock location and to provide the boundary and initial conditions for the Euler domain.

Step 2 - Euler Computations:

After the shock is captured, a small parallel quadrilateral fine-grid Euler domain is constructed around the shock. By using a bilinear interpolation of the

velocity components and the density obtained in Step 1, the corresponding distributions are obtained on the Euler grids. These distributions provide the initial and boundary conditions. The pressure, p, is calculated by Eq. (3.77).

The boundary conditions at the upstream and top boundaries are obtained from IE solutions and they are fixed during the unsteady time-marching, while the boundary conditions at the downstream boundary are updated by using linear extrapolation from the interior cells. At the airfoil surface, the boundary conditions are satisfied by using the normal-momentum equation as given by Eq. (3.78). Moreover, the central-differencing artificial viscosity terms given by Eqs. (4.27a) through (4.30) are replaced by corresponding forward- differencing terms at the first two layers above the airfoil surface.

The central-differencing, finite-volume Euler equation, Eq. (4.25), is solved in this Euler domain by using a four-stage Runge-Kutta time stepping procedure.

Step 3 - Updating the B.C.'s by IE Computations:

Fixing the values of the velocity components and the density obtained by the Euler computations, the integral equation calculations are carried out once in the IE domain outside the Euler domain to update the boundary conditions for the next Euler computation.

Step 4 - Euler Computations:

With the initial conditions obtained from the previous Euler computation and the boundary conditions interpolated from the previous IE computations, the Euler equations are solved again.

Step 5 - Convergence Criterion:

If the maximun residuals reach an order of 10^{-3}, the computations stop; otherwise Steps 3 and 4 are repeated.

Since Euler equations do not assume isentropic flow, the entropy increases across the shock and vorticity is produced behind the shock. On the other hand, the Euler domain boundary conditions are obtained from the solution of a potential flow. Therefore, one has to extract the vorticity from the flow at the downstream boundary of the Euler domain. This is accomplished as follows: During the solution of the Euler equations within its domain, the dowmstream boundary conditions are updated. When the IE computation is performed, an overlap region between the Euler equation domain and the IE domain is created, where the IE solution is also used.

The size of the Euler domain is determined by the strength of the shock. The Euler domain is increased with increases in the shock strength. The height of the Euler domain should be made such that the entire shock is included inside the Euler domain.

Chapter 5

COMPUTATIONAL SCHEME OF UNSTEADY TRANSONIC FLOWS

The computational scheme for unsteady transonic flows is presented in this chapter. The Integral Equation with Shock-Capturing (IE-SC) scheme for steady flows has been extended to treat unsteady transonic flows. Although the scheme is applied to airfoil pitching motion in the present work, the scheme is capable of treating the most general unsteady motions. In the first section, the time marching iterative cycle of the unsteady IE-SC scheme is described after the discretization of the integral equation solution is presented. In the second section, the wake point vortex generation procedure is described.

5.1 Unsteady IE-SC Scheme

For general unsteady flows, the governing equations are simple to solve if the body-fixed moving frame of reference is used. A major advantage of this description is that the computational grid is moving with the body. Therefore, no grid-motion computations are required for rigid airfoils. In Chapter 3, the full-potential equation and the associated boundary conditions for unsteady airfoil pitching motions, Eqs. (3.59) through (3.70), have been derived in the body-fixed moving frame.

The integral equation solution of the unsteady full-potential equation, Eq. (3.59), is given by Eq. (3.72) in terms of the absolute velocity field, $\nabla\Phi(x,y,t)$. Due to the fact that the body-fixed moving frame of reference is used in the formulation of the problem, the computational domain is fixed in that frame of reference

and moves with it. Consideration of the motion of the grid is necessary only if the body is deforming; a case which is not considered in the present dissertation.

After discretization of the integral equation solution, Eq. (3.72) becomes

$$\begin{aligned}\nabla\Phi(x,y,t) = &\frac{1}{2\pi}\sum_{k=1}^{N}\int_{g_k}\gamma_{g,k}(s,t)\frac{(y-\eta)\vec{i}-(x-\xi)\vec{j}}{(x-\xi)^2+(y-\eta)^2}ds \\ &+\frac{1}{2\pi}\sum_{i=1}^{IM}\sum_{j=1}^{JM}G_1(t)_{i,j}\int\int_{A_{i,j}}\frac{(x-\xi)\vec{i}+(y-\eta)\vec{j}}{(x-\xi)^2+(y-\eta)^2}d\xi d\eta \\ &+\frac{1}{2\pi}\sum_{i=1}^{IM}\sum_{j=1}^{JM}G_2(t)_{i,j}\int\int_{A_{i,j}}\frac{(x-\xi)\vec{i}+(y-\eta)\vec{j}}{(x-\xi)^2+(y-\eta)^2}d\xi d\eta \\ &+\frac{1}{2\pi}\sum_{k=1}^{M(t)}\gamma(t)_{w,k}\int_{w_k}\frac{(y-\eta)\vec{i}-(x-\xi)\vec{j}}{(x-\xi)^2+(y-\eta)^2}ds\end{aligned} \tag{5.1}$$

where N is the total number of airfoil surface panels, $IM \times JM$ is the total number of field elements, and $M(t)$ is the total number of wake point vortices or wake vortex panels, which is a function of the time.

In Eq. (5.1), it should be noted that the integral term of the shock panel contribution is absorbed into two volume integral terms – the second and third intgral terms in Eq. (5.1), because the Shock-Capturing (SC) rather than Shock-Fitting (SF) scheme is used. Also, it should be noted that the surface source (q_g) integral term is not included in Eq. (5.1), because surface vortex paneling is applied in the present unsteady computations.

Similar to the steady flow case, a linear, distributed surface vortex panel, given by Eq. (4.2b), and constant distributed compressibility terms, G_1 and G_2, are used in the unsteady computations. Wake point vortex or a constant distributed wake vortex panel modeling can be employed. If wake point vortex modeling is used, the last integral term in Eq. (5.1) becomes an algebraic term, which is given by

$$\frac{1}{2\pi}\sum_{k=1}^{M(t)}[\gamma(t)_{w,k}\Delta s_{w,k}]\frac{(y-y_w)\vec{i}-(x-x_w)\vec{j}}{(x-x_w)^2+(y-y_w)^2} \tag{5.2}$$

where $[\gamma(t)_{w,k}\Delta s_{w,k}]$ is the strength of the wake point vortex; and (x_w, y_w) is the coordinate of the wake point vortex. The surface panels and the field-elements in this unsteady computation are constructed in the same way as those in the steady flow computation, which are given by Figs. 4.1 and 4.2. The coordinate system is already shown in Fig. 3.2.

The main differences between the steady and the unsteady integral equation solutions are due to the unsteady contribution of the G_2-integral term in Eq. (5.1) and the unsteady contribution in the computation of density, Eq. (3.62). Moreover, this unsteadiness is partially represented by the shedding of the wake vorticity. The generation of the wake point vortex or vortex panels is of one of the most important parts of the unsteady flow modeling.

The unsteady IE-SC scheme is a time marching iterative scheme, which is outlined as follows: Starting with the initial conditions, which may be steady flow conditions or fluid at rest, one solves Eq. (5.1) with G_1 and G_2 given by Eqs. (3.60) through (3.62) and with boundary conditions given by Eqs. (3.63), (3.65), (3.67) through (3.69) iteratively at each time step. By the end of the iteration at each time step, we obtain the necessary distribution values; γ_g, γ_w, G_1 and G_2. The wake point vortices or panels are generated during each time step and updated at each iteration.

The unsteady IE-SC time-marching, iterative scheme is shown in Fig. 5.1 and is described as follows:

(I) At Time Step (n=0) - Steady Flows:

Let the time step, $n = 0$, correspond to the steady flow problem, and solve the steady flow problem using the steady IE-SC scheme to obtain the initial conditions.

In order to start the unsteady computation directly from steady flows, it is helpful to update the steady airfoil surface vortex distributions by including the unsteady contribution of the rate of change of angle of attack, $\dot{\alpha}$, in Eq. (3.60) and fixing the angle of attack at the initial (steady flow) position. By doing this, the wake point vortices or vortex panels generated during the unsteady computations are much more stable. After updating surface vortex distributions, one obtains $\gamma_g^{(o)}$, where the superscript (o) refers to the time step, $n = 0$.

(II) At Time Step (n) - Unsteady Time Marching Iterative Scheme:

From the previous time steps, $(n-1)$, and $(n-2)$, one has already obtained all necessary distribution values at $(n-1)$ and $(n-2)$ time levels, with the exception of $n = 1$ where the necessary distribution values at $(n-1)$ time level are obtained. At the time step (n), the airfoil changes its orientation according to Eq. (3.7), and thus one obtains new angle of attack, rate of change of angle of attack and time-step size, $\alpha^{(n)}, \dot{\alpha}^{(n)}$ and $(\Delta t)^n$, respectively. The rate of change of angle of attack is calculated numerically as

$$\dot{\alpha}^{(n)} = \frac{\alpha^{(n)} - \alpha^{(n-1)}}{(\Delta t)^n} \tag{5.3}$$

where supercripts, $(n), (n-1)$, etc., refer to time steps. One continues the iteration cycle to solve for the necessary distribution values at the (n) time level until the solution converges. The iteration cycle for the time step (n) can be described as follows:

Step 1 - Enforcing the Boundary Conditions:

In this step, Eq. (5.1) is used to calculate the absolute velocity at the airfoil surface control points and the relative velocity is calculated, according to Eq. (3.10), as

$$\begin{aligned}\vec{V}_r &= \nabla\Phi(x,y,t) - \vec{e}_o - (\dot{\alpha}\vec{k}) \times \vec{r} \\ &= (u + \cos\alpha + \dot{\alpha}y)\vec{i} + [v - \sin\alpha - \dot{\alpha}(x - x_p)]\vec{j}\end{aligned} \tag{5.4}$$

After one obtains the relative velocity at each control point, Eq.(3.63) is applied to enforce the no-penetration condition and to obtain the airfoil vortex distribution at time level (n), $\gamma_g^{(n)}$.

Step 2 - Wake Point Vortex Generation:

The change of the angle of attack in an unsteady motion corresponds to vorticity shedding in the form of a vortex strip along the trailing edge with the local relative velocity. In the present work, the shed vortex strip is modeled by a lumped point vortex. By using Eqs. (3.68) and (3.69), the wake point vortices are generated and thus we obtain $\gamma_{w,k}^{(n)}$ for $k = 1$ to n. The details of the wake point vortex generation are described in the next section.

Step 3 - Computation of $\Phi_t'^{(n)}$:

The time derivative term of the potential, $\Phi_t'^{(n)}$, can be calculated by $\Phi^{(n)}$ and $\Phi^{(n-1)}$, and hence the potential, $\Phi^{(n)}$ and $\Phi^{(n-1)}$ must be calculated by integration of the velocity field numerically. In order to avoid numerical error when doing this numerical integration of velocity, Eq. (3.62) is used to compute the $\Phi_t'^{(n)}$ distributions. Thus, Eq. (3.62) takes the form

$$\Phi_t'^{(n)} \equiv \left(\frac{\partial'\Phi}{\partial t}\right)^{(n)} = \frac{1}{(\kappa-1)M_\infty^2}[1-(\rho^{(n-1)})^{\kappa-1}]$$
$$+\frac{1}{2}\{-(\Phi_x^{(n-1)}+\cos\alpha^{(n)}+\dot{\alpha}^{(n)}y)^2$$
$$-[\Phi_y^{(n-1)}-\sin\alpha^{(n)}-\dot{\alpha}^{(n)}(x-x_p)]^2 \qquad (5.5)$$
$$+(\cos\alpha^{(n)}+\dot{\alpha}^{(n)}y)^2+[\sin\alpha^{(n)}+\dot{\alpha}^{(n)}(x-x_p)]^2\}$$

where the Φ_x, Φ_y and ρ values at time level $(n-1)$ are replaced by the values at time level (n) and previous iteration, starting from the second iteration.

Step 4 - Computation of Relative Velocity Fields, $\vec{V}_r^{(n)}$:

Equations (5.1) and (5.4) are used to compute the relative velocity field. For Eq. (5.1), the vortex distributions for the airfoil surface vortex panels and the wake point vortices are already known from Steps 1 and 2, respectively and the values of $G_1(x,y,t)$ and $G_2(x,y,t)$ are also obtained in the previous iteration or the previous time step $(n-1)$ (for the first iteration of the time step (n)). Only for the first time step $(n=1)$ at the first iteration, G_2 is set equal to zero.

Step 5 - Computation of $\rho^{(n)}$ and $G_2^{(n)}$:

After one computes $\Phi_t'^{(n)}$ in Step 3 and $\nabla\Phi^{(n)}$ in Step 4, we use Eq. (3.62) again to calculate the density distributions as given by

$$\rho^{(n)} = \rho(\nabla\Phi^{(n)}, \Phi_{t'}^{(n)}, \alpha^{(n)}, \dot{\alpha}^{(n)}) \qquad (5.6)$$

In order to compute $G_2^{(n)}$, one must first calculate the time derivative of density, $\rho_t'^{(n)}$. The value of $\rho_t'^{(n)}$ is calculated numerically by second-order accurate backward-differencing, which is given by

$$\rho_t'^{(n)} \equiv \left(\frac{\partial'\rho}{\partial t}\right)^{(n)} = \frac{c_1\rho^{(n-2)}+c_2\rho^{(n-1)}+c_3\rho^{(n)}}{c_4} \qquad (5.7)$$
$$+0[(\Delta t^{(n-1)})^2, (\Delta t^{(n)})^2]$$

where

$$
\begin{aligned}
c_1 &= 1 \\
c_2 &= -\left(\frac{\Delta t^{(n-1)} + \Delta t^{(n)}}{\Delta t^{(n)}}\right)^2 \\
c_3 &= c_2^2 - 1 \\
c_4 &= -(\Delta t^{(n-1)} + \Delta t^{(n)}) + \frac{(\Delta t^{(n-1)} + \Delta t^{(n)})^2}{\Delta t^{(n)}}
\end{aligned}
\tag{5.7a}
$$

Equation (3.61) is then used to calculate $G_2^{(n)}$. One exception is for $n = 1$, where first-order accurate backward-differencing is used.

Step 6 - Computation of $M^{(n)}, \rho_x^{(n)}, \rho_y^{(n)}$ and $G_1^{(n)}$:

Equation (4.15) is used to compute the local Mach number based on the relative velocity field. For these unsteady computations, Eq. (4.15) takes the form

$$
M^{(n)}(x,y,t) = \frac{M_\infty |\vec{V}^{(n)}(x,y,t)|}{[\rho^{(n)}(x,y,t)]^{\frac{\kappa-1}{2}}} \tag{5.8}
$$

After the local Mach numbers are obtained, the Murman-Cole type differencing is used to calculate the spatial derivatives of $\rho_x^{(n)}$ and $\rho_y^{(n)}$. Then Eq. (3.60) is used to calculate $G_1^{(n)}$.

Step 7 - Computation of Surface Pressure Coefficients, $C_p^{(n)}$:

The surface pressure coefficient, $C_p^{(n)}$, is calculated using Eq. (4.9) with the density given by Eq. (3.62).

Step 8 - Convergence Criterion:

If $C_p^{(n)}$ conveges at every surface control point, then we go to the next time step $(n+1)$; otherwise, Steps 1-8 are repeated to update all quantities at time level (n).

(III) At Time Step $(n+1)$:

The airfoil changes its orientation to another position and Steps 1-8 are repeated for time step $(n+1)$.

5.2 Wake Point Vortex Generation

As mentioned before, the change of the angle of attack during the unsteady pitching motion corresponds to vorticity shedding from the trailing edge. The generation of the wake point vortices has been discussed in Step 2 of the section above. Now, more details on the generation, as shown in Fig. 5.2, are given below:

(I) At Time Step $(n=0)$:

This time step corresponds to the steady flow, and hence there is no wake vorticity shedding from the airfoil trailing edge.

(II) At Time Step $(n=1)$:

When the airfoil changes angle of attack from $\alpha^{(o)}$ to $\alpha^{(1)}$, a strip of vorticity is shed from the airfoil trailing edge. The shed vorticity is modeled by a lumped point vortex which is placed at the middle point or at the end of this strip. The direction of this vortex strip is determined by Eq. (3.68) or by the fact that the local relative velocity is tangential to the vortex strip. The length of the strip, $\Delta s_{w,1}$, is determined by

$$\Delta s_{w,1}^{(n)} = |\vec{V}_r|_{TE}^{(n)} (\Delta t)^{(n)} \tag{5.9}$$

where $|V_r|_{(TE)}^{(n)}$ is the relative velocity at trailing edge and the second subscript, 1, refers to the first point vortex. The strength of the wake point vortex is determined

by Eq. (3.69), or equivalently by

$$\left(\frac{\Gamma}{\rho}\right)_{w,1}^{(n)} = \left[\sum_g \left(\frac{\Gamma}{\rho}\right)_g\right]^{(n-1)} - \left[\sum_g \left(\frac{\Gamma}{\rho}\right)_g\right]^{(n)} \tag{5.10}$$

where the summation is taken over the airfoil surface and Γ is the total vortex over the airfoil surface panel ($\Gamma \equiv \int_{panel} \gamma dl$) or the strength of the lumped wake point vortex.

The firste wake point vortex developed in the time step ($n = 1$) has thus been generated. The location and the strength of this point vortex is updated during this time step and at each succeeding iteration.

(III) <u>At Time Step ($n = 2$)</u>:

When the airfoil changes its angle of attack from $\alpha^{(1)}$ to $\alpha^{(2)}$, a new point vortex is shed from the trailing edge while the old point vortex, shed during the previous time step, is now convected downstream with the local relative velocity. The location and the strength of the newly shed, point vortex is determined in the same way as that of the time step ($n = 1$), where Eqs. (5.9) and (5.10) are used to obtain $\Delta s_{w,1}^{(2)}$ and $\Gamma_{w,1}^{(2)}$, respectively. The strength of the old point vortex is kept constant, or

$$\Gamma_{w,2}^{(2)} = \Gamma_{w,1}^{(1)} \tag{5.11}$$

In general, we have

$$\Gamma_{w,k}^{(n)} = \Gamma_{w,k-1}^{(n-1)} \tag{5.11a}$$

Therefore at time step ($n = 2$), there are two wake point vortices in the flow field. The generation of the first point vortex and the convection of the old point vortices are updated at each iteration.

(IV) At Time Step ($n = 3, 4....$):

In general, when the airfoil changes its orientation, a new wake vortex strip is shed from trailing edge. At the same time, all the old point vortices are convected downstream with the relative velocity.

The generation of the wake vortex is one of the most important parts of the unsteady integral equation method. The procedure described above has been tested and shown to be very stable.

Chapter 6

NUMERICAL RESULTS

In order to implement the IE-SC, IE-SCSF and IE-EE schemes for steady transonic flows, two scalar programs have been developed; the first is for the IE-SC and IE-SCSF schemes and the second is for the IE-EE scheme. The code has been applied to an NACA 0012 airfoil and a NACA 64A010A (Ames Model) airfoil at different Mach numbers and different angles of attack. Then the computer code for the integral equation solution of the IE-SC scheme for the steady transonic flows has been extended to that for unsteady transonic flows. The unsteady computation has been made on the NACA 0012 airfoil undergoing pitching motion. In the first section, the numerical results for the steady transonic flows are presented along with comparisons with other numerical results and experimental data; while in the second section, the unsteady transonic flow solutions by the unsteady IE-SC scheme are presented.

Most of the computations are applied to the NACA 0012 airfoil. This is a symmetric, round leading edge airfoil with 12% thickness. The coordinates of the airfoil surfaces are given by the equation [140]

$$\begin{aligned} y = \pm 0.6(&0.2969\sqrt{x} - 0.1260x \\ &- 0.3516x^2 + 0.2843x^3 - 0.1015x^4) \end{aligned} \tag{6.1}$$

The NACA 64A010A airfoil is a NASA Ames Research Center model airfoil, which has an actual thickness of about 10.6% with a small camber. The coordinates of this airfoil are tabulated in Ref. [140].

6.1 Steady Transonic Flow Solutions

The numerical results for steady flows will be presented in this section in three parts: (i) shock-free flow solutions, (ii) IE-SC and IE-SCSF solutions for transonic flows, and (iii) IE-EE solutions for transonic flows including flows with strong shocks.

6.1.1 Shock-Free Flow Solutions

The initial step in the code development for transonic flows was aimed at examining solutions for shock-free flows, which include incompressible and compressible high subsonic flows. The purpose of the work in this part is to examine the accuracy of the method applied to near critical flows and to provide the appropriate parameters, such as the number of airfoil surface panels, the size of the computational domain, etc., for transonic flow computations.

The first numerical test was aimed at comparing the results of the standard panel scheme using linear distributed source panels with those using linear distributed vortex panels for symmetric incompressible flows; the results of this test are shown in Fig. 6.1 for the NACA 0012 airfoil. The number of airfoil surface panels was determined numerically to be 50 panels each on the upper and lower airfoil surfaces. Around the leading edge, small panels were used, while uniform panels were used everywhere else for shock-free flows. By comparing the results with experimental data [141] shown in Fig. 6.1, it is obivious that the IE solution with linear distributed surface vortex panels is superior to that of the source panels.

The same test was also made for a lifting flow case. Figure 6.2 shows the results for this test with the same airfoil at $M_\infty = 0$ and $\alpha = 9^o$. In this test, we compared the IE solutions obtained using the linear distributed vortex panels with the analytical approximate solution [142]. Again, we found that the IE solution, with the linear distributed vortex panels, was much better than the one with source and vortex panels. The number of surface panels was the same as that given in Fig. 6.1.

Next, we consider the computation of the compressible shock-free flows at high subsonic Mach numbers. The test on the vortex vs. source panel models was also applied to the NACA 0012 airfoil at $M_\infty = 0.72$ and $\alpha = 0^o$. The results, along with a comparison with the Euler solution [143], are shown in Fig. 6.3. This test showed the same relative superiority of the vortex panel model. The computational domain used to compute the compressibility was 2×1.5 chord: 0.5 chord ahead and behind the airfoil in the x-direction and 0.75 chord above and below the airfoil, as shown in Fig. 4.2. A total number of 64×60 field- elements was used around the airfoil.

The second numerical test was to check the sensitivity of the IE solution to the size of the computational domain. Figures 6.4 and 6.5 show such results for two domain sizes: 2×1.5 and 3×2.5 chord, for symmetric and lifting flows, respectively. Figure 6.4 is for the NACA 0012 airfoil at $M_\infty = 0.72$ and $\alpha = 0^o$ while Fig. 6.5 is for the same airfoil at $M_\infty = 0.63$ and $\alpha = 2^o$. Several different sizes for the computational domains were tested and it was found that sufficient engineering accuracy was obtained when the domain was as small as 2×1.5 chord. It can been seen from the figures, that a computational domain of 2×1.5 gives solutions which are as accurate as those of the 3×2.5 computational domain. The total number of field-elements used in these two computational domains were both 64×60. Also,

a computational domain of 3×2.5 with 80×80 field elements was used and the results did not show appreciable changes from those of the 2×1.5 and 64×60 case. For the purpose of engineering accuracy vs. computational cost, the domain of 2×1.5 chord with 64×60 field-elements will be used for shock-free flows and for transonic flows with shocks of weak to moderate strength. In these tests, the linear distributed surface vortex panels are used. The comparison of the lifting case for the domain of dimension 2×1.5 with other finite-difference solutions [144,145] is shown in Fig. 6.6. The number of iterations used to achieve a convergent solution in all above compressible flow cases was six.

After we finished these numerical tests for shock-free flows, we proceded to compute transonic flows, which was our main interest. Several conclusions can be drawn from above tests:

(i) A total number of 100 surface panels with linear distributed vorticity is sufficient to get an engineering accurate solution for shock-free flows. However, for flows with shocks, a total number of 140 panels will be used due to the panel refinement requirement around the shock.

(ii) Linear distributed surface vortex panel modeling is much better than the linear distributed surface source panel modeling or the mixed source-vortex panel modeling when used with flat panels. Therefore the linear distributed vortex panels will be used for the transonic flow computations.

(iii) For the purposes of engineering accuarcy vs. computational cost the computational domain of 2×1.5 will be used for the transonic flow computations, except for the strong shock case where a larger domain will be used. The total number of the field-elements is 64×60 in this domain.

(iv) The IE solutions for the shock-free flows compare very well with the experimental data and other numerical results. For both symmetric and

lifting incompressible flows, the present solutions with the vortex panels match accurately the experimental data and the approximate analytic solution as shown in Figs. 6.1 and 6.2. For symmetric compressible flow as shown in Fig. 6.3, the IE solution with vortex panels and a computational domain of 2×1.5 chord gives excellent results for near critical flows. Also for lifting, compressible flows, the IE solutions provide acceptable results, except that a slight underprediction of the peak pressure exists in the solution when compared with finite-difference computational results [144,145].

6.1.2 IE-SC and IE-SCSF Solutions for Transonic Flows

For transonic flow computations, a total of 140 linear distributed surface vortex panels has been used. The surface panels were refined in the region around the shock. The computational domains used in the analysis presented in this subsection are all 2×1.5 chord, as determined earlier, and the total number of field-elements is 64×60 with the finer elements around the shock, as shown in Fig. 4.2.

First, a numerical test case is presented to show the effect of introducing the shock panels and their fitting as explained earlier. Figure 6.7 shows a comparison between the IE-SC results and the IE-SCSF results for the NACA 0012 airfoil at $M_\infty = 0.8$ and $\alpha = 0^o$. Convergence is achieved in the IE-SC scheme after 40 iterations. In the IE-SCSF scheme, convergence is achieved after 25 SCSF-iterations, in which 12 SC-iterations are taken to locate the shock and 13 SF-iterations are taken to fit the shock. It is clear that the IE-SCSF scheme sharpens the shock, as expected, with this relatively coarse grid and that the IE-SCSF scheme is more efficient computationally in its treatment of the shock than the IE-SC scheme.

Next, we compare the IE-SCSF results with experimental data and with other computational results. Figure 6.8 shows the results of the IE-SCSF scheme for NACA 0012 airfoil at $M_\infty = 0.8$ and $\alpha = 0^o$, along with the comparisons with the computational results of Garabedian, Korn and Jameson [144], and the experimental data taken from reference [146]. It can been seen that the shock strength and the shock location predicted by the current IE-SCSF scheme compare well with the experimental data [146] and the FD-solutions [144], except that the peak pressure is slightly underpredicted.

Figure 6.9 shows the results of the IE-SCSF scheme for the lifting flow case of an NACA 0012 airfoil at $M_\infty = 0.75$ and $\alpha = 2^o$ along with the computational results for the non-conservative full-potential FD-solution of Steger and Lomax [29] and the FD conservative Euler solution of Steger [147]. This case is approaching a strong shock case. The number of SCSF-iterations used to achieve convergence is the same as that for the case given in Fig. 6.8. The comparisons show that the current IE-SCSF solution agrees well with the full-potential solution [29], and it also shows that the location of the shock predicted by the SCSF-scheme is slightly upstream when compared with the Euler solution [147]. Also, the underprediction of the peak value of the pressure is noted as already seen in the earlier compressible shock-free lifting flow computation (Fig. 6.6).

The computation of the IE-SCSF scheme has also been carried out on another airfoil: NACA 64A010A. Figure 6.10 shows the results for that airfoil at $M = 0.796$ and $\alpha = 0^o$, along with a comparison with the computational results of Edwards, Bland and Seidel [92] who used the TSD-equation, and with experimental data taken from reference [92]. The present results compare very well overall, including the shock location. The number of SCSF-iterations used to achieve the convergence remained 12 SC-iterations and 13 SF-iterations.

6.1.3 IE-EE Solutions for Transonic Flows

The IE-SCSF scheme produces good solutions for the transonic flows with shocks of moderate strength. The location and strength of the shock are predicted correctly by the IE-SCSF scheme. But for the transonic flows with the strong shocks, the IE-SCSF scheme may not give accurate solutions. Here the Integral Equation with Embedded Euler domain (IE-EE) scheme has been developed and the computations have been carried out for flows with shocks of moderate strength as well as for strong shocks.

The first three cases of the IE-EE scheme are the same as those of the IE-SCSF scheme presented in the previous subsection. Figure 6.11 shows the results of the IE-EE scheme for the same case as shown in Fig. 6.8 along with the comparison with the computational results of Jameson et al. [48], who also used a finite-volume Euler scheme with four-stage Runge-Kutta time stepping. In the present IE-EE scheme, the integral equation domain is still 2×1.5 with 64×60 field-elements while the embedded Euler domain has a size of 0.5×0.6 around the shock region with a grid of 25×30, as shown in Fig. 4.9. This case took 10 SC-iterations to locate the shock, 250 time steps of the Euler solution to achieve a residual error of 10^{-3} and 5 IE-iterations to update the Euler domain boundary conditions. The IE-EE results predict a stronger shock, as compared with the experimental data of Fig. 6.8, typical of Euler results. Also, the IE-EE scheme over predicts the pressure behind the shock when compared with the Euler results of Jameson et al. [48]. This may be attributed to the short overlap between the Euler domain and the IE domain.

Figure 6.12 shows the IE-EE solution for the NACA 0012 airfoil at $M_\infty = 0.75$ and $\alpha = 2^\circ$. The sizes of the IE-domain and Euler domain and the number of IE field-elements and the Euler grid resolution are all the same as those used in the

case of Fig. 6.11. The numbers of IE-iterations and Euler-time steps are also same as those of Fig. 6.11. The FD Euler solution of Steger [147] is shown in Fig. 6.12. Comparison indicates that the IE-EE solution yields results which are close to the conservative Euler solutions, in terms of the strength and location of the shock, in this near strong shock flow case than those predicted by the IE-SCSF scheme shown in Fig. 6.9.

The third case of the IE-EE solution is made on an NACA 64A010A airfoil at $M_\infty = 0.796$ and $\alpha = 0^o$ as shown in Fig. 6.13. In this case a slightly larger Euler domain of 0.7×0.6 around the shock region with a grid of 35×30 was used, and consenquently, the number of Euler time steps required to achieve the same residual error of 10^{-3} was reduced. It took 10 SC-iterations to locate the shock, 130 Euler time steps to achieve a convergent solution and 3 IE-iterations to update the Euler domain boundary conditions. The comparisons of the current IE-EE results with other computational results [92] and the experimental data taken from reference [92] are shown in Fig. 6.13. Again, it is noticed that the IE-SCSF scheme predicts a slightly weaker shock (as shown in Fig. 6.10) than the experimental data, while the IE-EE scheme predicts a slightly stronger shock (as shown in Fig. 6.13) than the experimental data.

For stronger shocks than those considered above, both the IE and Euler computational domains are extended in the longitudinal and lateral directions. The Euler domain is extended beyond the trailing edge to allow for the vorticity to be shed downstream, where the overlaping region with the IE domain exists. The next three cases show the IE-EE solutions for the NACA 0012 airfoil at $\alpha = 0^o$ and three different free-stream Mach numbers: $M_\infty = 0.812, 0.82$ and 0.84, respectively.

Figure 6.14 shows the results for the IE-EE scheme for the NACA 0012 airfoil at $M_\infty = 0.812$ and $\alpha = 0^o$ along with the experimental data taken from reference

[146]. In Fig. 6.15, the results of the IE-EE scheme for the same airfoil at $M_\infty = 0.82$ and $\alpha = 0^\circ$ are shown along with the three-dimensional solution for the wing root chord of Tseng and Morino [118], who used the IEM for the TSD equation, and the same three-dimensional FD solution of reference [148]. The size of the embedded Euler domain for these two cases is 0.8×0.8 with a 40×40 grid. This case took 10 SC-iterations to locate the shock, 130 Euler time steps to achieve a residual error of 10^{-3} and 3 IE-iterations to update the boundary conditions. The comparisons shown in Figs. 6.14 and 6.15 are considered satisfactory.

Final case is a typical strong shock flow case, which is for an NACA 0012 airfoil at $M_\infty = 0.84$ and $\alpha = 0^\circ$. Figure 6.16 shows a computational domain used in this case. The size of the integral equation domain is 3×6 chord lengths and the Euler domain is 1.5×1.0 with a grid of 60×40. The results of the IE-EE scheme for this case are shown in Fig. 6.17 along with comparisons with the finite-volume Euler equation solution of Jameson et al. [48] and with the non-isentropic FP-solution of Whitlow et al. [47]. This case took 10 IE-iterations to locate the shock, 300 Euler time steps to achieve a residual error of 10^{-3} and 3 IE-iterations to update the Euler domain boundary conditions. The present IE-EE results compare very well with the Euler solution of Jameson et al. [48] both in the strength and in the location of the shock. For this particular case, it is worth mentioning that the finite-difference solution of the conservative full-potential equation yields a multiple solution for this symmetric flow [43], as mentioned in Chapter 2, but the present IE-solution did not show such nonuniqueness and neither did the IE-EE solution.

Since the Euler equations do not assume isentropic flow, one must extract the vorticity from the flow at the downstream boundary of the Euler domain as mentioned earlier. The downstream boundary conditions are updated during the Euler time-march in all of the above IE-EE computations and also, an overlap

region is created where the IE computation is carried out to clean the oscillation produced at the region near the downstream boundary of the Euler domain during the embedded Euler domain computations. The size of the overlap region increases with increases in the shock strength, and it decreases with the increase in the size of the embedded Euler domain.

A CYBER-185 computer at NASA-Langley Research Center was used. For 64×60 field elements, on that computer, an IE-iteration cycle took about 200 CPU seconds. For 25×30 cells, an Euler cycle took about 2 CPU seconds on the same computer.

6.2 Unsteady Transonic Flow Solutions

The unsteady IE-SC scheme has been applied to the NACA 0012 airfoil at a free-stream Mach number of 0.755 undergoing forced pitching oscillation around a pivot point at the quarter-chord, measured from the leading edge ($x_p = 0.25$). The angle of attack, $\alpha(t)$, is given by Eq. (3.7) as follows:

$$\alpha(t) = \alpha_o + \alpha_a \sin(k_c t) \tag{6.2}$$

where

$$\alpha_o = 0.016^o$$

$$\alpha_a = 1.255^o$$

$$k_c = 0.1632$$

Figures 6.18, 6.19 and 6.20 show the present computed results along with a comparison with the finite-volume Euler solution produced by Kandil and Chuang [106] who used an implicit approximately factorized Euler solver.

The initial condition corresponds to the steady flow solution at mean angle of attack, $\alpha_o = 0.016^o$, with $M_\infty = 0.755$. The computed steady solution is shown in Fig. 6.18 along with the comparison with the Euler solution produced by Reference

[106]. The comparison shows that the steady peak pressure predicted by the present IE-SC scheme is lower than that of the Euler solution, a typical relation between the present IE-SC solutions and the Euler solutions as seen in the previous steady computations. Figures 6.8 and 6.11 have already shown this relation, where the peak pressure predicted by IE-SCSF scheme (Fig. 6.8) is slightly lower than that of experimental data while the peak pressure predicted by the Euler solution (Fig. 6.11) is higher than that of the experimental data.

Figure 6.19 shows the computed periodic lift coefficient, C_N, for this pitching motion case. The lift coefficient, C_N, is calculated by

$$C_N = \int_0^1 (C_{pl} - C_{pu}) dx \tag{6.3}$$

The comparison with the Euler solution produced by Reference [106] shown in Fig. 6.19 is satisfactory. Figure 6.20 shows the corresponding periodic unsteady surface pressure coefficients for one cycle of the motion along with a comparison with the Euler solution produced by Reference [106]. The comparison shows that the unsteady pressure history is consistant with that of the Euler solution [106], except that the upper and lower surface peak pressure coefficients are lower than those of the Euler solution [106]. This difference has already existed in the steady initial condition as shown in Fig. 6.18. The unsteady motion of the shock, which includes the change of the shock strength, generation and loss of the shock, and the change of the shock location, is in a good agreement with the Euler solution [106], except that the shock strength is smaller than that of the Euler solutions [106].

The computational domain used in this unsteady flow case is same as that for most of the steady computations: 2×1.5 chord lengths with 64×60 field-elements. A total of 102 uniform time steps were used for one cycle of the computation and the number of iterations ranged from 10 to 20 per time step to achieve the convergence

for one time step. The periodic solution was obtained after 2 cycle. The CPU time for one iteration is almost the same as that for the steady IE iteration.

Most of the steady and unsteady transonic flow computational results presented here have been presented in References [149-153].

Chapter 7

CONCLUSIONS AND RECOMMENDATIONS

The integral equation (IE) solution for the full-potential equation has been presented for steady and unsteady transonic airfoil flow problems. The method has also been coupled with an embedded Euler domain solution to treat flows with strong shocks for steady flows.

For steady transonic flows, three IE schemes have been developed. The first two schemes are based on the integral equation solution of the full-potential equation in terms of the velocity field. The Integral Equation with Shock-Capturing (IE-SC) and the Integral Equation with Shock-Capturing Shock-Fitting (IE-SCSF) schemes have been developed. The IE-SCSF scheme is an extension of the IE-SC scheme, which consists of a shock-capturing (SC) part and a shock-fitting (SF) part, in which the shock is captured during the iteration of the SC-part and shock panels are introduced and updated at the shock location during the iteration of SF-part. The shock panels are fitted and the shocks are crossed by using the Rankine-Hugoniot relations in the SF-part of the IE-SCSF scheme. The third scheme is based on coupling the IE-SC integral equation solution of the full-potential equation with the psuedo-time integration of the Euler equation in a small embedded region around the shock. The integral solution provides the initial and boundary conditions for the Euler domain. The Euler solver is a central-difference, finite-volume scheme with four-stage Runge-Kutta time stepping. This scheme has been named the Integral

Equation-Embedded Euler (IE-EE) scheme. These three methods have been applied to different airfoils over a wide range of Mach numbers, and the results are in good agreement with the experimental data and other computational results.

For unsteady transonic flows, the full-potential equation formulation in the moving frame of reference has been used. The steady IE-SC scheme has been extended to treat airfoils undergoing time-dependent motions, and the unsteady IE-SC scheme has thus been developed. The resulting unsteady IE-SC scheme has been applied to a NACA 0012 undergoing a pitching oscillation. The numerical results are compared with the results of an implicit approximately-factored finite-volume Euler scheme. Although the motion of the shock has been predicted correctly, the predicted surface pressure has shown lower peaks compared with those from an Euler solver.

The three steady IE schemes and the unsteady IE-SC scheme are nevertheless efficient in terms of the number of iterations, compared to other existing schemes which use finite-difference or finite-volume methods throughout large computational domains with fine grids. If the influence coefficients of the field-elements are stored in the core memory of the computer, the computational time of the IE-iteration can be reduced substantially since the field-element calculations represent about 80% of the computational time per iteration.

The main focus of this study was to develop IE schemes for transonic flows. The study has shown that the integral equation solution of the full-potential equation can handle transonic flows with shocks correctly. But the IE method is restricted to flows with weak shocks or with shocks of moderate strength. The accuracy of the shock wave prediction is improved substantially by using shock-fitting instead of using fine gridding. The integral equation with an embedded Euler solution can handle transonic flows with strong shocks both accurately and efficiently. For unsteady

transonic flows, the integral equation solution of the full-potential equation has been first developed and the present unsteady IE-SC scheme is capable of generating the shock during the unsteady motion.

The recommendations for further research work in the area of transonic IE methods are drawn as follows:

(1) For steady flows, further development on the IE-EE scheme is recommended. Compatibility conditions between the integral equation domain and the embedded Euler domain need further development, so that the rotational flow behind the shock in the Euler domain can be matched with a corrected potential flow at the downstream boundary. Hence a small embedded Euler domain can been used for strong shock flow problem.

(2) For steady and unsteady flows, a stability analysis of the integral equation method should be developed. For unsteady flows, this work on stability analysis will definitely help in determining the optimun time-step size and hence increase the computational efficiency.

(3) Due to the success of the IE-EE scheme in the steady flow applications, the IE-EE scheme should be applied to unsteady transonic flows. Using the results of recommondations given in (1) and (2), the IE-EE scheme is expected to compete with the existing Euler schemes which are applied throughout the computational domain.

(4) For both steady and unsteady integral equation computations, the increase in computational efficiency per iteration cycle of time step is still an important issue that needs further study. The study must focus on the computational efficiency of the field integral term since it currently represents 80% of the computational time.

(5) The present IE-SCSF and IE-EE schemes are recommended to be extended for three-dimensional steady and unsteady transonic flows.

REFERENCES

1. Molenbroeck, P., "Uber eininge Bewegungen eines Gases bei Annahme eines Geschwindigdeits-potentials," Archiv. Math. und Phys., Series 2, Vol. 9, 1890, pp. 157-195.

2. Chaplygin, S. A., "On Gas Jets," NACA TM 1063, 1904.

3. Cole, J. D., "Twenty Years of Transonic Flow," D1-82-0878, Flight Sci. Lab., Boeing Sci. Res. Lab., July 1969.

4. Oswatitsch, K. and Weigardt, K., "Theoretische Untersuchungen uber stationare Potentialstromungen und Grenzschlichten bei hohen Geschwindigkeitin," Lilienthal-Gesellschaft fur Luftfahrtforschung, Ber 13/1, 1942, pp. 7-24. (Also available as NACA TM 1189.)

5. Busemann, A. and Guderley, K. G., "The Problem of Drag at High Subsonic Speeds," British M. A. P., Rep. and Trans. 184, 1947.

6. Guderley, K. G., "Considerations of the Structure of Mixed Subsonic - Supersonic Flow Patterns," AAFAMC Tech. Rep. F-TR-2168-ND, 1947.

7. Guderley, K. G., "On the Transition from a Transonic Potential Flow to a Flow with Shocks," AAFAMC Tech. Rep. F-TR-2160-ND, 1947.

8. von Karman, T., "The Similarity Law of Transonic Flows," Journal of Mathematics and Physics, Vol. 26, Oct. 1947, pp. 182-190.

9. von Karman, T., "Supersonic Aerodynamics - Principles and Applications," Journal of the Aeronautical Sciences, Vol. 14, July 1947, pp. 373-402 (discussion 403-309).

10. Cole, J. D., "Drag of Finite Wedge at High Subsonic Speeds," Journal of Mathematical Physics, Vol. 30, July 1951, pp. 79-93.

11. Guderley, K. G. and Yoshihara, J., "The Flow over a Wedge Profile at Mach Number 1," Journal of the Aeronautical Sciences, Vol. 17, Nov. 1950, pp. 723-735.

12. Vincenti, W. G. and Wagoner, C. G., "Transonic Flow Past a Wedge Profile with Detached Bow Wave," NACA Rep. 1095, 1952. (Supersedes NACA TN 2339 and 2588).

13. Liepmann, H. W. and Bryson, A. E., Jr., "Transonic Flow Past Wedge Sections," Journal of the Aeronautical Sciences, Vol. 17, Dec. 1950, pp. 745-755.

14. Bryson, A. E., Jr., "An Experimental Investigation of Transonic Flow Past Two-Dimensional wedge and Circular-Arc Sections Using a Mach-Zehnder Interferometer," NACA Rep. 1094, 1952. (Supersedes NACA TN 1560.)

15. Asaka, S., "Application of the Thin-Wing Expansion Method to the Flow of a Compressible Fluid Past a Symmetrical Circular-Arc Aerofoil," Journal of Physical Society of Japan, Vol. 10, June 1955, pp. 482-492; Errata, Ibid., Vol. 10, July 1955, p. 593, and Vol. 13, Jan. 1958, p. 115.

16. Oswatitsch, K., "Die Geschwindigkeitsverteilung bei lokalen Uberschallgebieten an flachen Profilen," ZAMM, Vol. 30, Nr. 1/2, 1950, pp. 17-24.

17. Oswatitsch, K., "Die Geschwindigkeitsverteilung au symmetrischen Profilen beim Auftreten lokaler Uberschallgeiete," Acta Physica Austriaca, Vol. 4, Nr. 2/3, 1950, pp. 228-271.

18. Spreiter, J. R., "On the Application of Transonic Similarity Rules to Wings of Finite Span," NACA Rep. 1153, 1953. (Supersedes NACA TN 2726.)

19. Oswatitsch, K., "Die Theoretischen Arbeiten uber Schallnahe Stromungen am Flugtechnischen Institut der Kungl," Tekniska Hokskolan, Stockholm, Proceedings of the Eighth International Congress on Theoretical and Applied Mechanics, 1953.

20. Oswatitsch, K., "The Area Rule," Applied Mechanics Reviews, Vol.10, Dec. 1957, pp. 543-545.

21. Whitcomb, R. T., "A Study of the Zero-Lift Drag-Rise Characteristics of Wing-Body Combinations Near the Speed of Sound," NACA Rep. 1273, 1956. (Supersedes NACA RM L 52H08).

22. Heaslet, M. A. and Spreiter, J. R., "Three-Dimensional Transonic Flow Theory Applied to Slender Wings and Bodies," NACA Rep. 1318, 1957. (Supercedes NACA TN 3717.)

23. Spreiter, J. R. and Alksne, A. Y., "Thin Airfoil Theory Based on Approximate Solution of the Transonic Flow Equation," NACA Rep. 1359, 1958. (Supersedes NACA TN 3970.)

24. Spreiter, J. R. and Alksne, A. Y., "Slender Body Theory Based on Approximate Solution of the Transonic Flow Equation," NACA TR-R-2, 1958.

25. Alksne, A. Y. and Spreiter, J. R., "Theoretical Pressure Distributions on Wings of Finite Span at Zero Incidence for Mach Numbers Near 1," NACA TR R-88, 1961.

26. Murman, E. M. and Cole, J. D., "Calculation of Plane Steady Transonic Flows," AIAA Journal, Vol. 9, No.1, 1971, pp. 114-121.

27. Ballhaus, W. F. and Bailey, F. R., "Numerical Calculation of Transonic Flow about Swept Wings," AIAA Paper 72-677, June 1972.

28. Bailey, F. R. and Ballhaus, W. F., "Relaxation Methods for Transonic Flow about Wing-Cylinder Combinations and Lifting Swept Wings," Third International Conference on Numerical Methods in Fluid Dynamics, Paris, July 1972.

29. Steger, J. L. and Lomax, H., "Transonic Flow about Two-Dimensional Arifoils by Relaxation Procedures," AIAA Journal, Vol. 10, No. 1, 1972, pp. 49-54.

30. Garabedian, P. R. and Korn, D., "Analysis of Transonic Airfoils," Comm. Pure Appl. Math., Vol. 24, 1972, pp. 841-851.

31. Jameson, A., "Iterative Solution of Transonic Flows over Airfoils and Wings, Including Flow at Mach 1," Comm. Pure Appl. Math., Vol. 27, 1974, pp. 283-309.

32. Jameson, A., "Transonic Potential Flow Calculation Using Conservation Form," Proceedings of the AIAA Second Computational Fluid Dynamics Conference, Hartford, Conn., June 1975, pp. 148-161.

33. Jameson, A. and Caughey, D. A., "Finite Volume Method for Transonic Potential Calculations," Proceedings of AIAA Third Computational Fluid Dynamics Conference, June 1977, AIAA, New York, 1977, pp. 33-54, also AIAA Paper 77-635, 1977.

34. Caughey, D. A. and Jameson, A., "Numerical Calculation of Transonic Potential Flow about Wing-Body Combinations," AIAA Journal, Vol. 17, No. 2, 1979, pp. 175-181.

35. Holst, T. L., "Implicit Algorithm for the Conservative Transonic Full-Potential Equation Using an Arbitrary Mesh," AIAA Journal, Vol. 17, No. 10, 1979, pp. 1038-1045.

36. Hafez, M., South, J. and Murman, E., "Artificial Compressibility Methods for Numerical Solutions for Transonic Full Potential Equation," AIAA Journal, Vol. 17, No. 8, 1979, pp. 838-844.

37. Ballhaus, W. F., Jameson, A. and Albert, J., "Implicit Approximate Factorization Scheme for Steady Transonic Flow Problems," AIAA Journal, Vol. 16, No. 6, 1978, pp. 573-579.

38. Holst, T. L., "Fast, Conservative Algorithm for Solving the Transonic Full-Potential Equation," AIAA Journal, Vo. 18, No. 12. 1980, pp. 1431-1439.

39. Brandt, A., "Multi-Level Adaptive Technique (MLAT) for Fast Numerical Solution to Boudary Value Problems," Lecture Notes in Physics, Vol. 18, 1973, pp. 82-89.

40. Brandt, A., "Multi-Level Adaptive Solutions to Boundary-Valve Problems," Math. Comp., Vol. 31, No. 138, 1977, pp. 333-390.

41. South, J. C. and Brandt, A., "Application of Multi-Level Grid Method to Transonic Flow Calculations," Rept. 76-8, ICASE, 1976.

42. Rizzi, A. and Viviand, H. (editors), "Numerical Methods for Computation of Inviscid Transonic Flow with Shocks," Proceedings of the GAMM Workshop, Stockholm, 1979, Viewveg Verlag, 1981.

43. Steinhoff, J. and Jameson, A., "Multiple Solutions of the Transonic Potential Flow Equation," AIAA Journal, Vol. 21, No. 11, 1982, pp. 1521-1525.

44. Salas, M. D., Jameson, A. and Melnik, R. E., "A Comparative Study of the Nonuniqueness Problem of the Potential Equation," AIAA Paper 83-1888, July 1983.

45. Salas, M. D. and Gumbert, C. R., "Breakdown of the Conservative Potential Equation," Symposium on Aerodynamics, NASA Langley Research Center, Vol. 1, April 1985, pp. 4.3-4.53.

46. Fuglsang, D. F. and Williams, M. H., "Non-Isentropic Unsteady Transonic Small Disturbance Theory," AIAA Paper 85-0600, April 1985.

47. Whitlow, W., Jr., Hafez, M. M. and Osher, S. J., "An Entropy Correction Method for Unsteady Full Potential Flows with Strong Shocks," NASA TM 87769, Langley Research Center, Hampton, VA, 1986.

48. Jameson, A., Schmidt, W. and Turkel, E., "Numerical Solutions of the Euler Equations by Finite-Volume Methods Using Runge Kutta Time-Steping Scheme," AIAA Paper 81-1259, 1981.

49. Caughey, David A., "A Diagonal Implicit Multigrid Algorithm for the Euler Equations," AIAA Paper 87-0354, 1987.

50. Pulliam, H. Thomas, "Artificial Disserpation Models for the Euler Equations," AIAA Journal, Vol. 24, No. 12, 1986, pp. 1931-1940.

51. Deiwert, G. S., "Numerical Simulation of High Reynolds Number Transonic Flow," AIAA Journal, Vol. 13, No. 10, 1975, pp. 1354-1359.

52. Deiwert, G. S., "Computation of Separated Transonic Turbulent Flow," AIAA Journal, Vol. 14, No. 6, 1976, pp. 735-740.

53. Matsushima, K., Obayashi, S. and Fujii, K., "Navier-Stokes Computations of Transonic Flows Using LU-ADI Method," AIAA Paper 87-0421, 1987.

54. Kandil, O. A. and Yates, E. C., Jr., "Computation of Transonic Vortex Flow Past Delta Wings - Integral Equation Approach," AIAA Paper 86-1582, 1985, also AIAA Journal, Vol. 24, No. 11, 1986, pp. 1729-1736.

55. Spreiter, J. R. and Alksne, A. Y., "Theoretical Prediction of Pressure Distributions on Non-Lifting Airfoils at High Subsonic Speeds," NACA Rpt. 1217, 1955.

56. Crown, J. C., "Calculation of Transonic Flow over Thick Airfoils by Integral Methods," AIAA Journal, Vol. 6, No. 3, 1968, pp. 413-423.

57. Norstrud, H., "Hign Speed Flow Past Wings," NASA Cr-2246, 1973.

58. Nixon, D., "Transonic Flow Around Symmetric Aerofoils at Zero Incidence," Journal of Aircraft, Vol. 11, No. 2, 1974, pp. 122-124.

59. Piers, W. J. and Sloof, J. W., "Calculation of Transonic Flow by Means of a Shock-Capturing Field Panel Method," AIAA Paper 79-1459, 1979.

60. Oskam, B., "Transonic Panel Method for the Full Potential Equation Applied to Multicomponent Airffoils," AIAA Journal, Vol. 23, No. 9, 1985, pp. 1327-1334.

61. Erickson, L. L. and Strande, S. M., "A Theoretical Basis for Extending Surface - Paneling Methods to Transonic Flow," AIAA Journal, Vol. 23, No. 12, 1985, pp. 1860-1867.

62. Erickson, L. L., Madson, M. D. and Wou, A. C., "Application of the TranAir Full-Potential Code to the F-16A," Journal of Aircraft, Vol. 24, No. 8, 1987, pp. 540-545.

63. Sinclair, P. M., "An Exact Integral (Field Panel) Method for the Calculation of Two-Dimensional Transonic Potential Flow around Complex Configurations," Aeronautical Journal, June/July 1986, pp. 227-236.

64. Ogana, W., "Bounday Element Methods in Two-Dimensional Transonic Flows," Boundary Elements IX, Vol. 3: Fluid Flow and Potential Applications, (edited by C.A. Brebbia, W. L. Wendland and G. Kuhu), Computational Mechanics Publications, Springer-Verlag, London, 1987, pp. 567-582.

65. Liepmann, H. W., "The Interaction Between A Boundary Layer and Shock Waves in Transonic Flow," Journal of the Aeronautical Sciences, Vol. 13, 1964, p. 623.

66. Ackeret, J., Feldman, F. and Rott, N., "Investigations on Compression Shocks and Boundary Layers in Fast Moving Gases," E. T. H., Zurich, No. 10, 1946.

67. Pearcey, H. H., Osborne, J. and Haines, A. B., "The Interaction Between Local Effects at the Shock and Rear Separation - A Source of Significant Scale Effect in Wind Tunnel Tests on Aerofoils and Wings," Paper No. 11, Transonic Aerodynamics, AGARD Conference CP-35, Sept. 1968.

68. Yoshihara, H. and Zonnars, D., "The Many Facts of 3-D Transonic Shock-Induced Separation," Paper 42, AGARD Conf. on Flow Separation, CP-168, Gottingen, Germany, May 1975.

69. Collins, D. J. and Krupp, J. A., "Experimental and Theoretical Investigations in Two-Dimensional Transonic Flow," AIAA Journal, Vol. 12, No. 6, 1974, pp. 771-778.

70. Collins, D. J., Private Communication, AEDC TR in preparation, Tullahoma, Tenn., 1976.

71. Studwell, V. E., "Investigation of Transonic Aerodynamic Phenomena for Wing Mouted External Stores," Ph.D Thesis, Univ. of Tenn. Space Institute, 1973, also see Smith, D. K., M.S. Thesis, Univ. of Tenn Space Institute, 1973.

72. Knechtel, Earl D., "Experimental Investigation at Transonic Speeds of Pressure Distributions over Wedge and Circular-Arc Airfoil Sections and Evaluation of Perforated-Wall Interference," NASA TN D-15, 1959.

73. United Aircraft Corp., Sikorsky Aircraft Division, "Two-Dimensional Wind Tunnel Tests of an H-34 Main Rotor Airfoil Section," TRECTR 60-53, 1960.

74. Cahill, J. F., Treon, S. L. and Hofstetter, W. R., "Feasibility of Testing a Large-Chord, Swept-Panel Model to Determine Wing Shock Location at Flight Reynolds Number," AGARD Proceedings No. 83, Paper No. 17, April 1971.

75. Monnerie, B. and Charpin, F., "Essais de Buffeting d'une Aile en Fleche Transsonique," Colloque d'Aerodynamique Applique Lille, November 1973.

76. McDevitt, J. B., Levy, L. L., Jr. and Deiwert, G. S., "Transonic Flow About a Thick Circular-Arc Airfoil," AIAA Journal, Vol. 14, No. 5, 1976, pp. 606-613.

77. Cook, W. J., Presley, L. L. and Chapman, G. T., "Use of Shock Tubes in High Reynolds Number Transonic Testing," Iowa State Univ. Eng. Research Inst., Preprint ERI-75192, 1975.

78. Cook, P. H., McDonald, M. A. and Firmin, M. C. P., "Airfoil RAE2822-Pressure Distributions, and Boundary Layer and Wake Measurements," AGARD AR-138, 1979.

79. Anon., "Experimental Data Base for Computer Program Assessment," AGARD AR-138, May 1979.

80. Harris, C. D., "Two-Dimensional Aerodynamic Characteristics of NACA 0012 Airfoil in the Langley 8-Foot Transonic Pressure Tunnel," NASA TM-81927, April 1981.

81. McCroskey, W. J., Kutler, P. and Bridgeman, J. O., "Status and Prospects of Computational Fluid Dynamics for Unsteady Transonic Viscous Flows," in AGARD CP-374, "Transonic Unsteady Aerodynamics And its Aeroelastic Application," AGARD, January 1985.

82. Ballhaus, W. F. and Lomax, H., "Numerical Solution of Low Frequency Unsteady Transionic Flow Fields," Lecture Notes in Physics, Vol. 35, 1975, pp. 57-63.

83. Tijdeman, H., "Investigations of the Transonic Flow Around Oscillating Airfoils," National Aerospace Laboratory NLR, The Netherlands, NLR TR 77090U, 1978.

84. Ballhaus, W. F. and Steger, J. L., "Implicit-Approximate-Factorization Scheme for the Low Frequency Transonic Equation," NASA TM X-73082, 1975.

85. Ballhaus, W. F. and Goorjiam, P. M., "Implicit Finite-Difference Computations of Unsteady Transonic Flows about Airfoil," AIAA Journal, Vol. 15, No. 12, 1977, pp. 1728-1735.

86. Houwink, R. and van der Vooren, J., "Improved Version of LTRAN2 for Unsteady Transonic Flow Computations," AIAA Journal, Vol. 18, No. 8, 1980, pp. 1008-1010.

87. Couston, M. and Angelin, J. J., "Numerical Solutions of Nonsteady Two-Dimensional Transonic Flows," Journal of Fluids Engineering, Vol. 101, 1979, pp. 341-347.

88. Rizzetta, D. P. and Chin, W. C., "Effect of Frequency in Unsteady Transonic Flow," AIAA Journal, Vol. 17, No. 7, 1979, pp. 779-781.

89. Whitlow, W., Jr., "XTRAN2L: A Program for Solving the General Frequency Unsteady Transonic Small Disturbance Equation," NASA TM 85723, November, 1983.

90. Borland, C. J. and Rizzetta, D. P., "Nonlinear Transonic Flutter Analysis," AIAA Journal, Vol. 20, No. 11, 1982, pp. 1606-1615.

91. Gibbons, M. C., Whitlow, W., Jr. and Williams, M. H., "Nonisentropic Unsteady Three-Dimensional Small Disturbance Potential Theory," NASA TM 87226, 1986.

92. Edwards, J. W., Bland, S. R. and Seidel, D. A., "Experience with Transonic Unsteady Aerodynamic Calculations," in AGARD CP-374, "Transonic Unsteady Aerodynamics and its Aeroelastic Application," AGARD, January 1985.

93. Bland, S. R. and Seidel, D. A., "Calculation of Unsteady Aerodynamics for Four AGARD Standard Aeroelastic Configurations," NASA TM 85817, May 1984.

94. Goorjian, P. M. and Guruswamy, G. P., "Unsteady Transonic Aerodynamic and Aeroelastic Calculations about Airfoils and Wings," in AGARD CP-374, "Transonic Unsteady Aerodynamics and its Aeroelastic Apploication," AGARD, January 1985.

95. Malone, J. B., Ruo, S. Y. and Sankar, N. L., "Computation of Unsteady Transonic Flows about Two-Dimensional and Three-Dimensional AGARD Standard Configurations," in AGARD CP-374, "Transonic Unsteady Aerodynamics and its Aeroelastic Application," AGARD, January 1985.

96. Edwards, J. W., "Applications of Potential Theory Computations to Transonic Aeroelasticity," Paper No. ICAS-86-2.9.1, Fifteenth Congress of the International Council of the Aeronautical Sciences, London, England, September 1986.

97. Isogai, K., "Calculation of Unsteady Transonic Flow Using the Full Potential Equation," AIAA Paper 77-448, 1977.

98. Chipman, R. and Jameson, A., "Fully Conservative Numerical Solutions for Unsteady Irrotational Transonic Flow about Airfoils," AIAA Paper 79-1555, 1979.

99. Goorjian, P. M., "Implicit Computation of Unsteady Transonic Flow Governed by the Full Potential Equation in Conservative Form," AIAA Paper 80-150, Jan. 1980.

100. Chipman, R. and Jameson, A., "An Alternating-Direction-Immplicit Algorithm for Unsteady Potential Flow," AIAA Paper 81-0329, 1981.

101. Magnus, R. and Yoshihara, H., "The Transonic Oscillating Flap," AIAA Paper 76-327, presented at the AIAA 9th Fluid and Plasma Dynamics Conference, San Diego, California, July 14-16, 1976.

102. Magnus, R. J., "Calculations of Some Unsteady Transonic Flows about the NACA 64A006 and 64A010 Airfoils," Technical Report AFFDL-TR-77-46, July 1977.

103. Magnus, R. J., "Some Numerical Solutions of Inviscid, Unsteady, Transonic Flows Over the NLR 7301 Airfoil," CASD/LVP 78-013, Convair Division of General Dynamics, San Diego, California, January 1978.

104. Chyu, W. J., Davis, S. S. and Chang, K. S., "Calculation of Unstady Transonic Flows over an Airfoil," AIAA Paper 79-1554R, 1979.

105. Kandil, O. A. and Chuang, H. A., "Unsteady Vortex-Dominated Flows around Maneuvering Wings over a Wide Range of Mach Numbers," AIAA Paper 88-0371, 1988.

106. Kandil, O. A. and Chuang, H. A., "Unstaedy Transonic Airfoil Computation Using Implicit Euler Scheme on Body-Fixed Grid," presented in Southeastern Conference on Theoretical and Applied Mechanics, SECTAM XIV, April 18-19, 1988, Biloxi, Mississippi.

107. Kandil, O. A. and Chuang, H. A., "Computation of Steady and Unsteady Vortex-Dominated Flows," AIAA Paper 87-1462, 1987.

108. Anderson, W., Thomas, J. and Rumsey, C., "Extension and Applications of Flux-Vector Spliting to Unsteady Calculations on Dynamic Meshes," AIAA Paper 87-1152-CP, 1987.

109. Smith, G. E., Whitlow, W., Jr. and Hassan, H. A., "Unsteady Transonic Flows Past Airfoils Using the Euler Equations," AIAA Paper 86-1764-CP, 1986.

110. Salmond, D. J., "Calculation of Harmonic Aerodynamic Forces on Arofoils and Wings from the Euler Equations," in AGARD CP-374,"Transonic Unsteady Aerodynamics and its Aeroelastic Application," AGARD, January 1985.

111. Jameson, A. and Baker, T. J., "Multigrid Solutions of the Euler Equations for Aircraft Configurations," AIAA Paper 84-0093, 1984.

112. Holst, T. L., Kaynak, U., Gundy, K. L., Thomas, S. D. and Flores, J., "Numerical Solution of Transonic Wing Flow Fields Using an Euler/Navier-Stokes Zonal Approach," AIAA Paper 85-1640, 1985.

113. Sankar, L. N., Malone, J. B. and Schuster, D., "Full Potential and Euler Solutions for the Unsteady Transonic Flow Past a Fighter Wing," AIAA Paper 85-4061, 1985.

114. Edwards, J. W. and Thomas, J. L., "Computational Methods for Unsteady Transonic Flows," AIAA Paper 86-0107, 1986.

115. Rumsey, C. L. and Anderson, W. K., "Some Numerical and Physical aspects of Unsteady Navier-Stokes Computations Over Airfoils Using Dynamic Meshes," AIAA Paper 88-0329, 1988.

116. Nixon, D., "Calculation of Unsteady Transonic Flows Using the Integral Equation Method," AIAA Journal, Vol. 16, No. 9, 1978, pp. 976-983.

117. Hounjet, M. H. L., "Transonic Panel Method to Determine Loads on Oscillating Airfoils with Shocks," AIAA Journal, Vol. 19, No. 5, 1981, pp. 559-566.

118. Tseng, K. and Morino, L., "Nonlinear Green's Function Methods for Unstady Transonic Flows," in Transonic Aerodynamics, Edited by D. Nixon, AIAA, New York, 1982, pp. 565-603.

119. Hounjet, M. H. L., "A Field Panel / Finite Difference Method for Potential Unsteady Transonic Flow," AIAA Journal, Vol. 23, No. 4, 1985, pp. 537-545.

120. Erickson, A. L. and Robinson, R. C., "Some Preliminary Results in the Determination of Aerodynamic Derivatives of Control Surfaces in the Transonic Speed Range by means of a Flush Type Electrical Pressure Cell," NACA RM A8H03, 1948.

121. Lessing, H. C., Troutman, J. L. and Meness,G. P., "Experimental Determination of the Pressure Distribution on a Rectangular Wing Oscillating in the First Bending Mode for Mach Numbers from 0.24 to 1.30," NASA TN-D344, 1960.

122. Leadbetter, S. A., Clevenson, S. A. and Igoe, W. B., "Experimental Investigation of Oscillatory Aerodynamic Forces, Moments and Pressures Acting on a Tapered Wing Oscillating in Pitch at Mach Numbers from 0.40 to 1.07," NASA TN-D1236, 1960.

123. Tijdeman, H. and Zwaan, R. J., "On the Prediction of Aerodynamic Loads on Oscillating Wings in Transonic Flow," NLR MP 73026U, Nat'l. Aerosp. Lab., Netherlands, 1963.

124. Tijdeman, H. and Bergh, H., "Analysis of Pressure Distributions Measured on a Wing with Oscillating Control Surface in Two-Dimensional High Subsonic and Transonic Flow," NLR-TR F.253, 1967.

125. Tijdeman, H. and Schippers, P., "Results of Pressure Measurements on an Airfoil with Oscillating Flap in Two-Dimensional High Subsonic and Transonic Flow (Zero Incidence and Zero Mean Flap Position)," NLR TR 73078 U, 1973.

126. Destuynder, R. and Tijdeman, H., "An Investigation of Different Techniques for Unsteady Pressure Measurements in Compressible Flow and Comparison with Results of Lifting Surface Theory," NLR MP 73031U, Nat'l Aero. Lab., Netherlands, 1974.

127. Tijdeman, H., "On the Motion of Shock Waves on an Airfoil with Oscillating Flap in Two-Dimensional Transonic Flow," NLR TR 75038U, Netherlands, 1975, also Symposium Transsonicum, II, Springer-Verlag, 1976.

128. Tijdeman, H., "On the Unsteady Aerodynamic Characteristics of Oscillating Airfoils in Two-Dimensional Transonic Flow," NLR-MP 76003, U, 1976.

129. Tijdeman, H., "Investingations of the Transonic Flow Around Oscillating Airfoils," Doctoral Thesis, Technische Hogeschool Delft, The Netherlands, 1977.

130. Grenon, R. and Thers, J., "Etude d'un profil supercritique avec gouverne oscillante en ecoulement subsonique et transsonique," AGARD CP-227, 1972.

131. Davis, S. and Malcolm, G., "Experimental Unsteady Aerodynamics of Conventional and Supercritical Airfoils," NASA TM 81221, August 1980.

132. Landon, R. H., "NACA 0012. Oscillatory and Transient Pitching," Compendium of Unsteady Aerodynamic Measurements, AGARD Report No. 702, August 1982.

133. Tijdeman, H., "Investigations of the Transonic Flow around Oscillating Airfoils," NLR TR 77090 U, 1977.

134. Hess, R. W., Seidel, D. A., Igoe, W. B. and Lawing P. L., "Highlights of Unsteady Pressure Tests on a 14 Percent Supercritical Airfoil at High Reynolds Number, Transonic Condition," NASA TM 89080, 1987.

135. Tijdeman, H., Van Nunen, J. W. Gl, Kraan, A. N., Persoon, A. J., Poestkoke, R., Roos, R., Schippers, P. and Sieber, C. M., "Transonic Wind Tunnel Tests on an Oscillating Wing with External Stores," AFFDL-TR-78-194, December 1978.

136. Horsten, J. J., den Boer, R. G. and Zwaan, R. J., "Unsteady Transonic Pressure Measurements on a Semi-Span Wind-Tunnel Model of a Transport-Type Supercritical Wing (LANN Model)," NLR TR 82069 U, Parts I and II, July 1982.

137. Mabey, D. G., Welsh, B. L. and Cripps, B. E., "Measurements of Steady and Oscillatory Pressures on a Low Aspect Ratio Model at Subsonic and Supersonic Speeds," British RAE Technical Report 84095, September 1984.

138. Moulden, T. H., Fundamentals of Transonic Flow, John Wiley & Sons, New York, 1984.

139. Kraus, Werner, "Panel Methods in Aerodynamics," in Numerical Methods in Fluid Dynamics, edited by H. J. Wirz and J. J. Smolderen, Hemisphere Publishing Corporation, Washington-London, 1978, pp. 237-297.

140. Bland, S. R., "AGARD Two-Dimensional Aeroelastic Configurations," AGARD-AR-156, Aug. 1979.

141. Abbott, I. H. and von Doenhoff, A. E., Theory of Wing Sections, Dover Publications, Inc., New York, 1959, p. 321.

142. Kuethe, Arnold M. and Chow, Chuen-Yen, Foundations of Aerodynamics: Bases of Aerodynamic Design, third edition, John Wiley & Sons, New York, 1976, p. 124.

143. Sells, C. L., "Plane Subcritical Flow Past a Lifting Airfoil," Proceedings of the Royal Society, London, No. 308 (Series A), 1968, pp. 377-401.

144. Garabedian, P., Korn, D. G. and Jameson, A.,"Supercritical Wing Sections," Lecture Notes in Econcomic and Mathematical Systems, Vol. 66, 1972.

145. Hafez, M., "Perturbation of Transonic Flow with Shocks," Numerical And Physical Aspects of Aerodynamic Flows, edited by Tuncer Cebeci, Springer-Verlag, New York, Heidelberg Berlin, 1982, pp. 421-438.

146. Hall, M. G., "Transonic Flows," IMA, Controller, HMSO, London, 1975.

147. Steger, J. L., "Implicit Finite-Difference Simulation of Flow about Arbitrary Two-Dimensional Geometries," AIAA Journal, Vol. 16, No. 7, 1978, pp. 679-686.

148. Lee, K. D., Dickson, L. J., Chen, A. W. and Rubbert, P. E., "An Improved Matching Method for Transonic Computations," AIAA Paper 78-1116, 1978.

149. Kandil, Osama A. and Hu, Hong, "Integral Equation Solution for Transonic and Subsonic Aerodynamics," presented in The Third GAMM-Seminar on Panel Methods in Mechanics, January 16-18, 1987, Kiel, F.R.G. Also published in Notes on Numerical Fluid Mechanics, Springer-Verlag, 1987.

150. Kandil, Osama A., Chuang, Andrew and Hu, Hong, "Solution of Transonic-Vortex Flow using Finite-Volume Euler and Full-Potential Integral Equations," presented in Symposium on Transonic Unsteady Aerodynamics and Aeroelasticity - 1987, NASA-Langley Research Center, Hampton, Virginia.

151. Kandil, Osama A. and Hu, Hong, "Transonic Airfoil Computation Using the Integral Equation with and without Embedded Euler Domains," Boundary Elements IX Vol. 3: Fluid Flow and Potential Applications, edited by C. A. Brebbia, W. L. Wendland and G. Kuhn, Computational Mechanics Publications, Springer-Verlag, 1987, pp. 553-566.

152. Kandil, Osama A. and Hu, Hong, "Full-Potential Integral Solution for Transonic Flows with and without Embedded Euler Domains," AIAA Paper 87-1461, 1987. Also to appear in AIAA Journal, Vol. 26, No. 8, 1988.

153. Kandil, Osama A. and Hu, Hong, "Unsteady Transonic Airfoil Computations Using the Integral Solution of Full-Potential Equation," will present in Computational Mechanics Institute 10th International Conference: Boundary Element Methods in Engineering, Sept. 6-8, 1988, Southampton, UK. Also published in Boundary Elements X, Computational Mechanics Publications, Springer-Verlag, 1988.

APPENDIX A

SURFACE INTEGRALS

After the linear surface source or vortex distribution, given by Eq. (4.2a) or Eq. (4.2b), or the constant shock panel source is substituted into the corresponding integral terms in Eqs. (4.1), (4.21) and (5.1), the four integrals are obtained in the local coordinates ξ and η as follows:

$$I_1(\bar{x},\bar{y}) = \int_0^{l_k} \frac{\bar{y}}{(\bar{x}-\xi)^2+\bar{y}^2} d\xi \tag{A.1}$$

$$I_2(\bar{x},\bar{y}) = \int_0^{l_k} \frac{\bar{y}\xi}{(\bar{x}-\xi)^2+\bar{y}^2} d\xi \tag{A.2}$$

$$I_3(\bar{x},\bar{y}) = \int_0^{l_k} \frac{\bar{x}-\xi}{(\bar{x}-\xi)^2+\bar{y}^2} d\xi \tag{A.3}$$

$$I_4(\bar{x},\bar{y}) = \int_0^{l_k} \frac{\xi(\bar{x}-\xi)}{(\bar{x}-\xi)^2+\bar{y}^2} d\xi \tag{A.4}$$

The closed form expressions of these four integrals are given by

$$I_1(\bar{x},\bar{y}) = \tan^{-1}\left(\frac{\bar{x}}{\bar{y}}\right)^2 - \tan^{-1}\left(\frac{\bar{x}-l_k}{\bar{y}}\right)^2 \tag{A.1a}$$

$$I_2(\bar{x},\bar{y}) = \frac{\bar{y}}{2}\ln\left[\frac{(\bar{x}-l_k)^2+\bar{y}^2}{\bar{x}^2+\bar{y}^2}\right] + \bar{x}I_1(\bar{x},\bar{y}) \tag{A.2a}$$

$$I_3(\bar{x},\bar{y}) = -\frac{1}{2}\ln\left[\frac{(\bar{x}-l_k)^2+\bar{y}^2}{\bar{x}^2+\bar{y}^2}\right] \tag{A.3a}$$

$$I_4(\bar{x},\bar{y}) = -l_k + \bar{y}I_1(\bar{x},\bar{y}) + \bar{x}I_3(\bar{x},\bar{y}) \tag{A.4a}$$

where $(\bar{x},\bar{y})$ is the receiver point measured in the local coordinates ξ and η, and l_k is the source or vortex panel length ($l_k = \xi_{k+1} - \xi_k$).

When the receiver point $(\bar{x}, \bar{y})$ is on the panel surface itself ($\bar{y} = 0$, but $\bar{x} \neq 0$ or l_k), then the integrals given by Eqs. (A.1) through (A.4) become singular integrals. The results of these singular integrals are given by

$$I_1(\bar{x}, \bar{y}) = \pi \tag{A.1b}$$

$$I_2(\bar{x}, \bar{y}) = \bar{x}\pi \tag{A.2b}$$

$$I_3(\bar{x}, \bar{y}) = \ln\left(\frac{\bar{x}}{l_k - \bar{x}}\right) \tag{A.3b}$$

$$I_4(\bar{x}, \bar{y}) = -l_k + \bar{x}\ln\left[\frac{\bar{x}}{l_k - \bar{x}}\right] \tag{A.4b}$$

APPENDIX B

FIELD INTEGRALS

The integrals of compressibilities, G, G_1 and G_2, are double integrals which are evaluated over rectangular and trapezoidal elements. Constant distributions of G, G_1 and G_2 are used over each element.

B.1 Rectangular Elements

The integrals are given by

$$I_5(x,y) = \int_c^d \int_a^b \frac{x-\xi}{(x-\xi)^2+(y-\eta)^2} d\xi d\eta \qquad (B.1)$$

$$I_6(x,y) = \int_c^d \int_a^b \frac{y-\eta}{(x-\xi)^2+(y-\eta)^2} d\xi d\eta \qquad (B.2)$$

The corresponding results are given by

$$I_5(x,y) = I_{5,1}(b,d) - I_{5,1}(a,d) - I_{5,1}(b,c) + I_{5,1}(a,c) \qquad (B.1a)$$

$$I_6(x,y) = I_{6,1}(b,d) - I_{6,1}(a,d) - I_{6,1}(b,c) + I_{6,1}(a,c) \qquad (B.2a)$$

where

$$I_{5,1}(\xi,\eta) = (x-\xi)\tan^{-1}\left(\frac{y-\eta}{x-\xi}\right) + \frac{(y-\eta)}{2}\ln\left[\left(\frac{x-\xi}{y-\eta}\right)^2 + 1\right] \qquad (B.1b)$$

$$I_{6,1}(\xi,\eta) = (y-\eta)\tan^{-1}\left(\frac{x-\xi}{y-\eta}\right) + \frac{(x-\xi)}{2}\ln\left[\left(\frac{y-\eta}{x-\xi}\right)^2 + 1\right] \qquad (B.2b)$$

where (x,y) is the receiver point measured in the global coordinates x and y.

B.2 Trapezoidal Elements

The integrals are given by

$$I_7(x,y) = \int_a^b \int_{A+B\xi}^d \frac{x-\xi}{(x-\xi)^2+(y-\eta)^2} d\eta d\xi \qquad (B.3)$$

$$I_8(x,y) = \int_a^b \int_{A+B\xi}^d \frac{y-\eta}{(x-\xi)^2+(y-\eta)^2} d\eta d\xi \qquad (B.4)$$

The corresponding results are given by

$$I_7(x,y) = I_{5,1}(b,d) - I_{5,1}(a,d) - I_{7,1}(b) + I_{7,1}(a) \qquad (B.3a)$$

$$I_8(x,y) = I_{8,1}(b) - I_{8,1}(a) - I_{8,2}(b) + I_{8,2}(a) \qquad (B.4a)$$

where

$$\begin{aligned} I_{7,1}(\xi) = &-\xi\tan^{-1}\left(\frac{y-A-B\xi}{x-\xi}\right) \\ &+ \frac{E}{2E_1}\ln(E_1\xi^2 + E_2\xi + E_3) \\ &- \frac{EE_2}{2E_1} I_{it}(E_1,E_2,E_3) \end{aligned} \qquad (B.3b)$$

$$\begin{aligned} I_{8,1}(\xi) = &-\frac{1}{2}\left(\xi + \frac{F_2}{2F_1}\right)\ln(F_1\xi^2 + F_2\xi + F_3) + \xi \\ &+ \frac{F_2^2 - 4F_1F_3}{2F_1} I_{it}(F_1,F_2,F_3) \end{aligned} \qquad (B.4b)$$

$$\begin{aligned} I_{8,2}(\xi) = &-\frac{1}{2}\left(\xi - \frac{H_2}{2H_1}\right)\ln(H_1\xi^2 + H_2\xi + H_3) \\ &+ \xi + \frac{H_2^2 - 4H_1H_3}{2H_1} I_{it}(H_1,H_2,H_3) \end{aligned} \qquad (B.4c)$$

and

$$E_1 = 1 + B^2$$

$$E_2 = -2x - 2B(y - A)$$

$$E_3 = x^2 + (y - A)^2 \qquad (B.3c)$$

$$E = -(A + Bx) + y$$

$$F_1 = 1$$

$$F_2 = -2x \qquad (B.4d)$$

$$F_3 = x^2 + (y - d)^2$$

$$H_1 = E_1$$

$$H_2 = E_2 \qquad (B.4e)$$

$$H_3 = E_3$$

$$I_{it}(X_1, X_2, X_3) \equiv \int \frac{1}{X_1\xi^2 + X_2\xi + X_3} d\xi \qquad (B.3d)$$

The result of I_{it} is given by:

For $D \equiv X_2^2 - 4X_1X_3 < 0$:

$$I_{it}(X_1, X_2, X_3) = \frac{2}{\sqrt{-D}} \tan^{-1}\left[\frac{2X_1\xi + X_2}{\sqrt{-D}}\right] \qquad (B.3e)$$

For $D > 0$:

$$I_{it}(X_1, X_2, X_3) = \frac{1}{\sqrt{D}} \ln\left(\frac{2X_1\xi + X_2 - \sqrt{D}}{2X_1\xi + X_2 + \sqrt{D}}\right) \qquad (B.3f)$$

For $D = 0$:

$$I_{it}(X_1, X_2, X_3) = -\frac{2}{2X_1\xi + X_2} \qquad (B.3g)$$

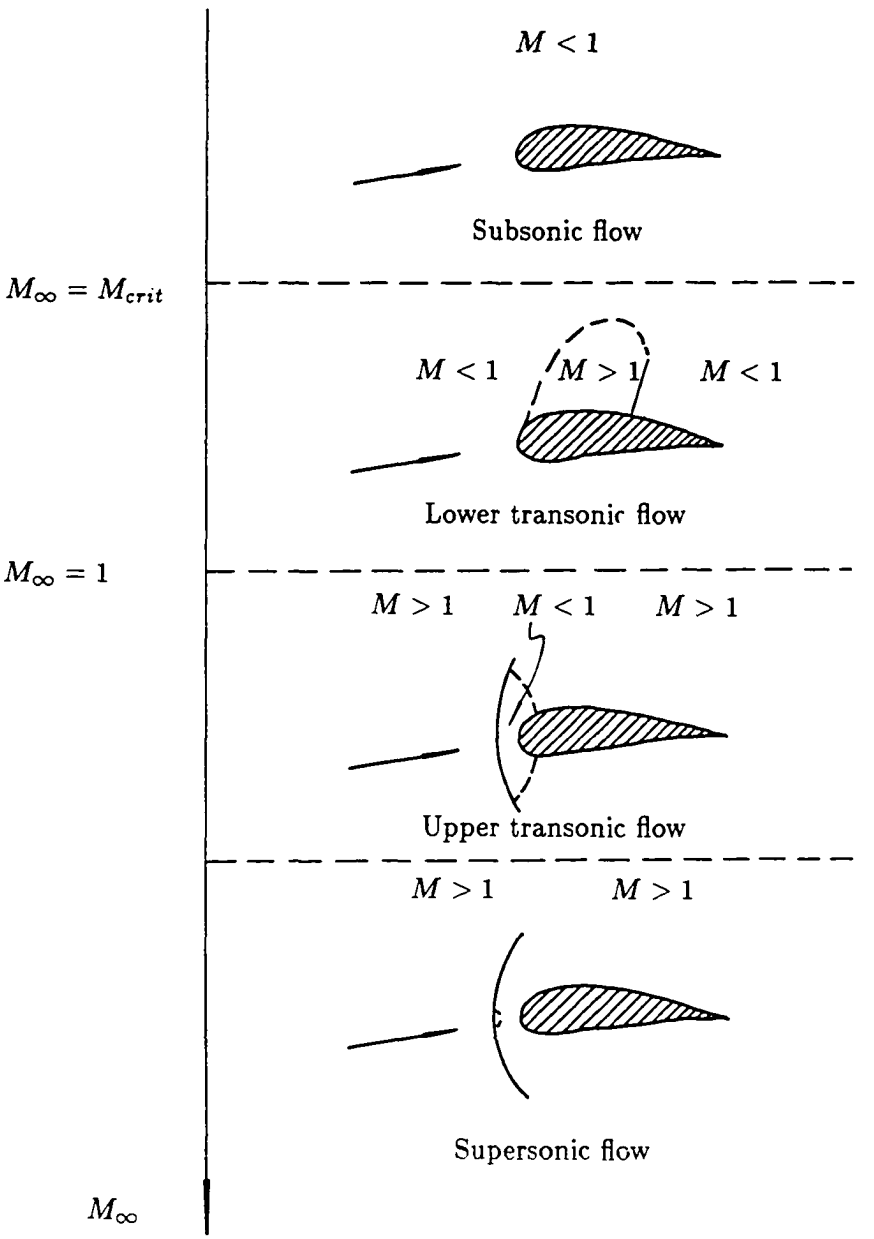

Fig. 2.1 Classification of the flow.

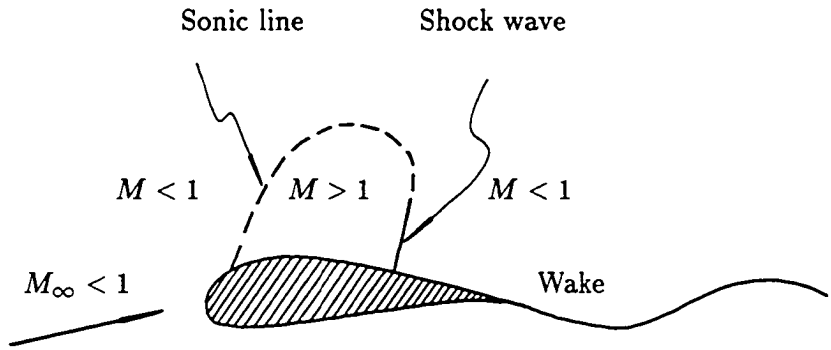

Fig. 2.2 Sketch of a typical transonic flow.

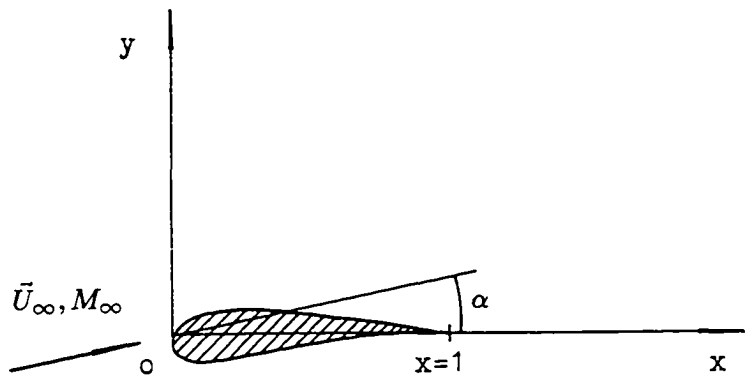

Physical parameters:

Free-stream velocity	$\vec{U}_\infty$
Free-stream Mach no.	$M_\infty = U_\infty / a_\infty$
Angle of attack	α
Space-fixed coordinates	x, y

Fig. 3.1 Physical problem and coordinate system for steady flows.

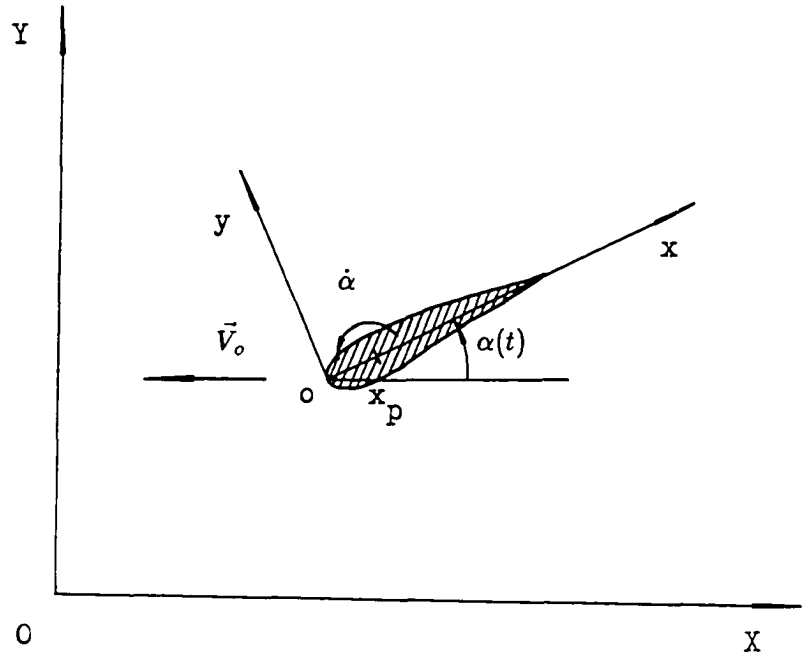

Physical parameters:

Space-fixed coordinates	X, Y
Body-fixed coordinates	x, y
Translation velocity	$\vec{V}_o$
Angle of attack	$\alpha(t) = \alpha_o + \alpha_a \sin(k_c t)$
Angular velocity	$\dot{\alpha}\vec{k} = \frac{d\alpha}{dt}\vec{k}$
Pivot point of pitching oscillation	x_p

Fig. 3.2 Physical problem and coordinate system for unsteady flows.

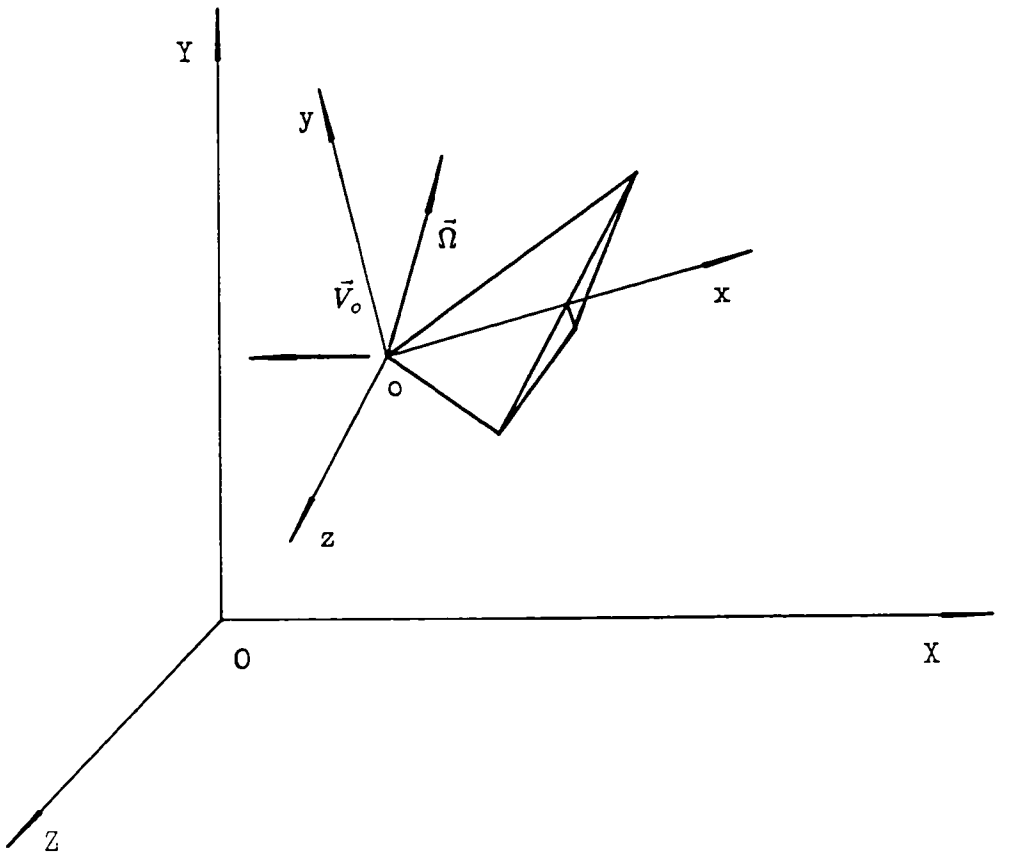

Physical parameters:

Space-fixed coordinates	X, Y, Z
Body-fixed coordinates	x, y, z
Translation velocity	$\vec{V}_o$
Angular velocity	$\vec{\Omega}$

Fig. 3.3 Space-fixed and body-fixed frames of reference.

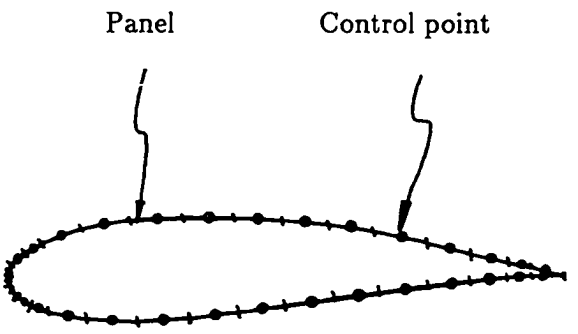

Fig. 4.1 Airfoil surface paneling.

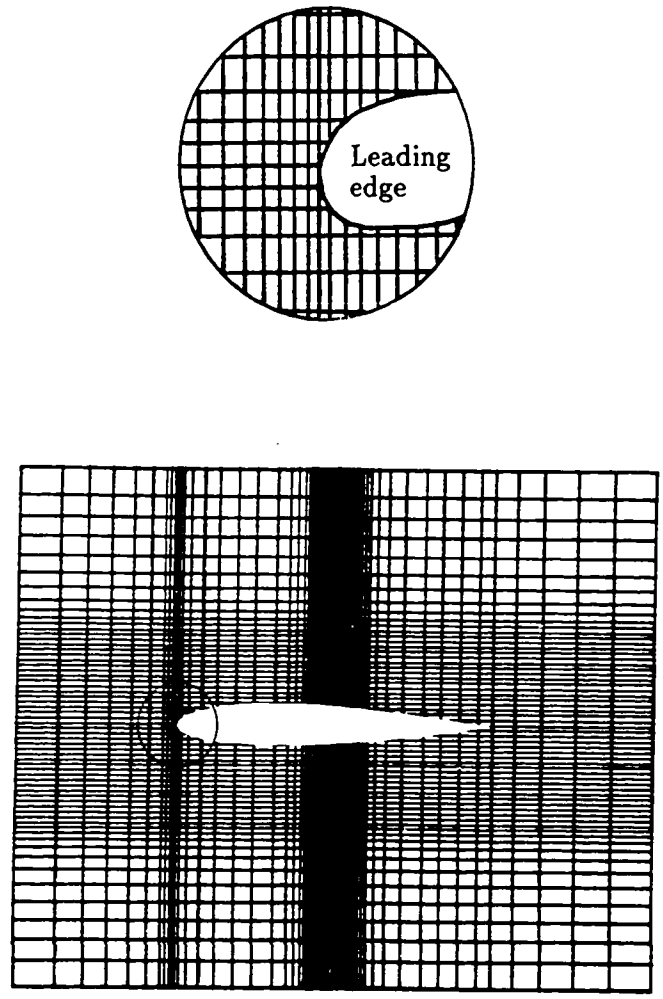

Fig. 4.2 Computational domain and field-elements.

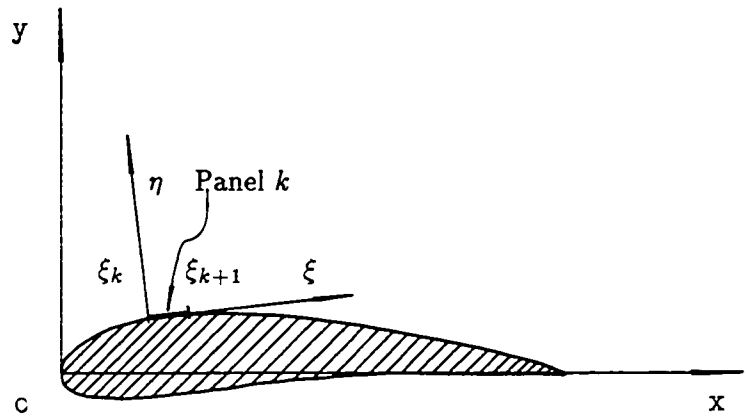

x, y : Global coordinate

ξ, η: Local coordinate for each panel

Fig. 4.3 Relation between global and local coordinates.

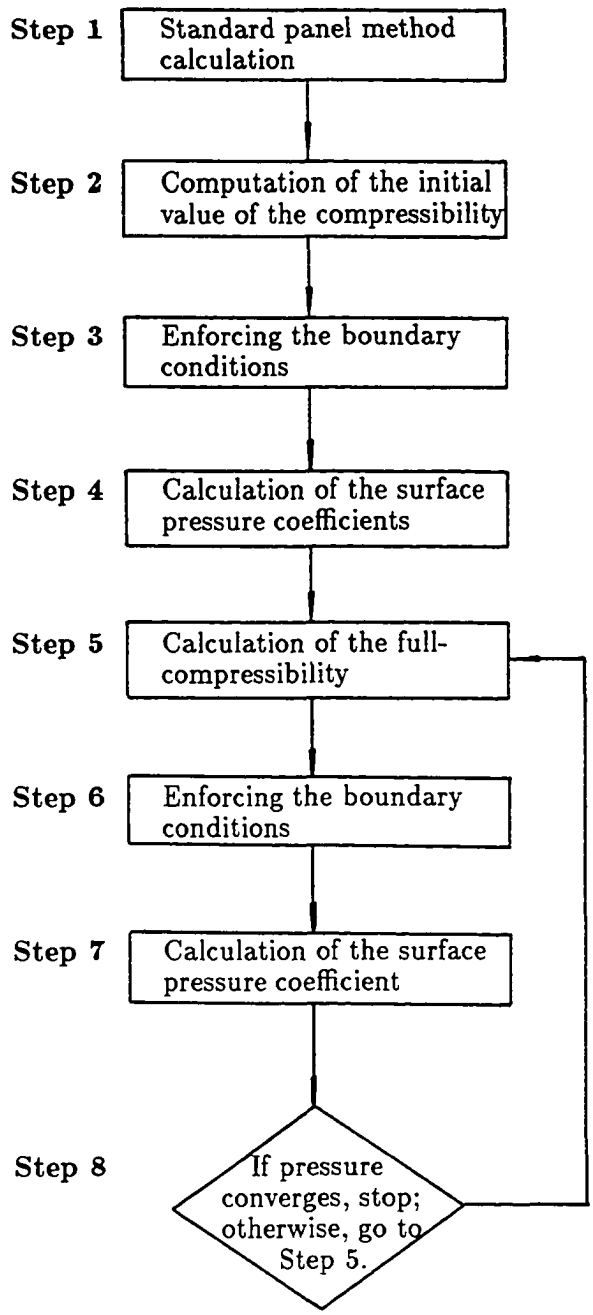

Fig. 4.4 Computational steps for shock-free flows.

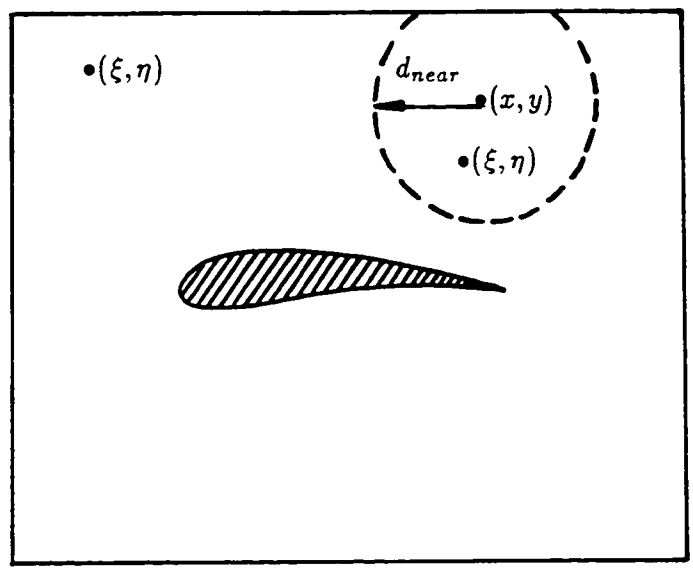

If the sender point (ξ, η) is inside the circle with the center at the receiver point (x, y) and radius of d_{near}, Eq. (4.11) is used; otherwise, Eq. (4.13) is used.

Fig. 4.5 Near-field vs. far-field computations.

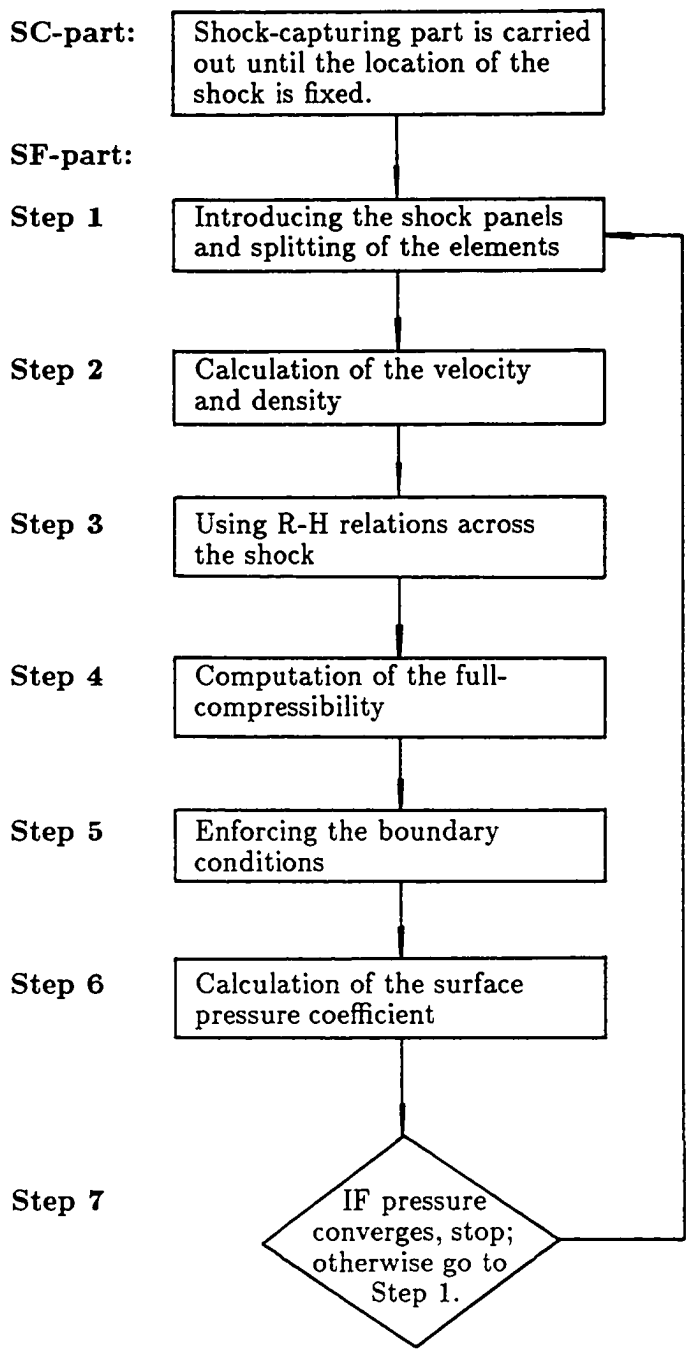

Fig. 4.6 Computational steps of the IE-SCSF scheme.

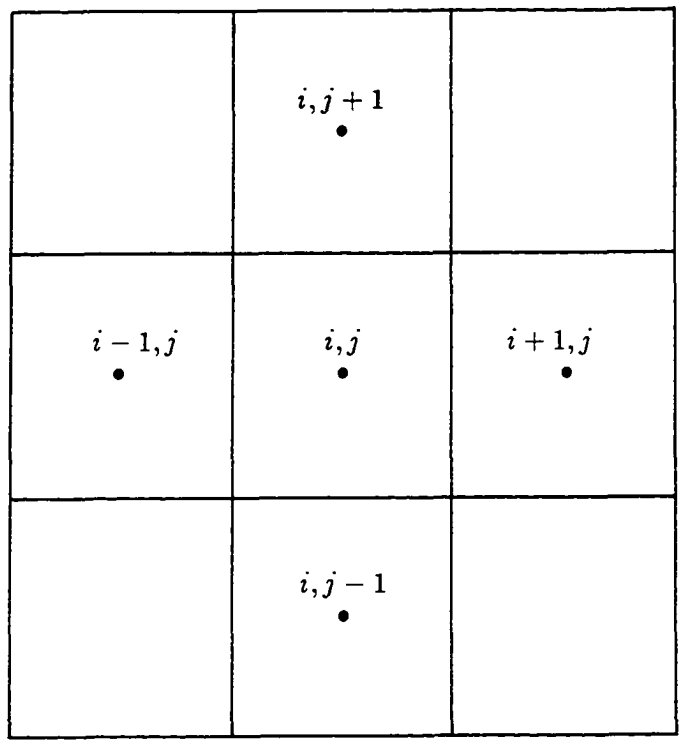

Fig. 4.7 Index used in difference scheme.

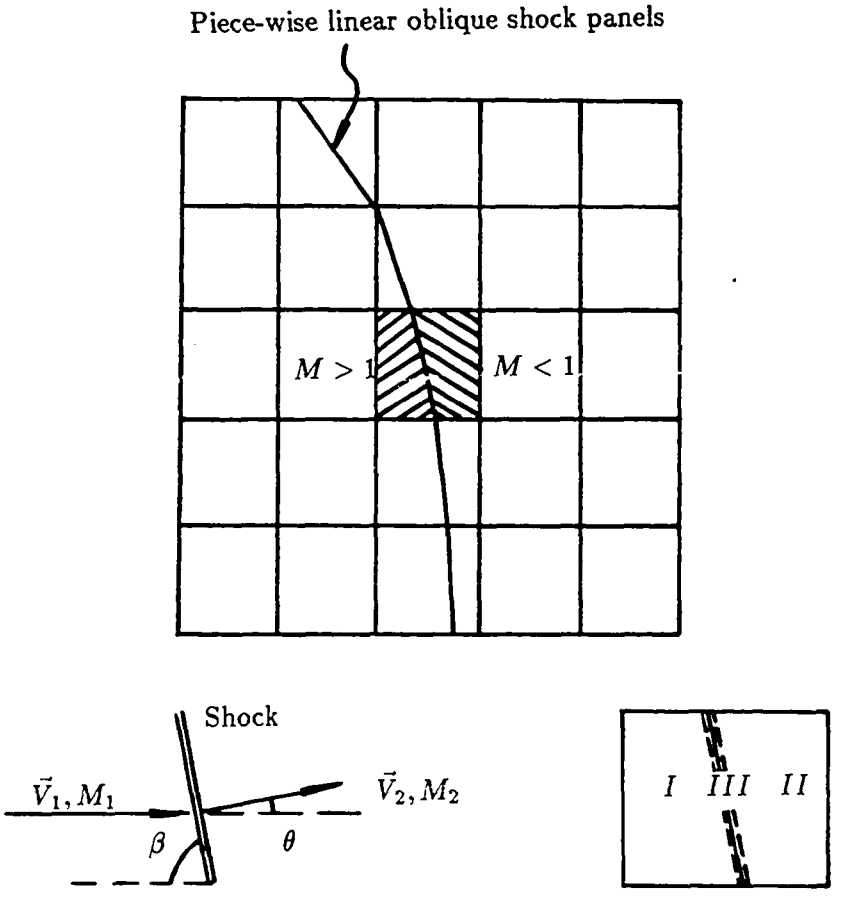

Areas I and II: Third integral of Eq. (4.21)

Area III: Fourth integral of Eq. (4.21)

Fig. 4.8 Illustration of shock panels and field-element splitting.

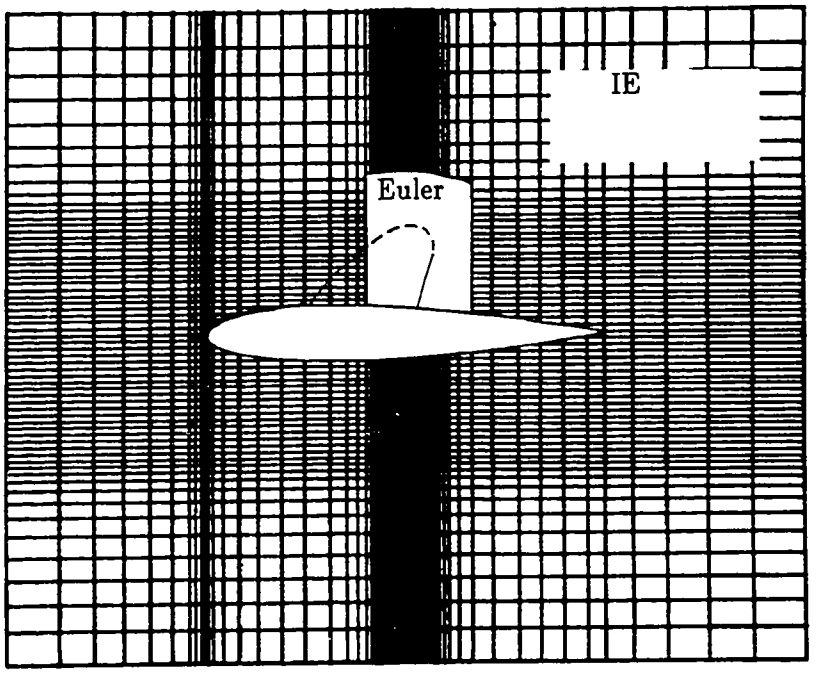

Fig. 4.9 Computational region of the IE with embedded Euler domain.

Step 1
The IE-SC scheme is carried out
until the shock location is fixed.

Step 2
With B.C.s and I.C. obtained from
Step 1, Euler equations are solved
in the small embedded Euler domain.

Step 3
One IE-SC iteration is taken in the
IE-domain outside the Euler domain to
update the B.C.s for the Euler domain.

Step 4
With the B.C.s obtained in Step 3 and the I.C.
obtained in Step 2, Euler equations
are solved in the Euler domain.

Step 5
Repeat Steps 3 and 4 until the
solution converges.

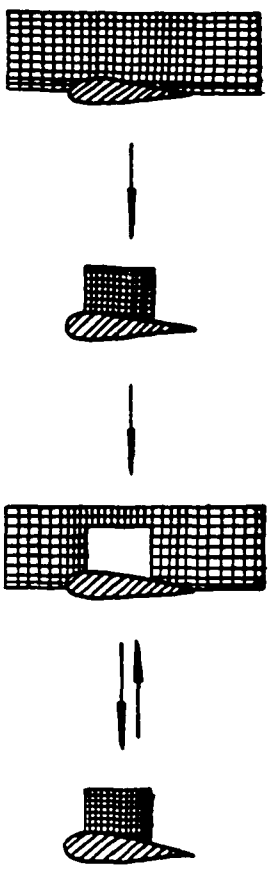

Fig. 4.10 Computational steps of the IE-EE scheme.

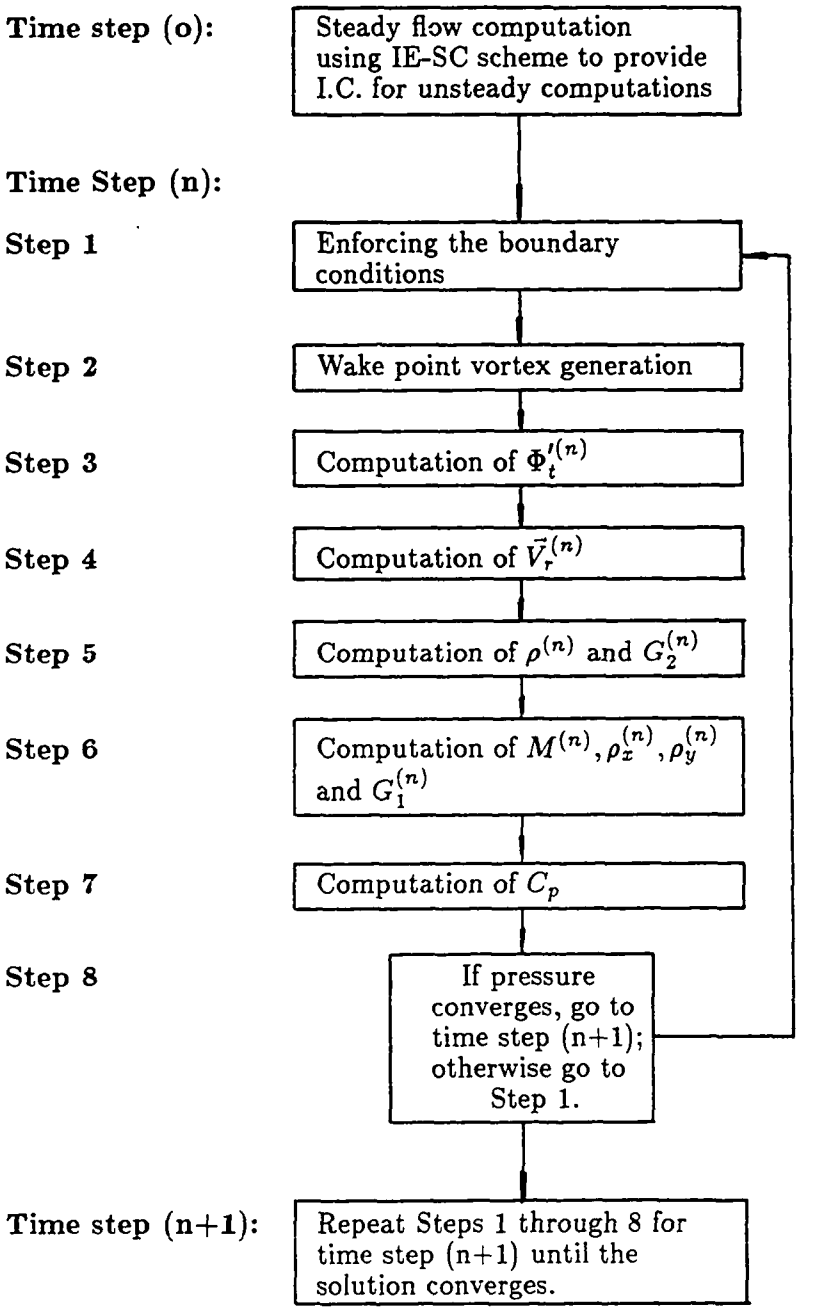

Fig. 5.1 Computational steps of the unsteady IE-SC scheme.

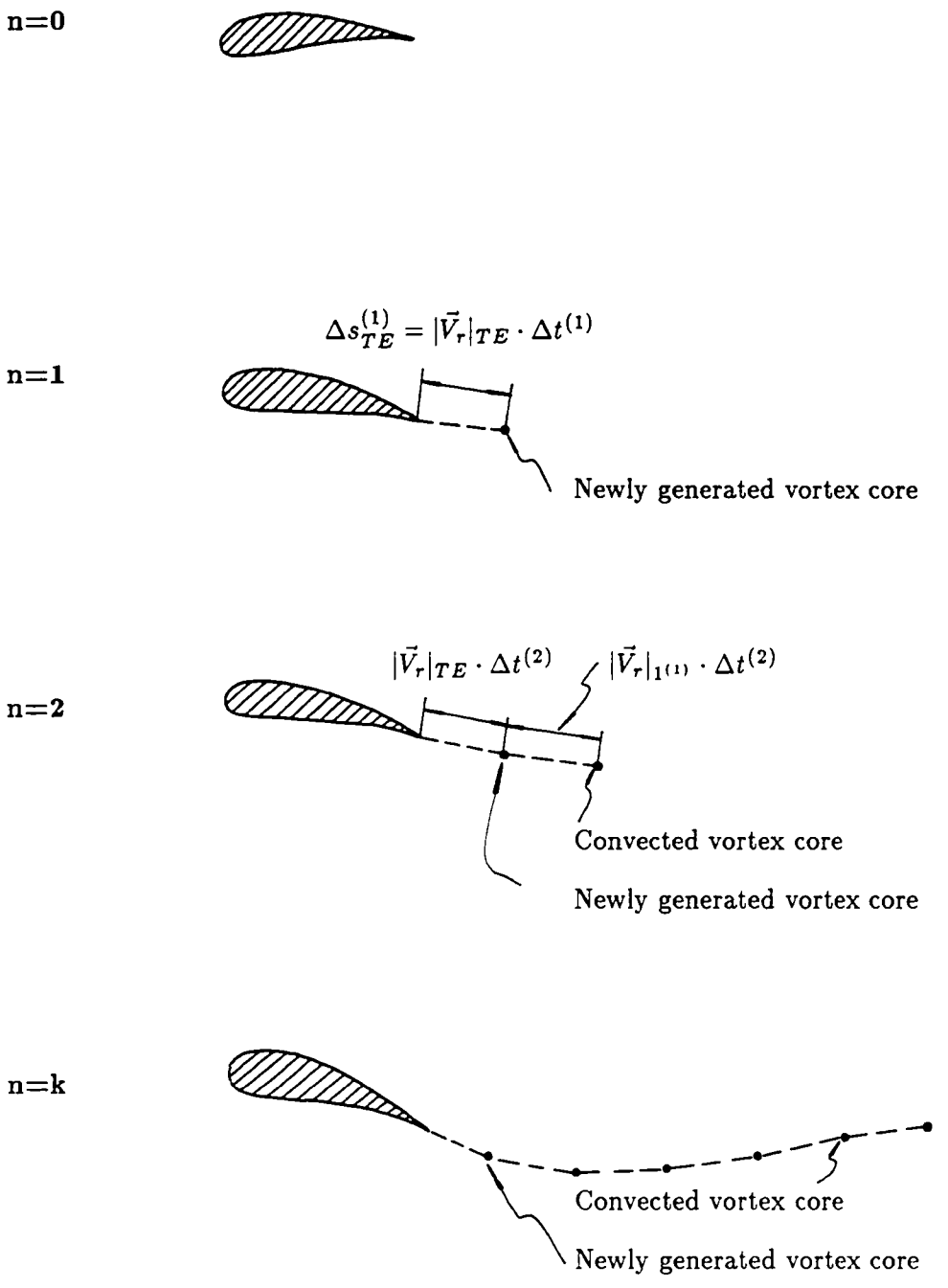

Fig. 5.2 Wake point vortex generation.

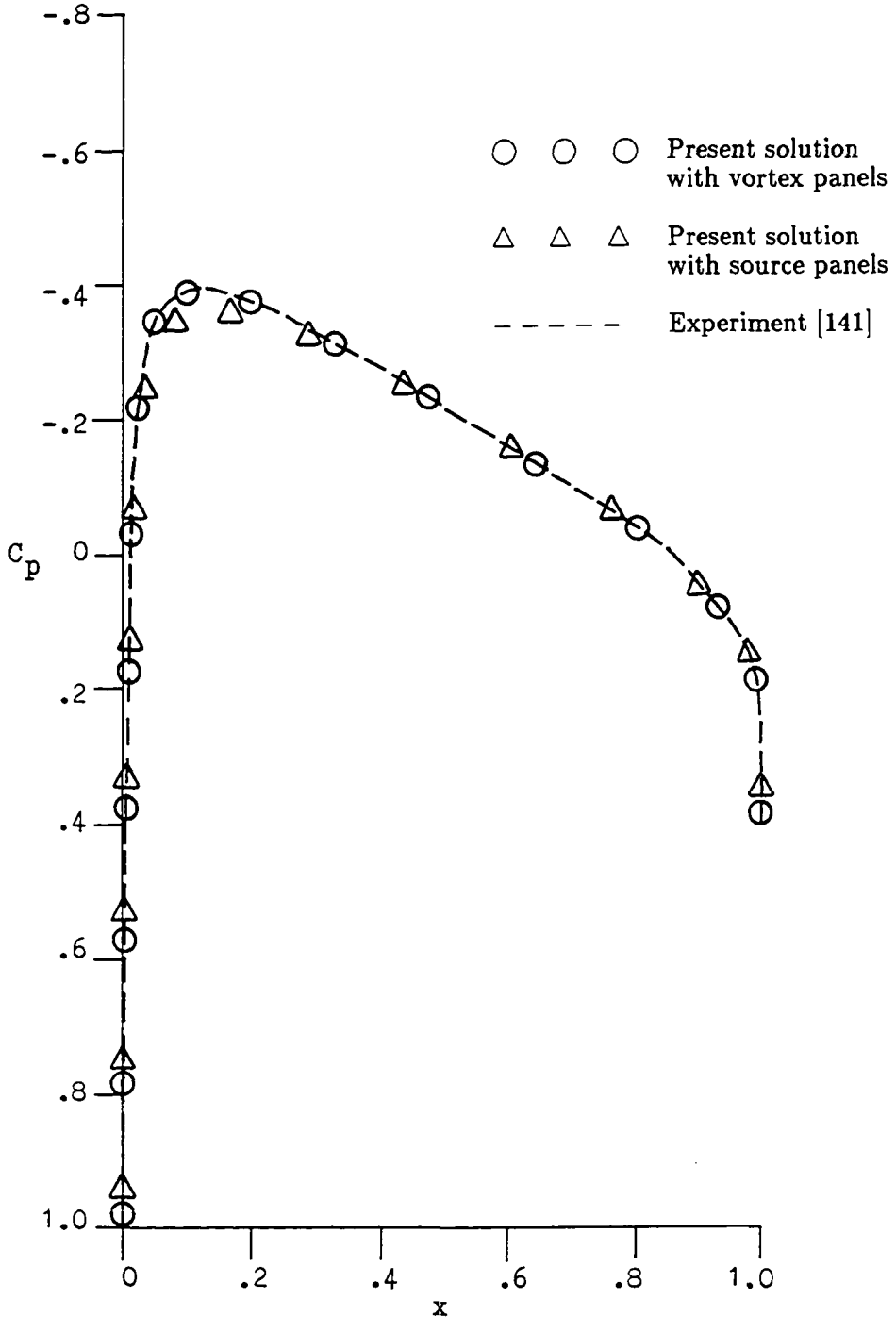

Fig. 6.1 Vortex vs. source panels, NACA 0012, $M_\infty = 0, \alpha = 0^o$.

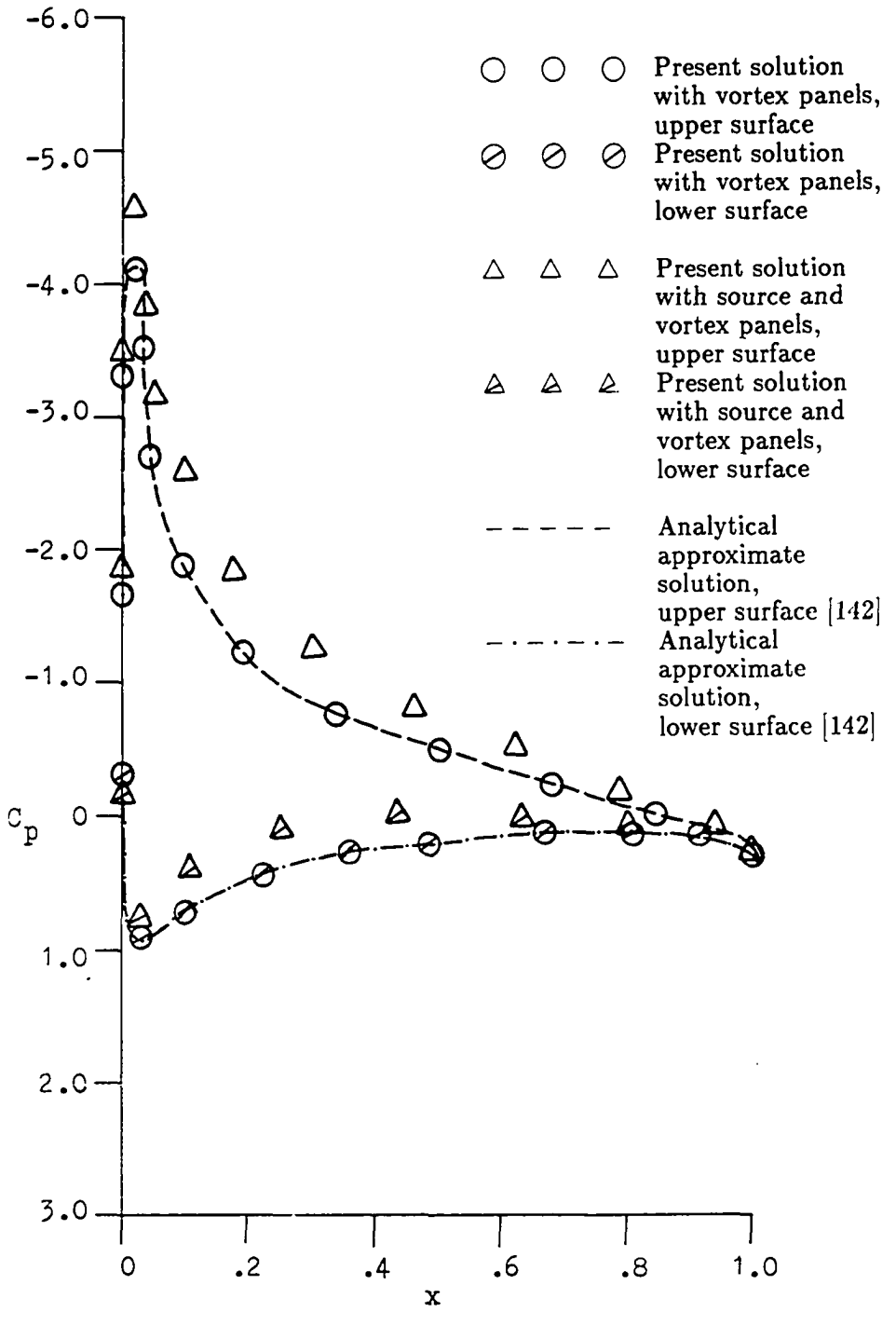

Fig. 6.2 Vortex vs. source-vortex panels, NACA 0012, $M_\infty = 0, \alpha = 9^\circ$.

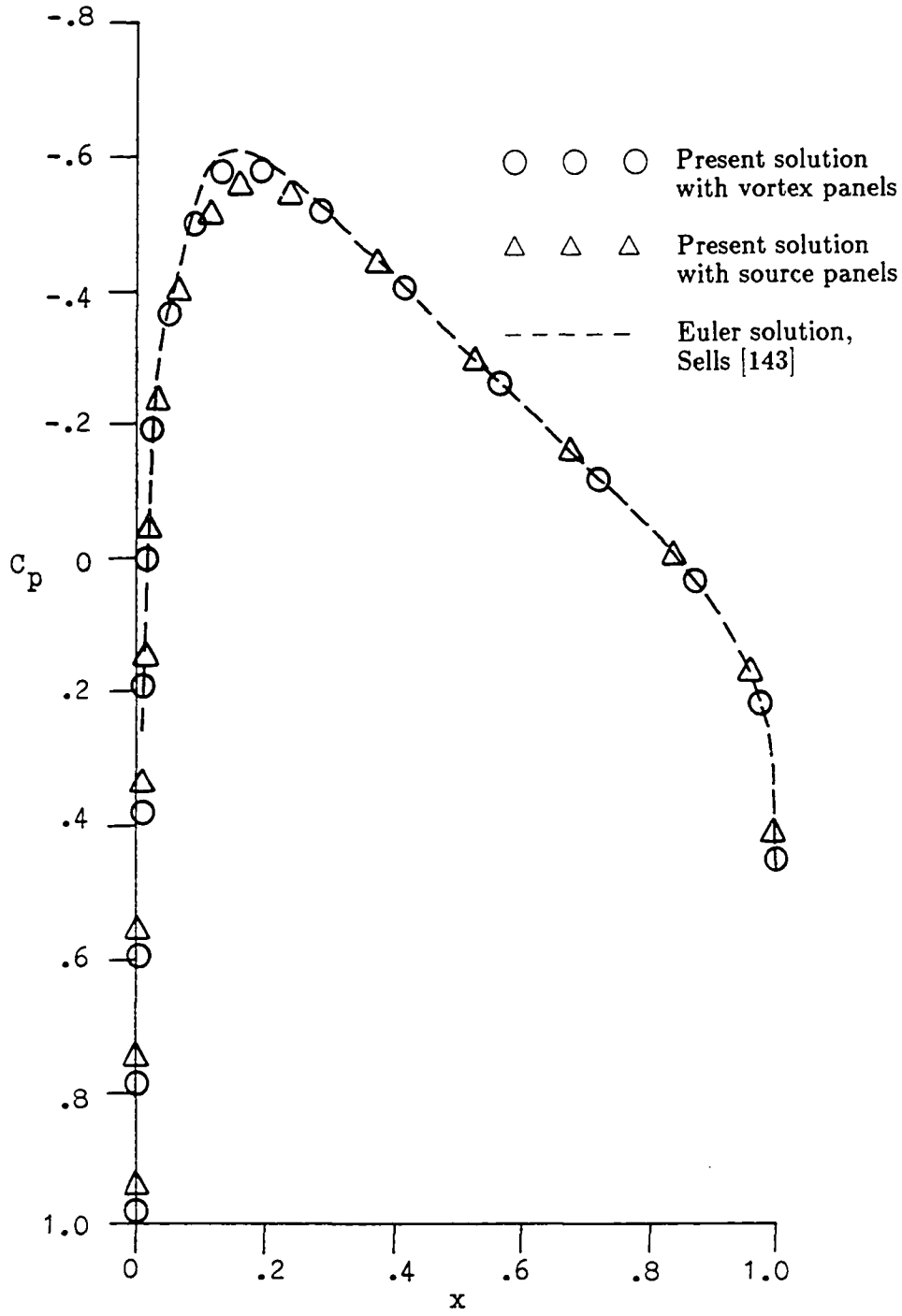

Fig. 6.3 Vortex vs. source panels, NACA 0012, $M_\infty = 0.72, \alpha = 0°$.

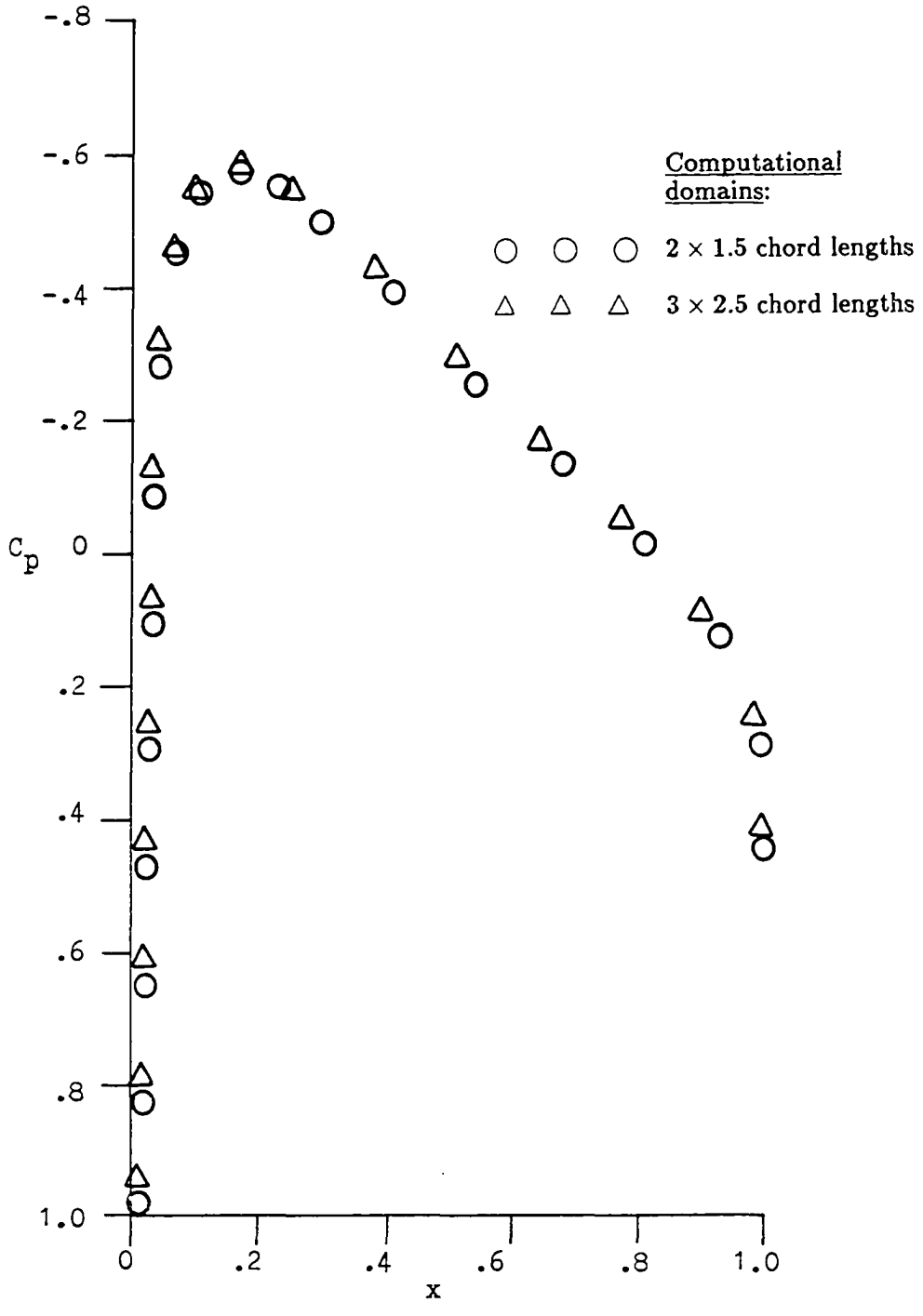

Fig. 6.4 Computational domain effect, NACA 0012, $M_\infty = 0.72, \alpha = 0°$.

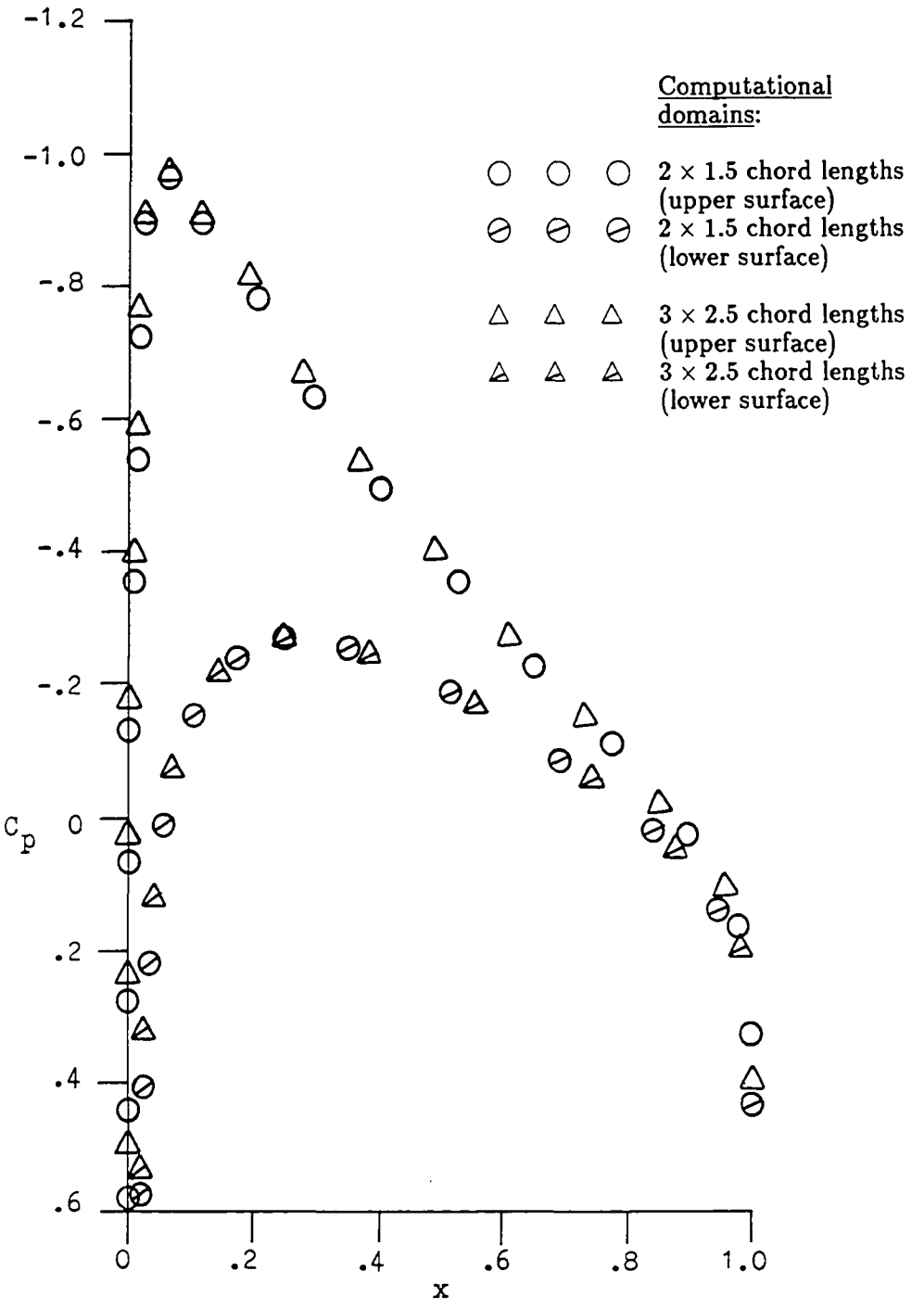

Fig. 6.5 Computational domain effect, NACA 0012, $M_\infty = 0.63, \alpha = 2^o$.

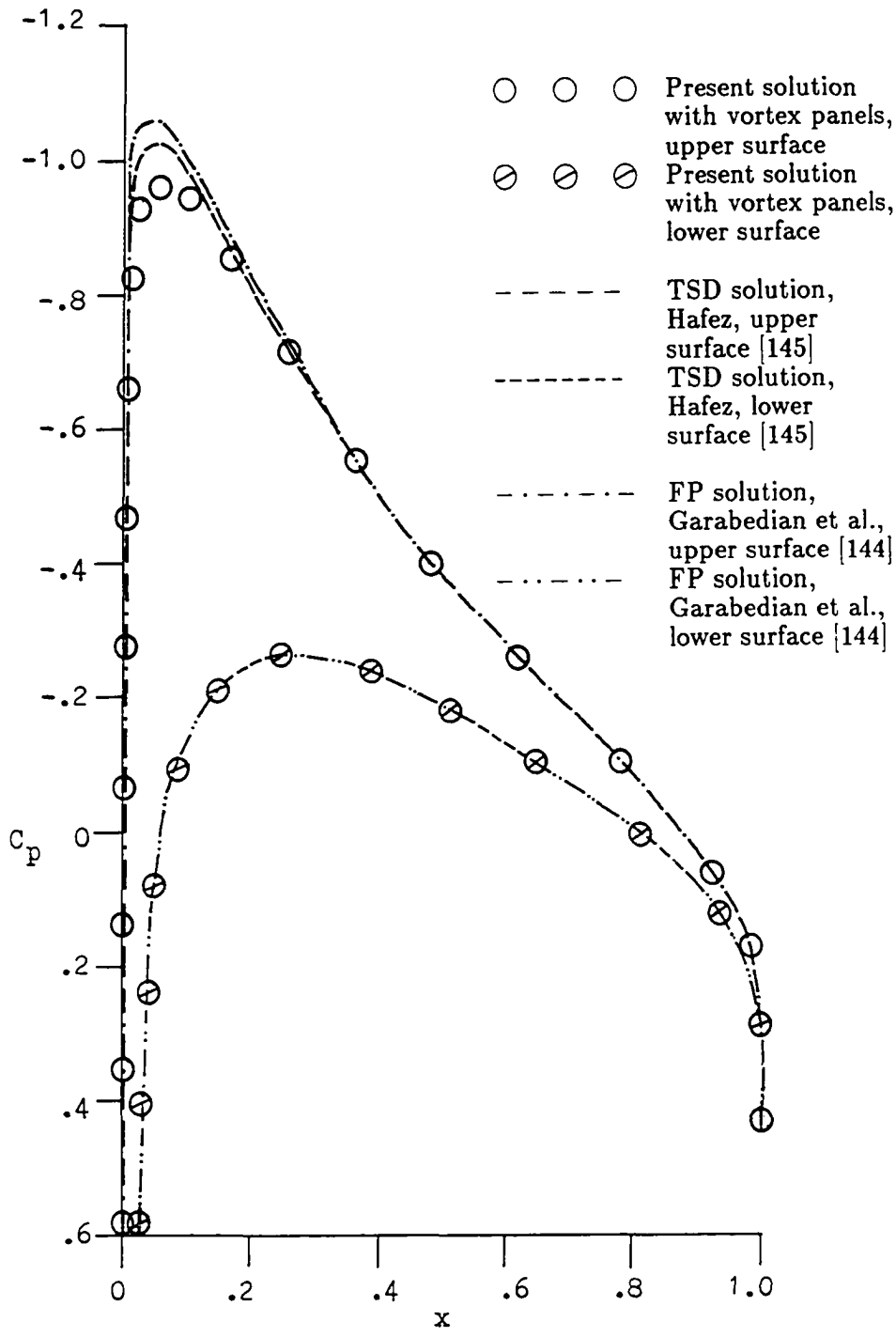

Fig. 6.6 Comparisons with FD solutions, NACA 0012, $M_\infty = 0.63, \alpha = 2^o$.

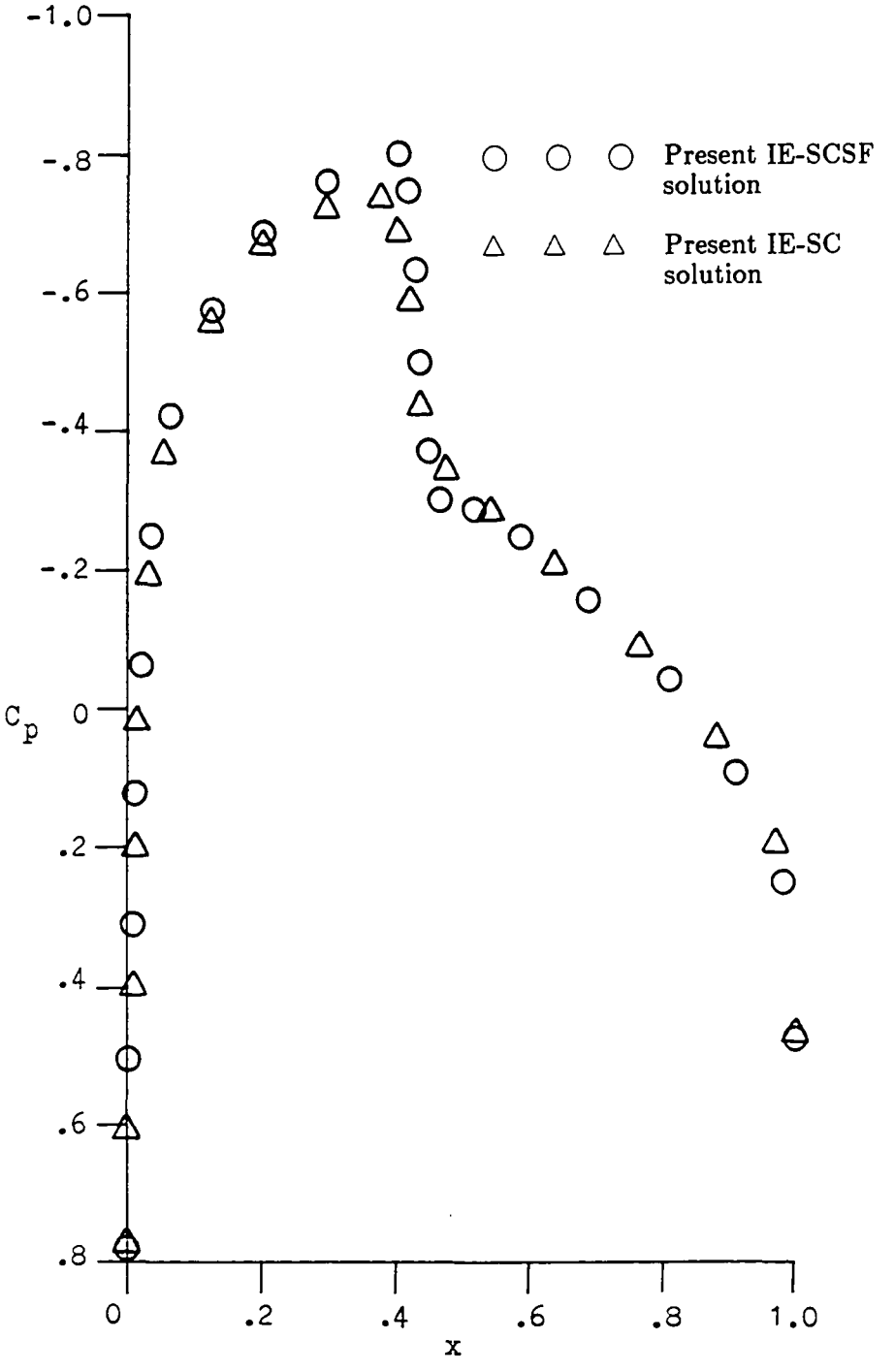

Fig. 6.7 IE-SC vs. IE-SCSF schemes, NACA 0012, $M_\infty = 0.8, \alpha = 0^\circ$.

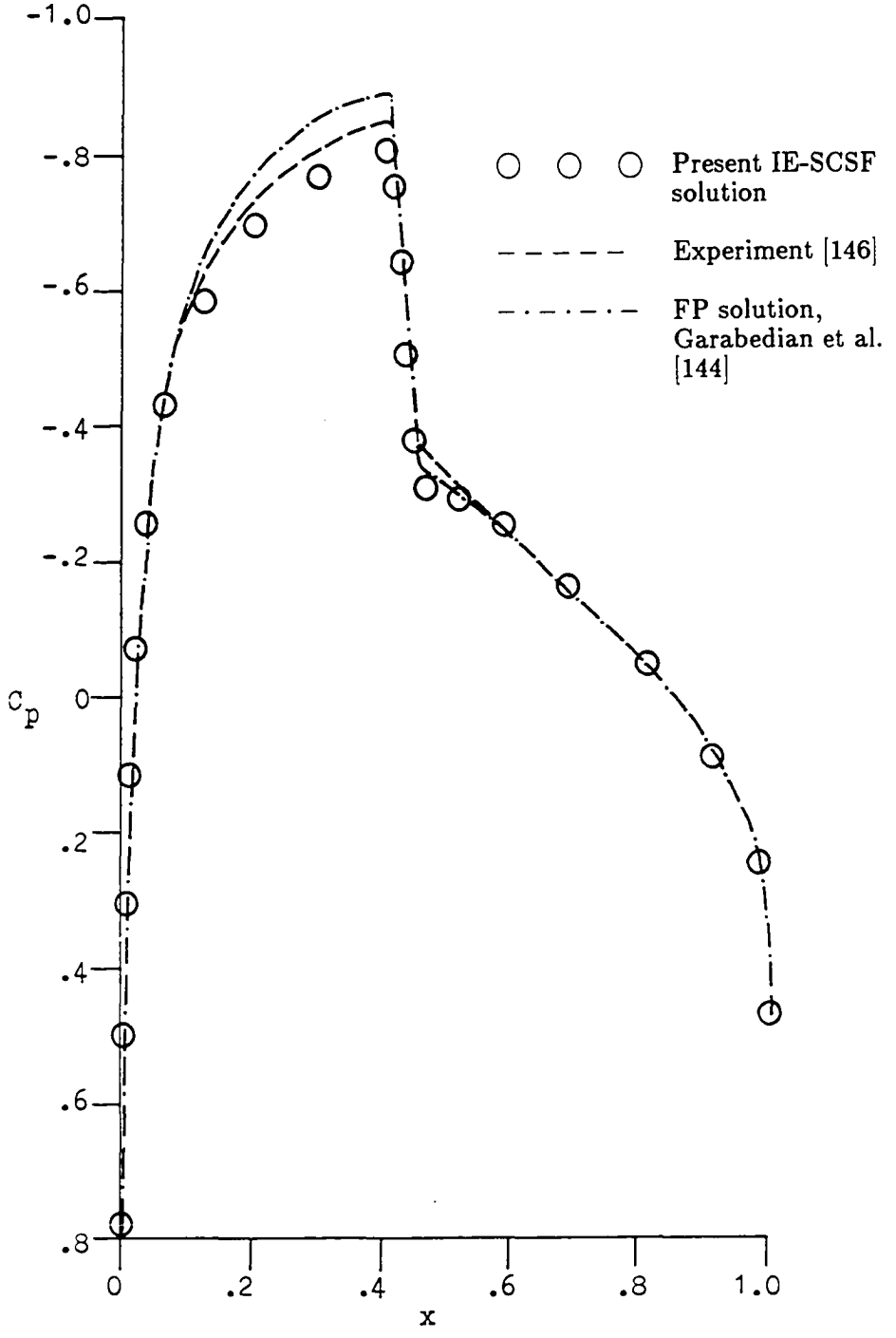

Fig. 6.8 Comparison of the IE-SCSF solution, NACA 0012, $M_\infty = 0.8, \alpha = 0^o$.

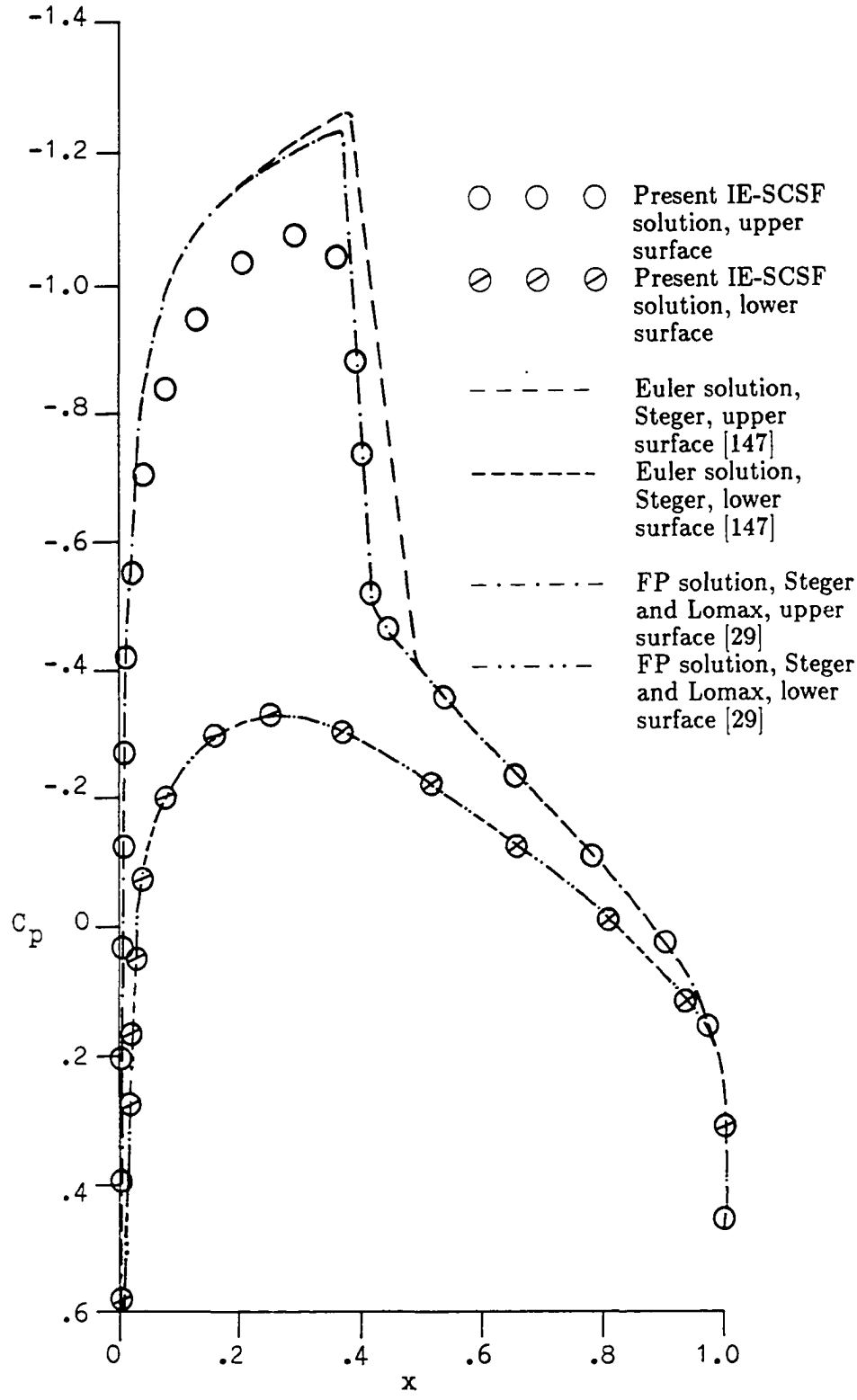

Fig. 6.9 Comparison of the IE-SCSF solution, NACA 0012, $M_\infty = 0.75, \alpha = 2^o$.

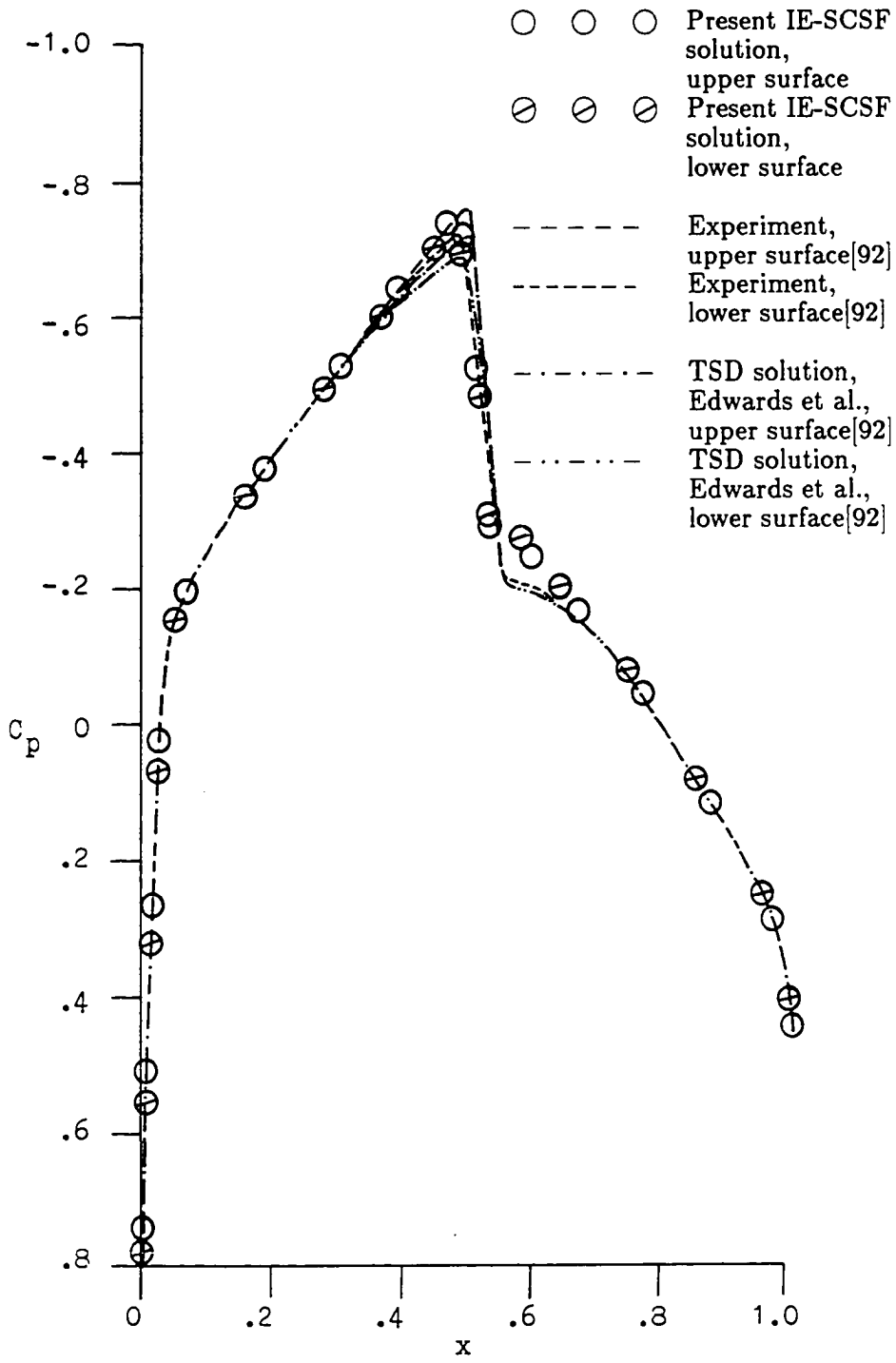

Fig. 6.10 Comparison of the IE-SCSF solution, NACA 64A010A, $M_\infty = 0.796$, $\alpha = 0^o$.

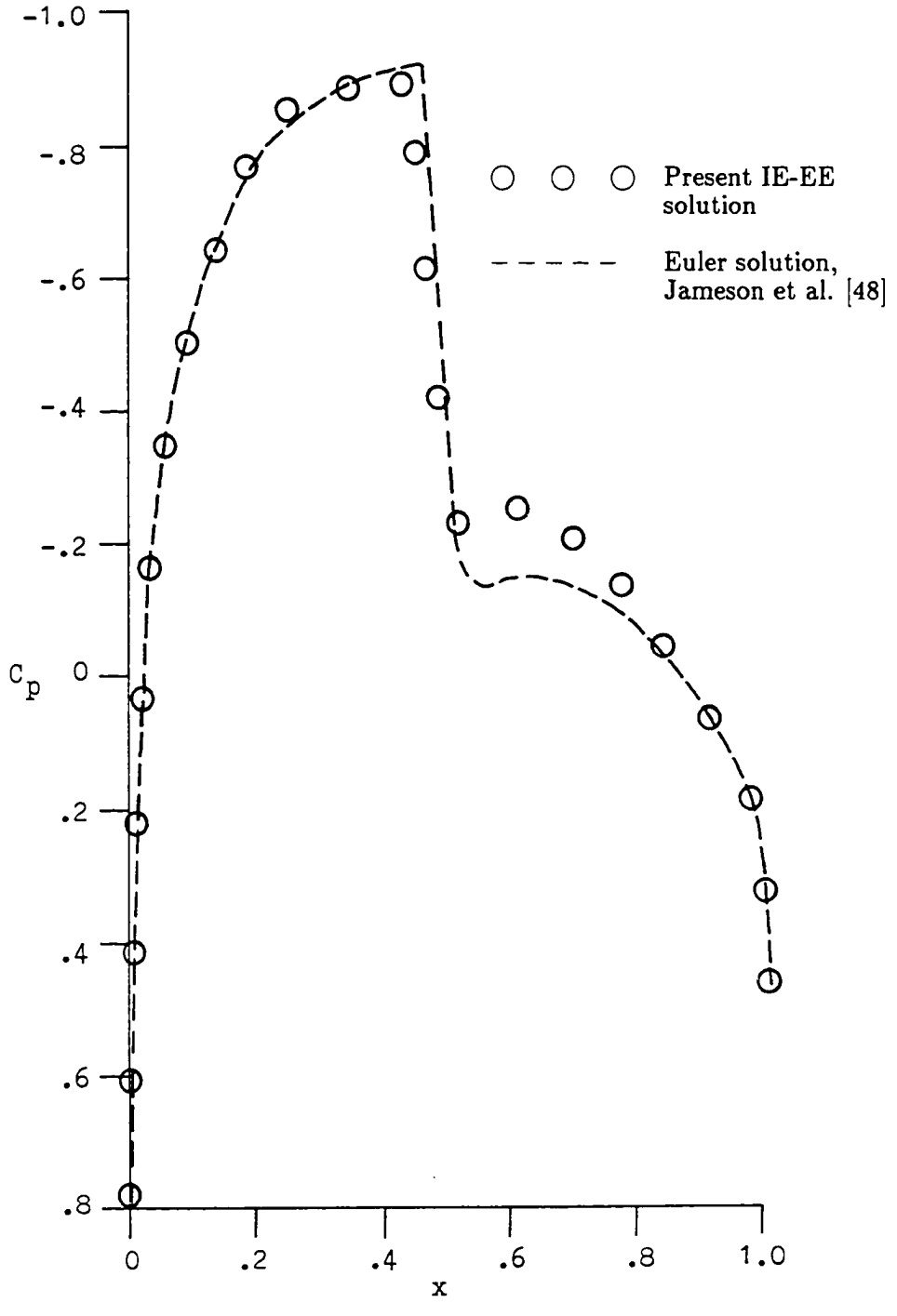

Fig. 6.11 Comparison of the IE-EE solution, NACA 0012, $M_\infty = 0.8, \alpha = 0°$.

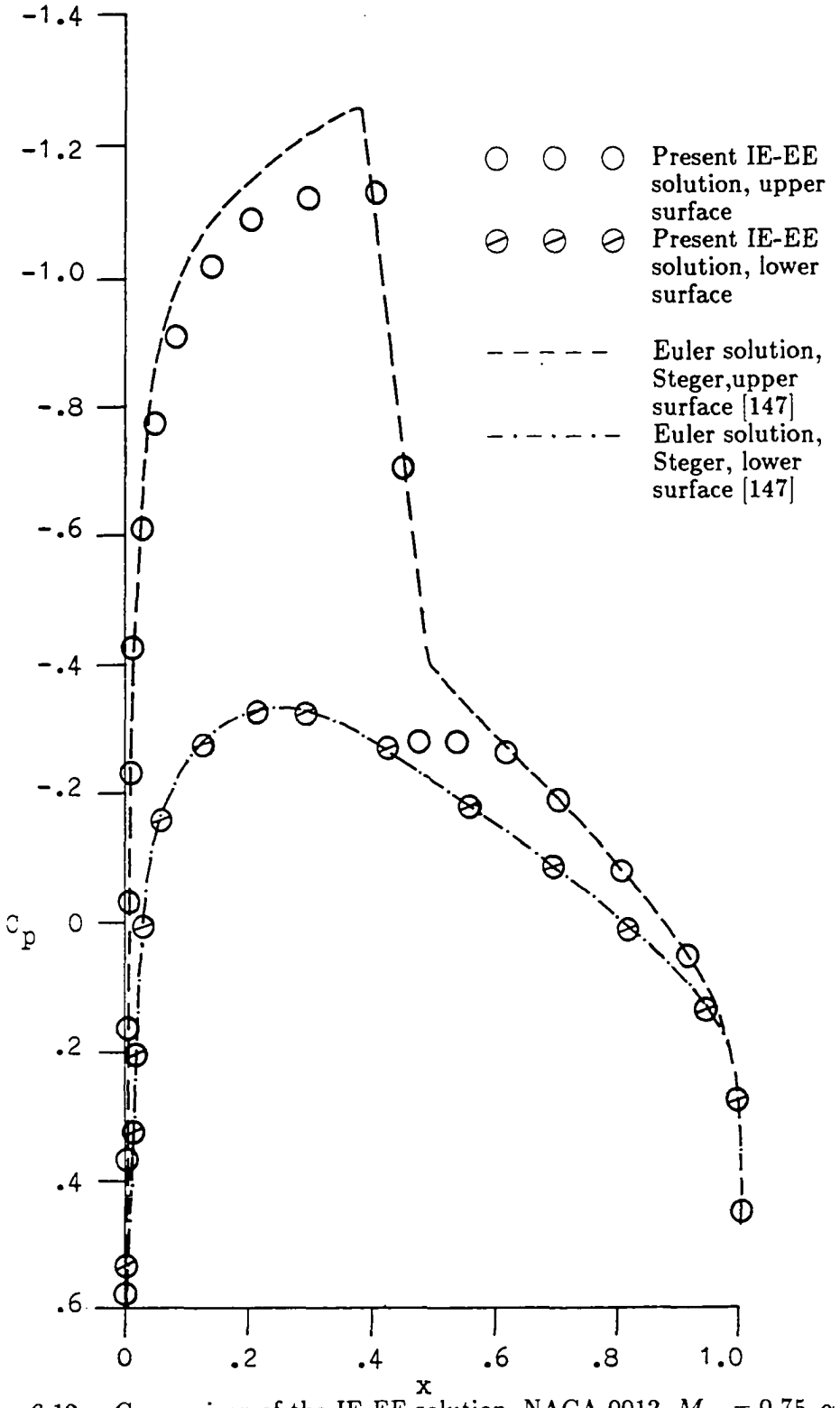

Fig. 6.12 Comparison of the IE-EE solution, NACA 0012, $M_\infty = 0.75, \alpha = 2^\circ$.

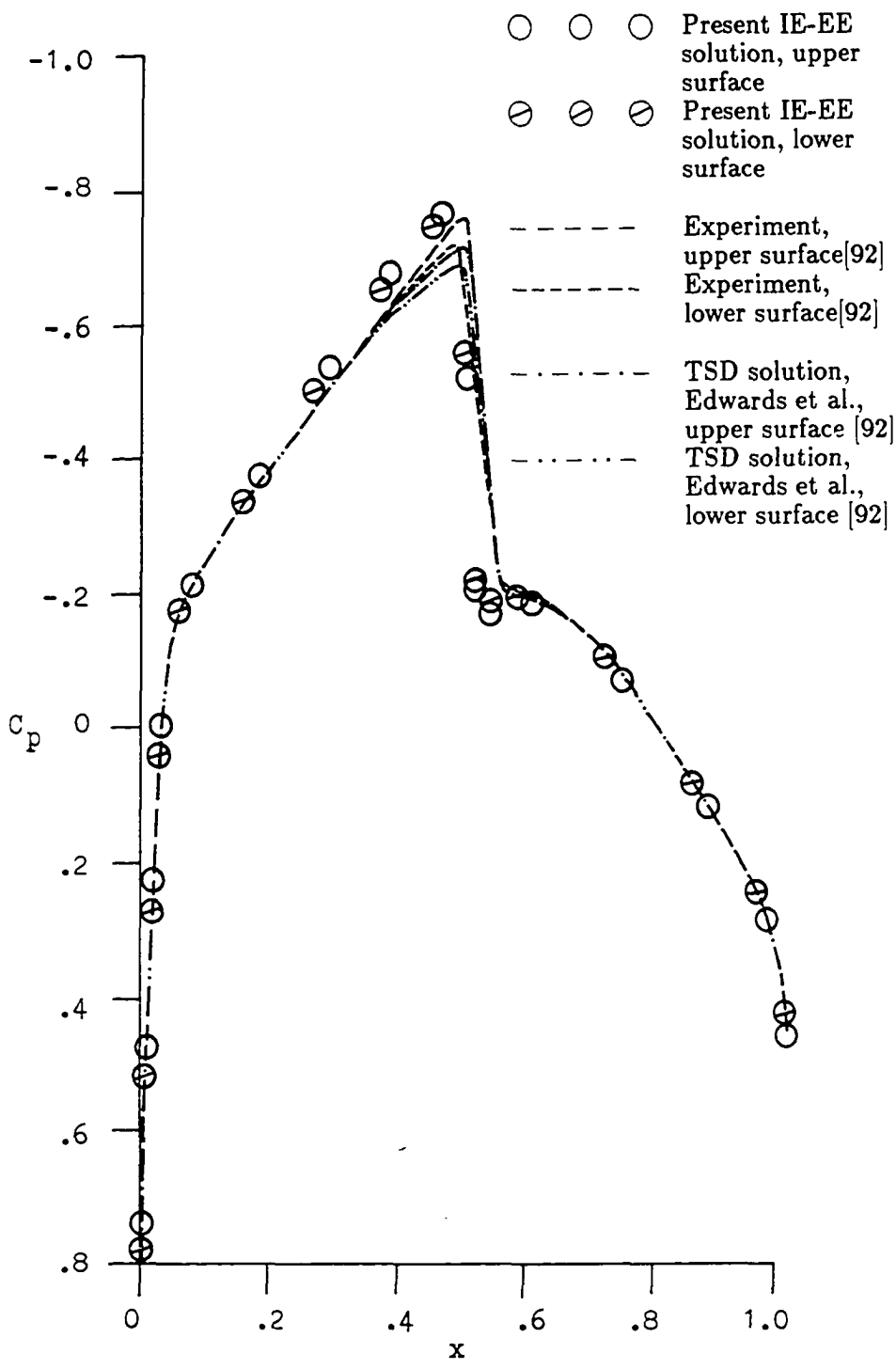

Fig. 6.13 Comparison of the IE-EE solution, NACA 64A010A, $M_\infty = 0.796$, $\alpha = 0^o$.

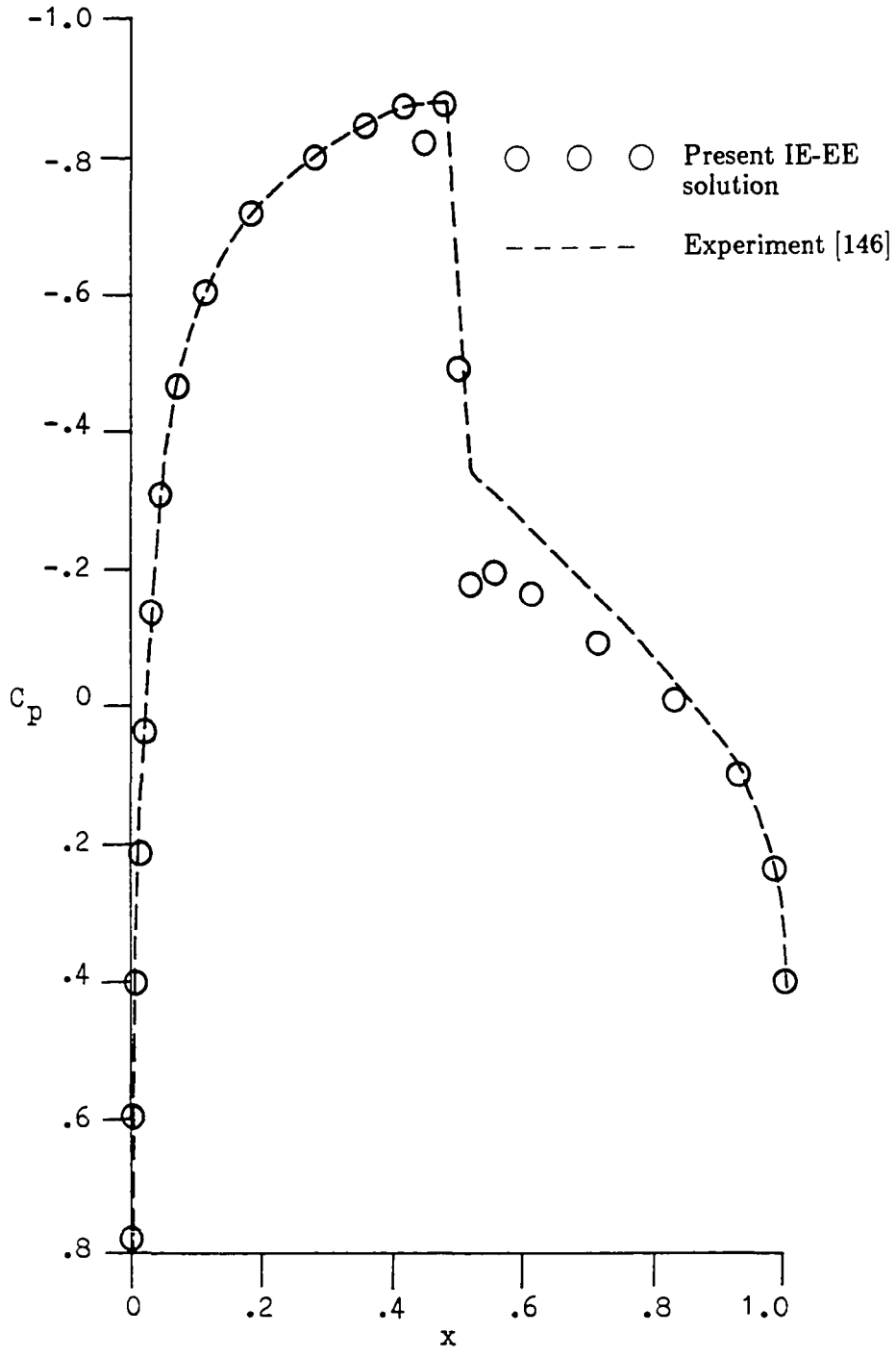

Fig. 6.14 Comparison of the IE-EE solution, NACA 0012, $M_\infty = 0.812, \alpha = 0°$.

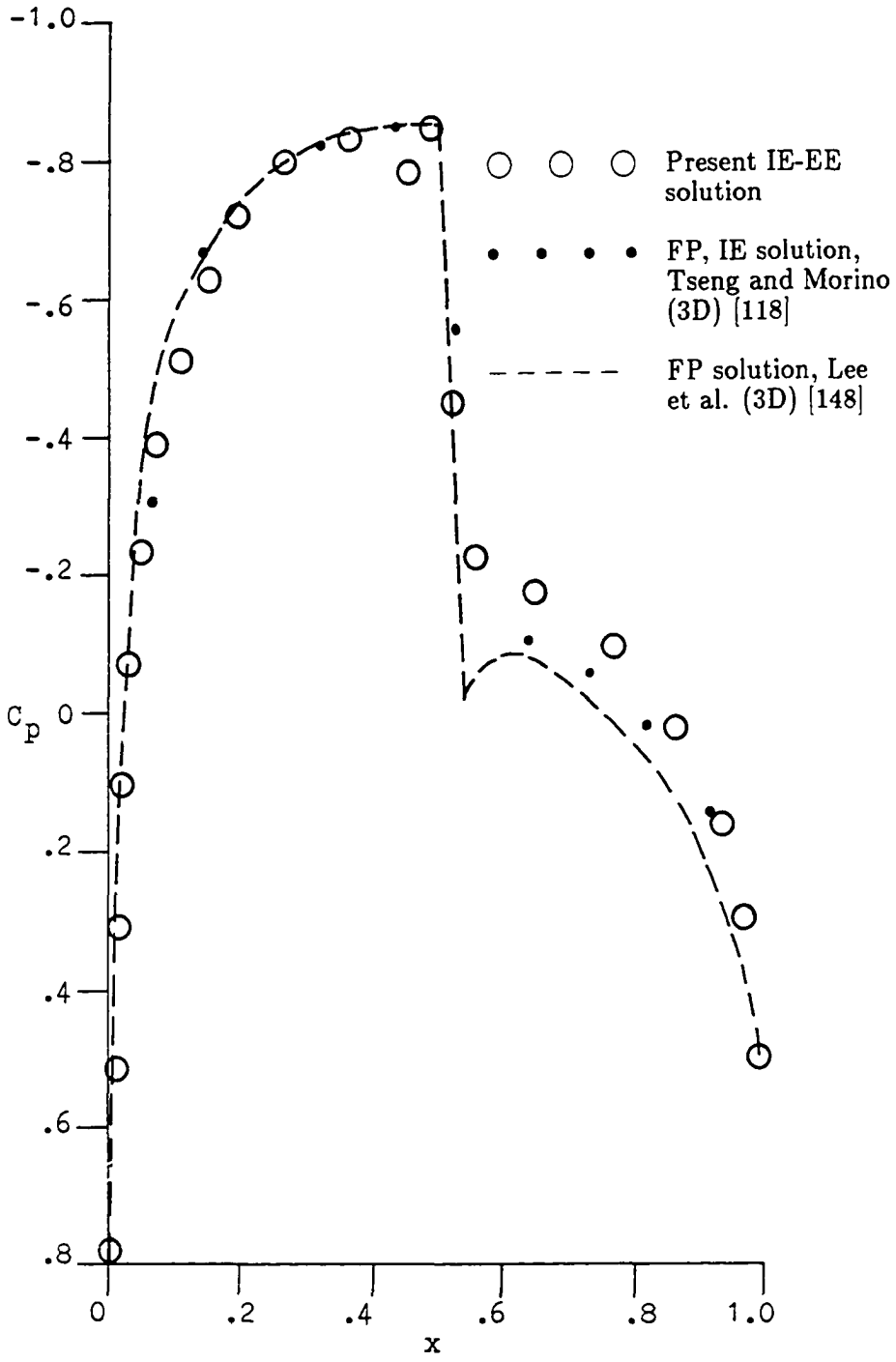

Fig. 6.15 Comparison of the IE-EE solution, NACA 0012, $M_\infty = 0.82, \alpha = 0^\circ$.

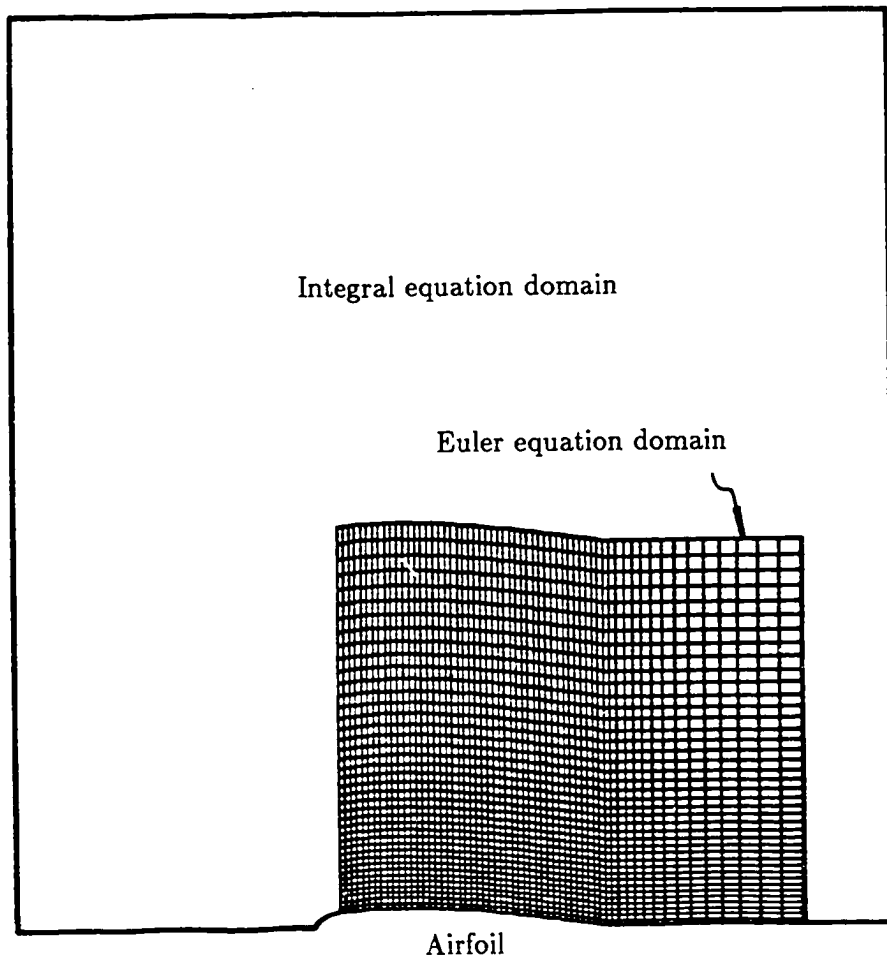

Fig. 6.16 IE and Euler domains, NACA 0012, $M_\infty = 0.84, \alpha = 0°$.

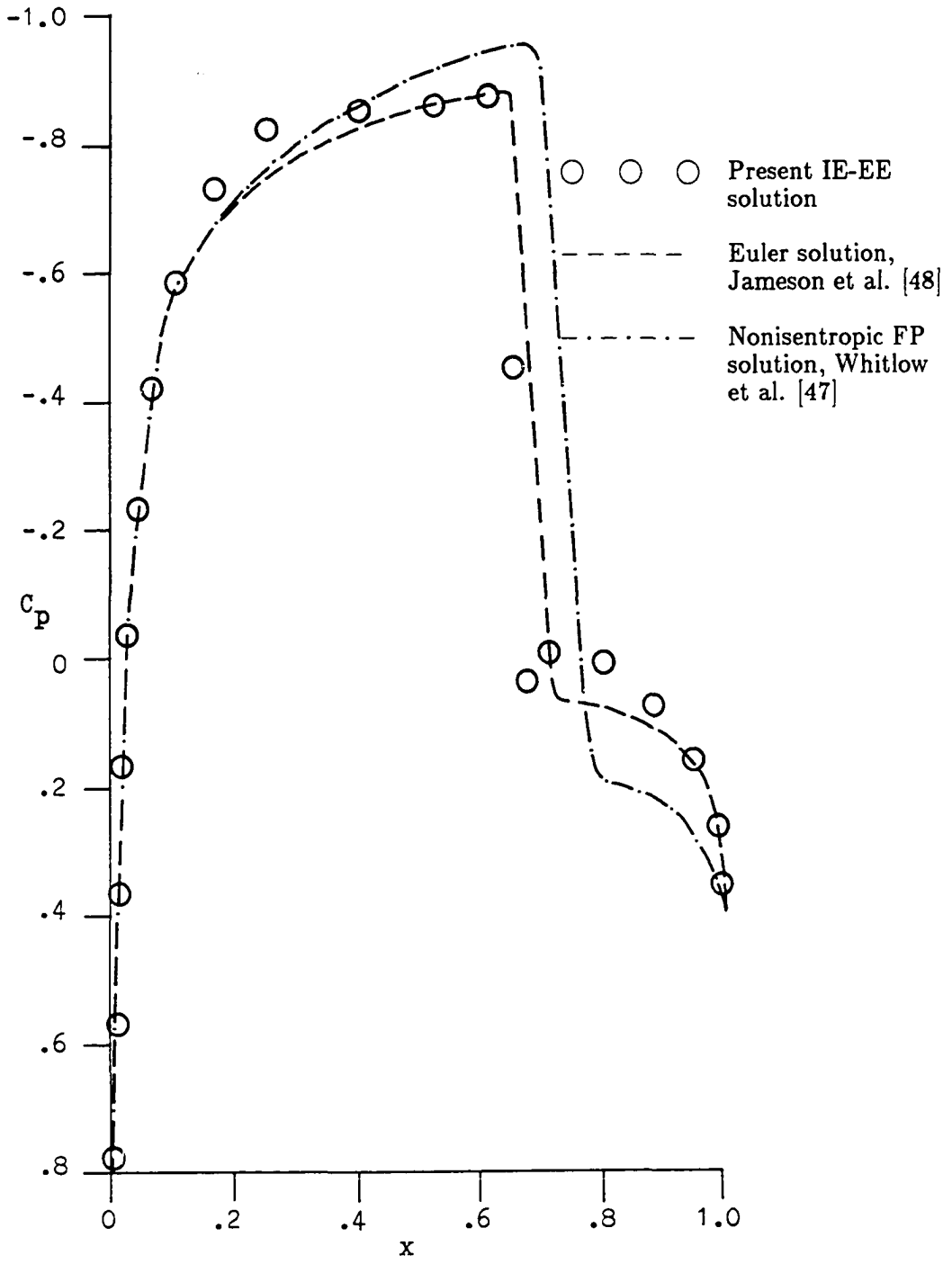

Fig. 6.17 Comparison of the IE-EE solution, NACA 0012, $M_\infty = 0.84, \alpha = 0^o$.

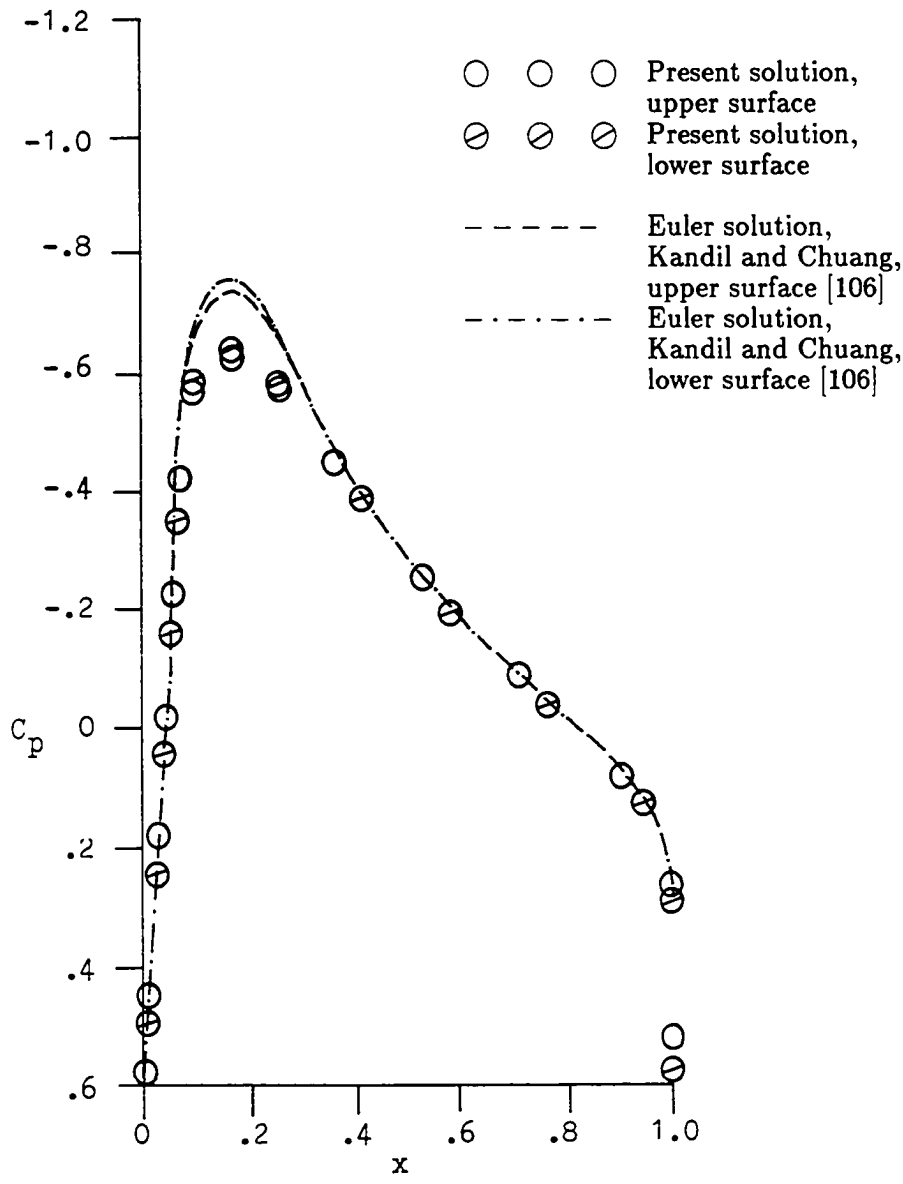

Fig. 6.18 Initial C_p distributions, NACA 0012, $M_\infty = 0.755, \alpha = \alpha_o = 0.016^o$.

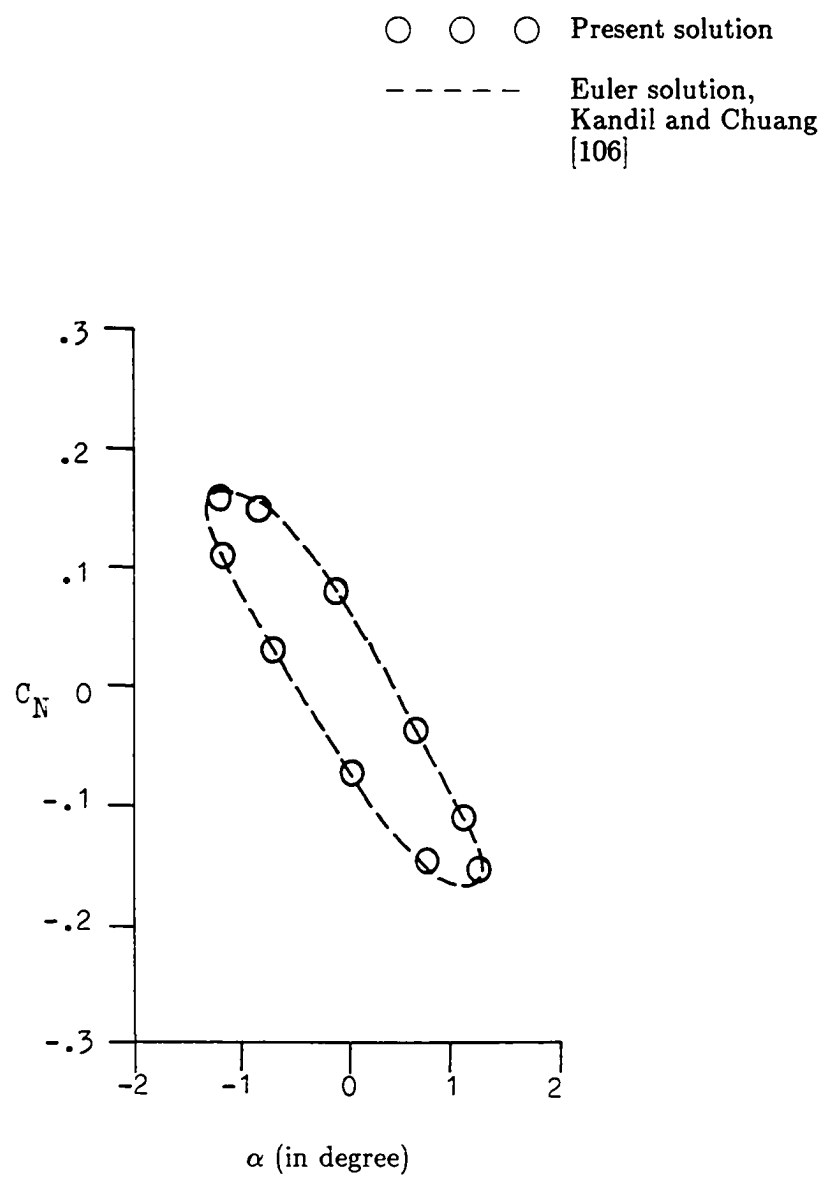

Fig. 6.19 Lifting coefficients for a pitching oscillation, NACA 0012, $M_\infty = 0.755$, $\alpha(t) = 0.016^\circ + 1.255^\circ \sin(0.1632t)$.

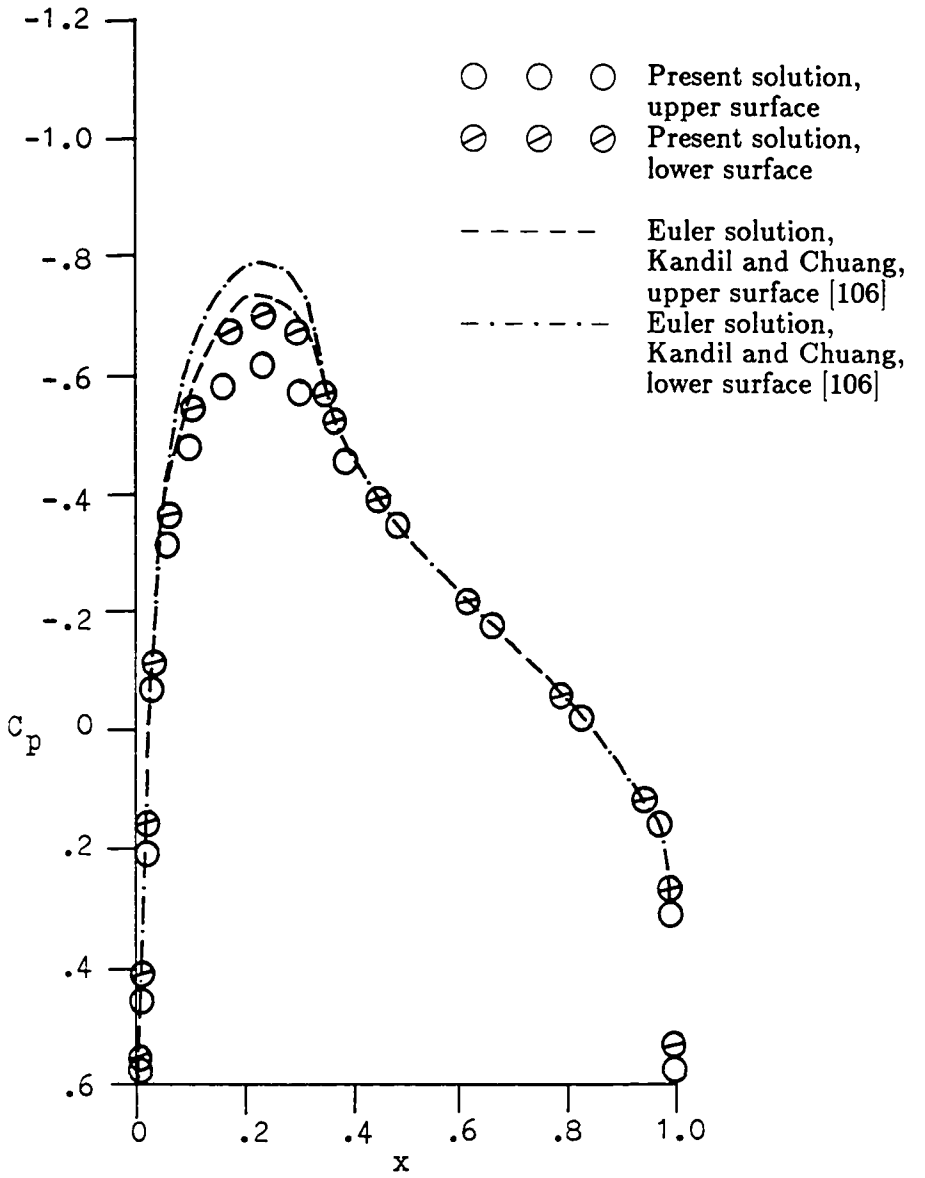

(a) $\alpha(t) = 0.729°, \quad k_c t = 35°$

Fig. 6.20 Time history of C_p for a pitching oscillation, NACA 0012, $M_\infty = 0.755$, $\alpha(t) = 0.016° + 1.255° \sin(0.1632t)$.

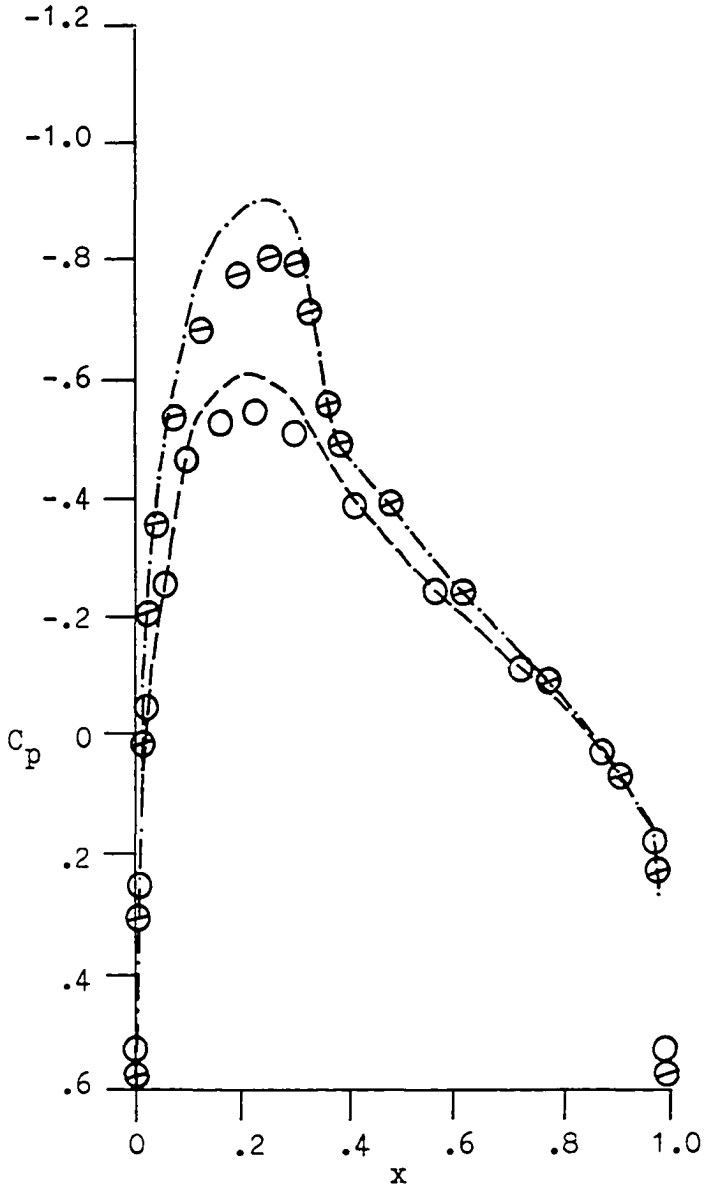

(*b*) $\alpha(t) = 1.189^o, \quad k_c t = 70^o$

Fig. 6.20 (Continued.)

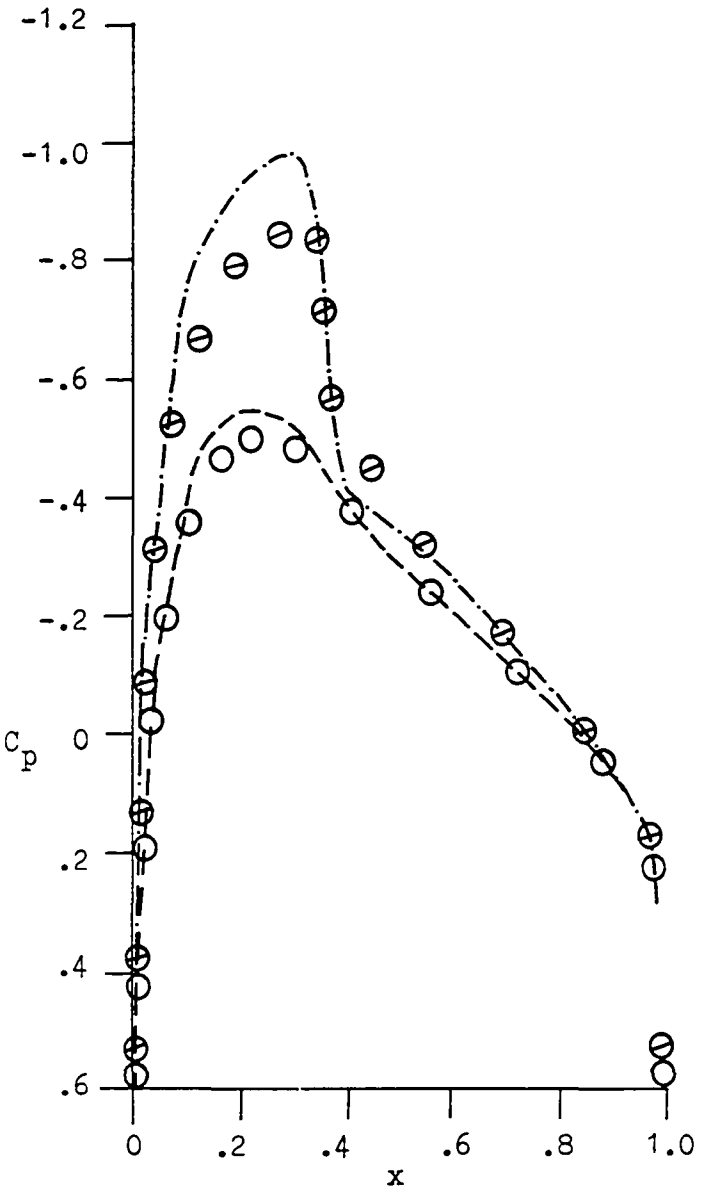

(c) $\alpha(t) = 1.235^o$, $k_c t = 104^o$

Fig. 6.20 (Continued.)

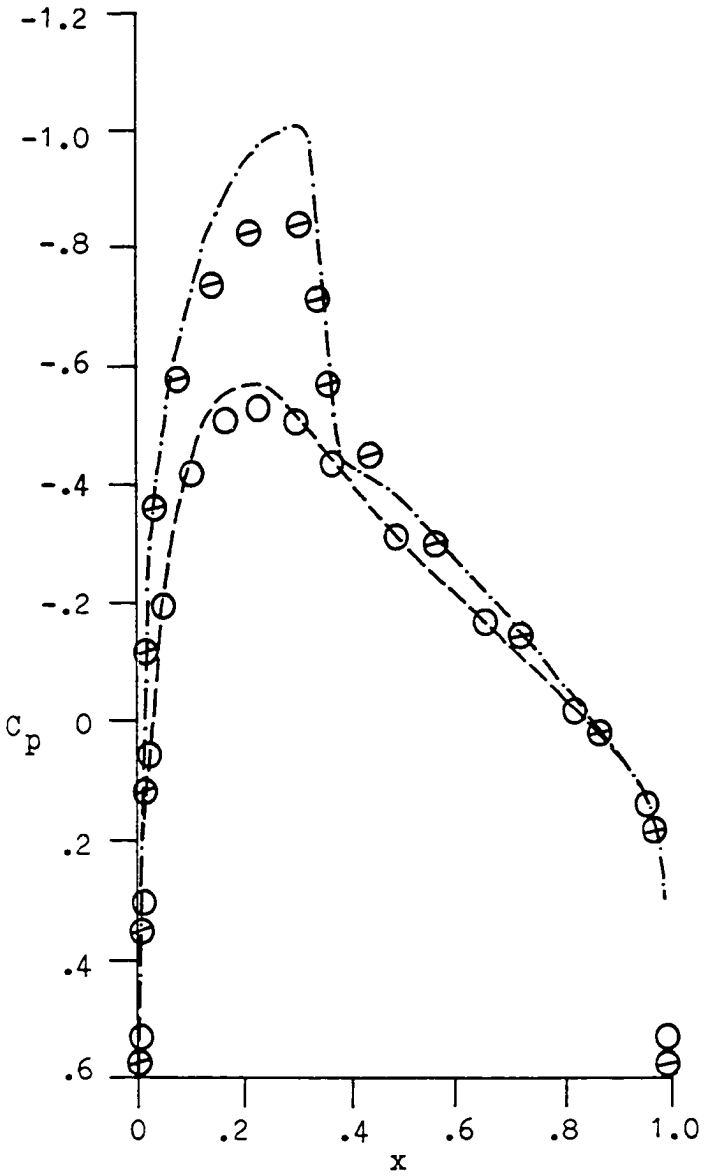

(*d*) $\alpha(t) = 0.848^o, \quad k_c t = 139^o$

Fig. 6.20 (Continued.)

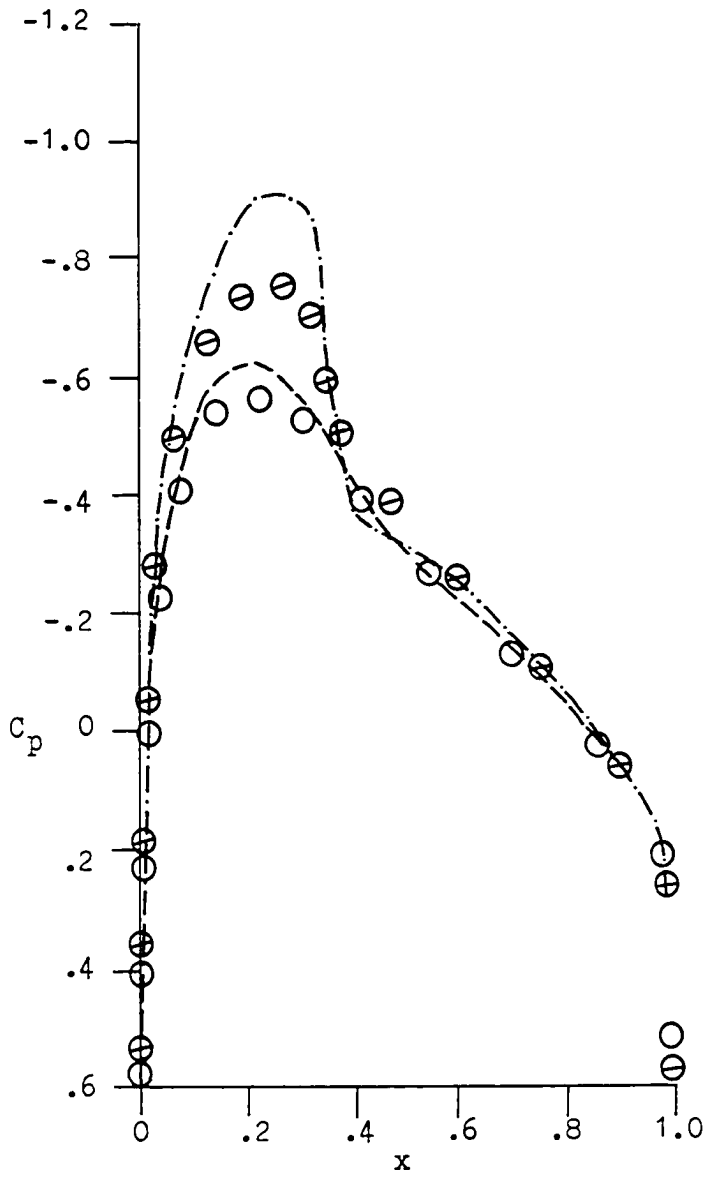

(e) $\alpha(t) = 0.167^o, \quad k_c t = 173^o$

Fig. 6.20 (Continued.)

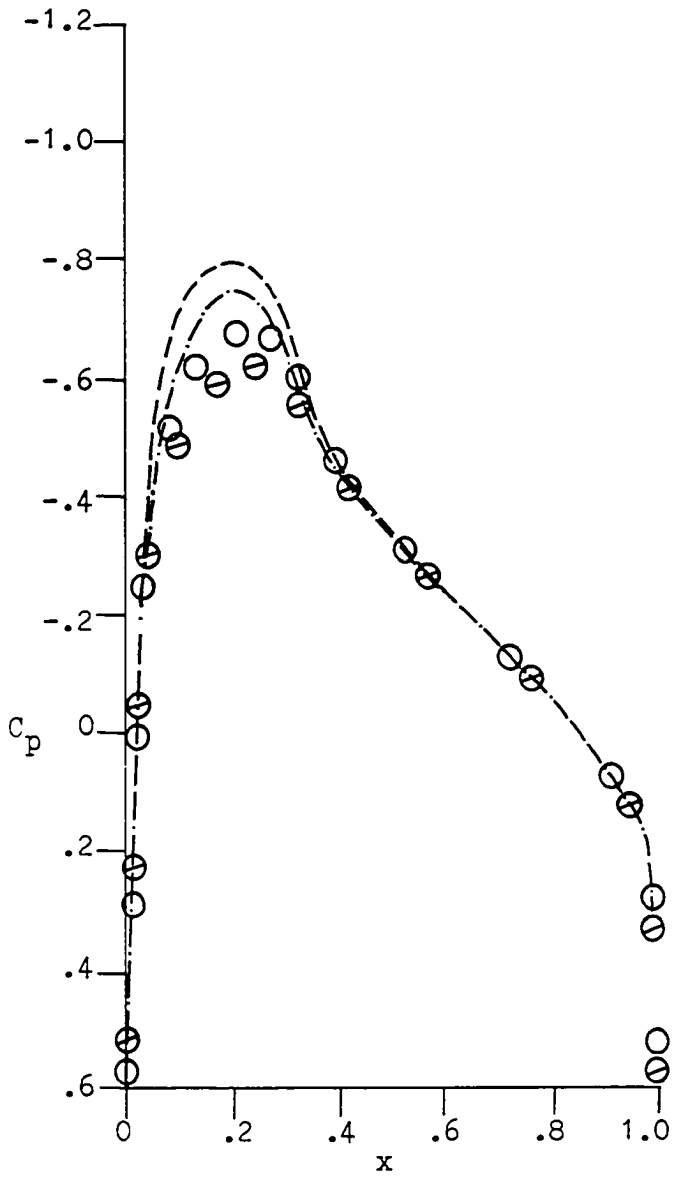

(f) $\alpha(t) = -0.697^o, \quad k_c t = 215^o$

Fig. 6.20 (Continued.)

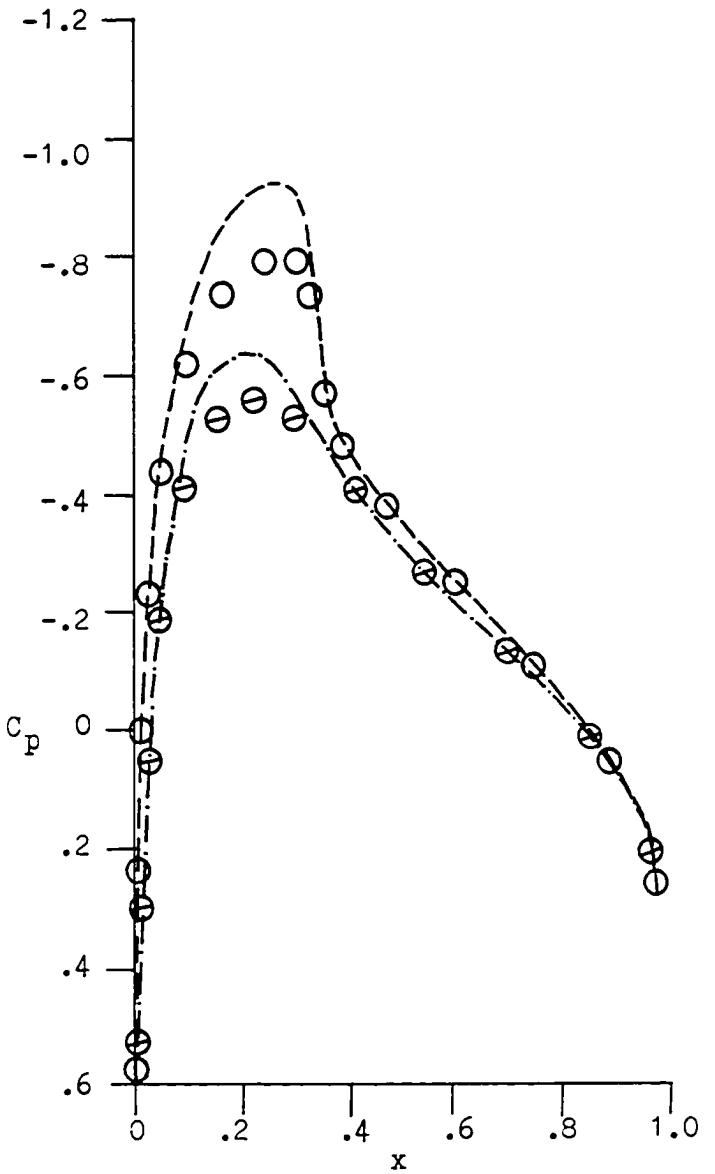

(g) $\alpha(t) = -1.157^o, \quad k_c t = 250^o$

Fig. 6.20 (Continued.)

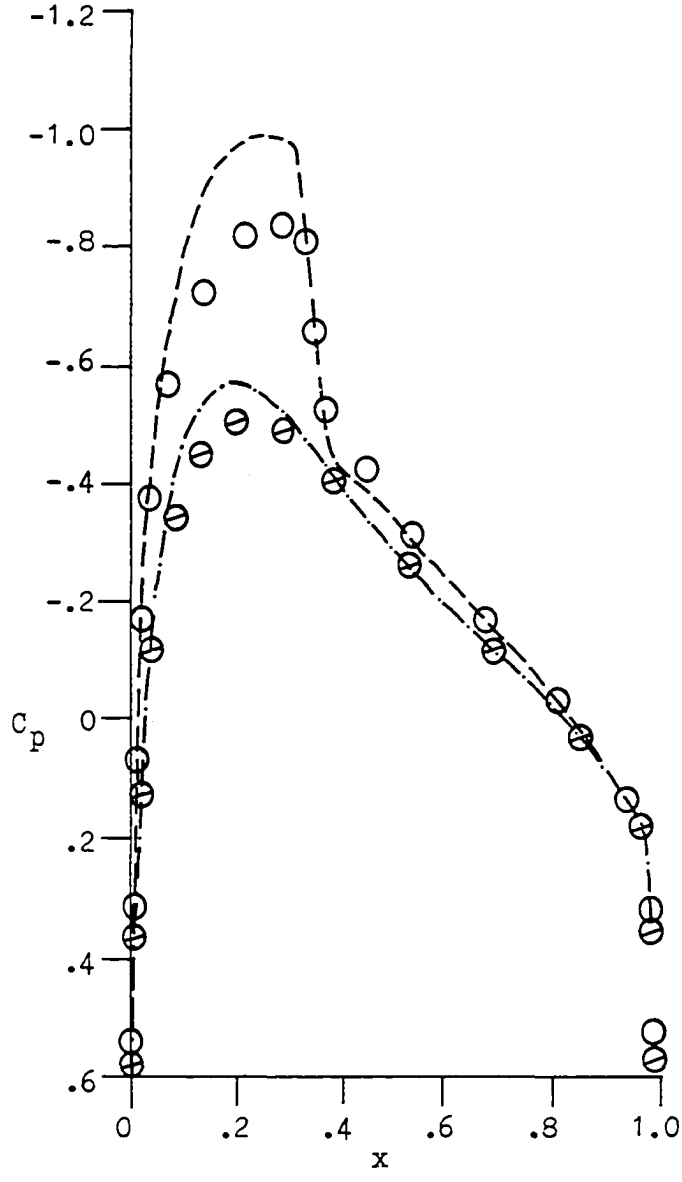

(h) $\alpha(t) = -1.203°, \quad k_c t = 284°$

Fig. 6.20 (Continued.)

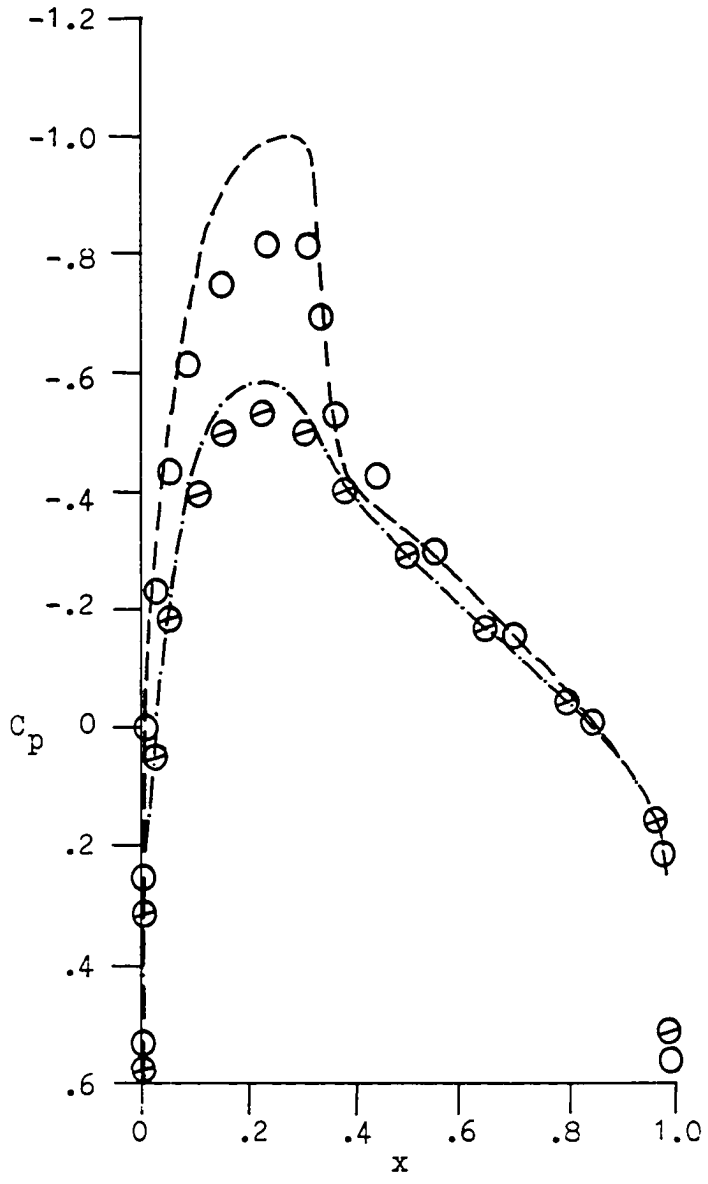

$(i) \quad \alpha(t) = -0.816^o, \quad k_c t = 319^o$

Fig. 6.20 (Continued.)

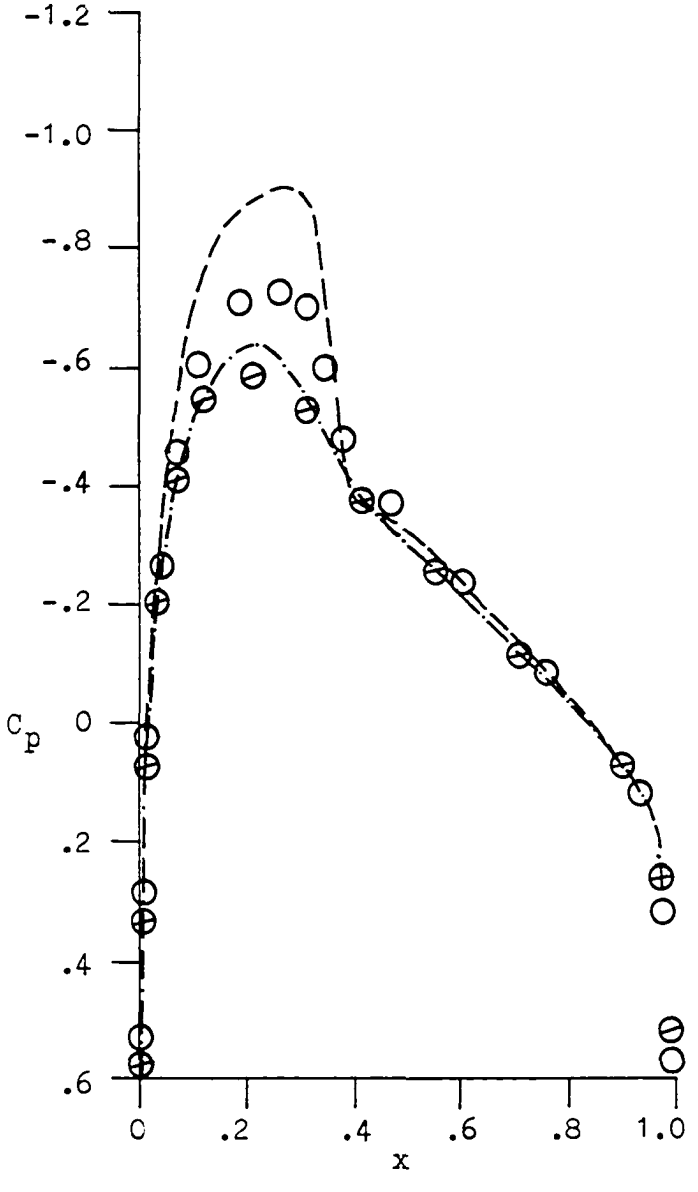

(j) $\alpha(t) = -0.135^{o}, \quad k_c t = 354^{o}$

Fig. 6.20 (Continued.)